Eur. Phys. J. C (2025) 85:791
https://doi.org/10.1140/epjc/s10052-025-14226-6

THE EUROPEAN PHYSICAL JOURNAL C

Regular Article - Experimental Physics

Energy scale and resolution for anti-k_t jets with radius parameters $R = 0.2$ and 0.6 measured in proton-proton collisions at $\sqrt{s} = 13$ TeV with the ATLAS detector

ATLAS Collaboration[⋆]

CERN, 1211 Geneva 23, Switzerland

Received: 23 December 2024 / Accepted: 23 April 2025

Abstract Jets with different radius parameters R are an important tool for probing quantum chromodynamics processes at different angular scales. Jets with small $R = 0.2$ are instrumental in measurements of the substructure of large-R jets resulting from collimated hadronic decays of energetic W, Z, and Higgs bosons, top quarks, and of potential new resonances. This paper presents measurements of the energy scale, resolution, and associated uncertainties of jets with radius parameters $R = 0.2$ and 0.6, obtained using the ATLAS detector. The results are based on 37 fb^{-1} of proton–proton collision data from the Large Hadron Collider at a centre-of-mass energy of $\sqrt{s} = 13$ TeV. A new *in situ* method for measuring jet energy scale differences between data and Monte Carlo simulations is presented. The systematic uncertainties in the jet energy scale for central jets ($|\eta| < 1.2$) typically vary from 1% to about 5% as a function of $|\eta|$ at very low transverse momentum, p_{T}, of around 20 GeV for both $R = 0.2$ and 0.6 jets. The relative energy resolution ranges from (35 ± 6)% at $p_{\mathrm{T}} = 20$ GeV to (6 ± 0.5)% at $p_{\mathrm{T}} = 300$ GeV for central $R = 0.2$ jets, and is found to be slightly worse for $R = 0.6$ jets. Finally, the effect of close-by hadronic activity on the jet energy scale is investigated and is found to be well modelled by the ATLAS Monte Carlo simulations.

Contents

1 Introduction

High energy proton–proton (pp) collisions at the Large Hadron Collider (LHC) [1] predominantly produce final states with collimated showers of hadrons known as jets. These final states with jets are used in many precision measurements and searches for new phenomena at the LHC. Jets reconstructed using the anti-k_t algorithm [2,3] with different radius parameters R are an important experimental tool for probing quantum chromodynamics (QCD) processes at different angular scales. Moreover, jets with small $R = 0.2$ are instrumental in reconstructing and measuring the substructure within large-R jets resulting from highly collimated hadronic decays of energetic W, Z, H bosons, top quarks, as well as potential new resonances.

This paper describes the methods used to calibrate the energy scale and energy resolution of jets reconstructed with the anti-k_t algorithm with radius parameters $R = 0.2$ and 0.6. The determination of the jet energy scale (JES) involves an *in situ* technique, referred to as the "direct matching method"

⋆ e-mail: atlas.publications@cern.ch

Published online: 22 July 2025

in the following, to correct for the observed jet response difference between data and Monte Carlo (MC) simulations. The direct matching method relates the energies of $R = 0.2$ and 0.6 jets to fully calibrated $R = 0.4$ jets reconstructed with the anti-k_t algorithm. The advantage of this new technique is the use of well-calibrated $R = 0.4$ jets as reference objects in only two topologies, Z+jet and dijet, without requiring the full complexity of the standard *in situ* calibration procedure using Z+jet, γ+jet, dijet, and multijet events described in Ref. [4], for each R parameter. This is the first application of this technique to jets in pp collisions at the LHC. A similar method was used to calibrate jets built using algorithms dedicated to heavy ion collisions [5]. The jet energy resolution (JER) is calibrated using the same methods as described in Ref. [4] since there are no obvious gains in changing that straightforward methodology.

Energy calibration and resolution measurements of jets with $R = 0.2$ and 0.6 are presented using 37 fb^{-1} of pp collision data collected in 2015 and 2016 at $\sqrt{s} = 13$ TeV [6,7]. To study the sensitivity to additional pp interactions in the event (pile-up), some of the systematic uncertainties related to the JES were also studied using 44 fb^{-1} of data taken in 2017 under higher pile-up conditions. No significant pile-up dependence was identified. These results are applicable for the entire Run 2 of the LHC between 2015 and 2018. The JES and JER results presented here are used in published [8,9] ATLAS results.

A correct modelling in MC simulations of the detector response in dense environments with overlapping energy signatures from independent particles is crucial for analyses relying on collimated decays of energetic massive particles into hadrons. This is tested by studying the effect on the JES for close-by jets whose central axes are separated by an angular distance[1] ΔR that is small relative to their size parameters, in data and in MC simulations.

The ATLAS Collaboration has published JES and JER calibration results for $R = 0.4$ jets previously, with data taken in 2010 [10–12], 2011 [13], 2012 [14], and 2015 [15], 2015–2017 [4], and 2015–2018 [16,17]. Papers using Run 1 data recorded in 2010–2012 include dedicated calibrations of jets reconstructed with the anti-k_t algorithm with $R = 0.6$ and $R = 1.0$. A dedicated *in situ* calibration of jets with $R = 1.0$ is carried out using Run 2 data taken in 2015 and 2016 [18]. The effect of close-by jets was previously studied using early Run 2 data recorded in 2016 [19]. A calibration of jets in 2015–2018 data was derived from single particle responses and found to be consistent with standard methods [17].

This publication presents the first jet energy calibration and resolution measurements of anti-k_t $R = 0.2$ jets, and the first measurements of anti-k_t 0.6 jets for $\sqrt{s} > 7$ TeV. The established calibrations of anti-k_t jets with the standard radius parameter of $R = 0.4$, derived using Run 2 data at $\sqrt{s} = 13$ TeV, are used as a reference. In the following, anti-k_t $R = 0.2$ and 0.6 jets are collectively referred to as "alternative radius" (AR) jets.

This paper is organised as follows. After a description of the ATLAS detector in Sect. 2, the data and the MC simulations used are described in Sect. 3 and the jet reconstruction algorithms in Sect. 4. Section 5 details the calibration of the jet energy scale, including the description of the direct matching technique. Section 6 describes the calibration of the jet energy resolution and the associated uncertainties. The effect of close-by jets on the JES is investigated in Sect. 7. Finally, the conclusions are given in Sect. 8.

2 The ATLAS detector

The ATLAS detector consists of an inner detector tracking system spanning the pseudorapidity range $|\eta| < 2.5$, sampling electromagnetic and hadronic calorimeters covering the range $|\eta| < 4.9$, and a muon spectrometer spanning $|\eta| < 2.7$. A detailed description of the ATLAS detector can be found in Ref. [20].

Charged-particle tracks are reconstructed in the inner detector (ID), which consists of three subdetectors: a silicon pixel tracker closest to the beamline, a microstrip silicon tracker, and a straw-tube transition radiation tracker farthest from the beamline. The ID is surrounded by a thin solenoid providing an axial magnetic field of 2 T, allowing the measurement of charged-particle momenta. Since Run 2, a new innermost layer of the silicon pixel tracker, the insertable B-layer (IBL) [21], was added at a radial distance of 3.3 cm from the beamline to enhance track reconstruction, pile-up mitigation, and the identification of jets initiated by b-quarks.

The ATLAS calorimeter system consists of inner electromagnetic calorimeters surrounded by hadronic calorimeters. The calorimeters are segmented in η and ϕ, and each region of the detector has at least three calorimeter readout layers for measuring longitudinal shower profiles. Within $|\eta| < 3.2$, electromagnetic calorimetry is provided by high-granularity lead/liquid-argon (LAr) calorimeters. Energy loss of particles traversing inactive detector material before reaching the calorimeters is corrected for using an additional thin LAr presampler within $|\eta| < 1.8$. Hadronic calorimetry is provided by the steel/scintillator-tile calorimeter, segmented into three barrel structures within $|\eta| < 1.7$, and

[1] ATLAS uses a right-handed coordinate system with its origin at the nominal interaction point (IP) in the centre of the detector and the z-axis along the beam pipe. The x-axis points to the centre of the LHC ring, and the y-axis points upward. Cylindrical coordinates (r, ϕ) are used in the transverse plane, ϕ being the azimuthal angle around the z-axis. The pseudorapidity is defined in terms of the polar angle θ as $\eta = -\ln\tan(\theta/2)$. The distance between two objects in η–ϕ space is $\Delta R = \sqrt{(\Delta\eta)^2 + (\Delta\phi)^2}$. Transverse momentum is defined by $p_{\mathrm{T}} = p\sin\theta$.

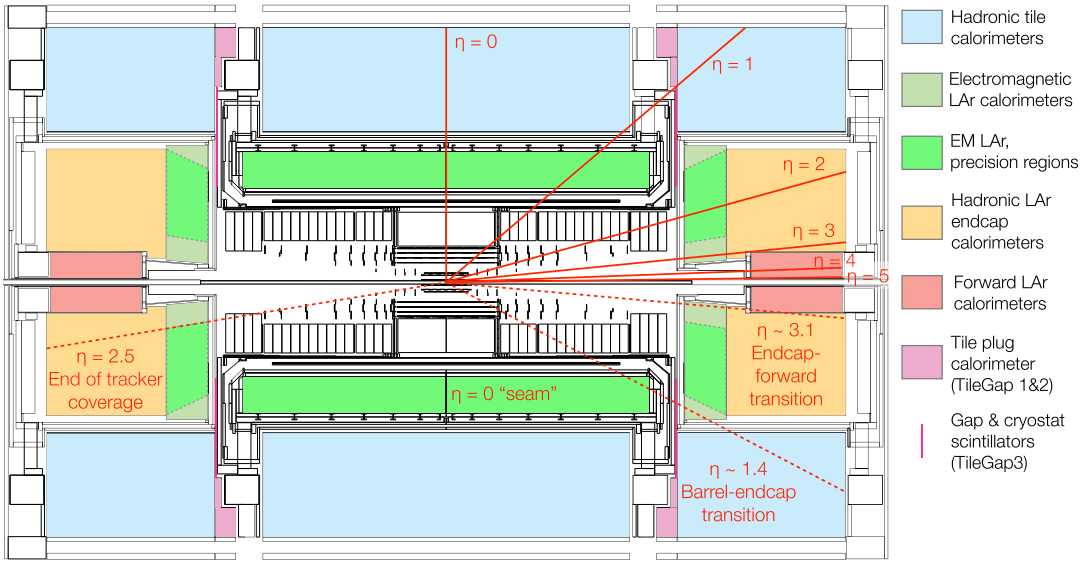

Fig. 1 A schematic diagram of the calorimeter system of the ATLAS detector adapted from Ref. [4], including the inner tracking and the solenoid magnet. Integer values of pseudorapidity η ranging from zero to five are indicated by solid lines. Relevant detector regions are highlighted and their pseudorapidity is shown as dashed lines

two copper/LAr hadronic endcap calorimeters cover the range $1.5 < |\eta| < 3.2$. The solid angle coverage between $3.2 < |\eta| < 4.9$ is completed with forward copper/LAr and tungsten/LAr calorimeter modules optimised for electromagnetic and hadronic measurements respectively. Gaps at the interfaces between each of these components, in particular between the barrel and endcap regions, allow the routing of various services and infrastructure, such as electrical and fiber-optic cabling, cooling, and support structures. However, these interfaces also create discontinuities in the response of the calorimeter to both charged and neutral particles due to energy absorption in the inactive materials and changes in the geometry of the active materials of the calorimeters. The calibrated response and resolution of the calorimeter must therefore either correct for these features, or account for them when establishing systematic uncertainties. The components of the calorimeter system [20,22,23] with reference pseudorapidities and various relevant transition regions also marked, are shown in Fig. 1.

A muon spectrometer with an air-core toroid magnet system surrounds the calorimeters. Three layers of high-precision tracking chambers provide coverage in the $|\eta| < 2.7$ range, while dedicated fast chambers allow triggering in the $|\eta| < 2.4$ region. The ATLAS trigger system consists of a hardware-based level-1 trigger followed by a software-based high-level trigger [24].

3 Data and Monte Carlo simulation

The pp collision data used for the calibrations presented here were recorded by the ATLAS experiment at the LHC during the 2015 and 2016 data-taking periods of Run 2 at a centre-of-mass energy of $\sqrt{s} = 13$ TeV and with bunch crossing intervals of 25 ns. After requirements on data quality [25] and on the operational status of all relevant detector sub-systems, this data sample corresponds to an integrated luminosity of 37 fb^{-1} . Predictions from several MC generators are used to simulate the physics processes relevant for the different jet calibrations as outlined in the following.

The PYTHIA8.186 [26] generator together with the NNPDF 2.3 LO [27] parton distribution function (PDF) set is used to simulate multijet events in pp collisions at $\sqrt{s} = 13$ TeV. It uses leading-order QCD matrix elements for $2 \to 2$ processes, along with a leading-logarithmic parton shower (PS), underlying event (UE) simulation with multiple parton interactions, and the Lund string model [28] for hadronisation. The UE, PS and hadronisation parameters are those from the A14 [29] set of tuned parameters (tune). The EvtGen 1.2.0 programme [30] is used to model bottom and charm hadron decays.

Events containing jets and a Z boson decaying into two muons are generated at next-to-leading-order (NLO) accuracy in pQCD using the POWHEG BOX 2.0 programme [31]

with the CT10 [32] PDF set. The PS, UE and hadronisation are modelled with PYTHIA8.186 using the CTEQ6L1 [33] PDF set and the AZPHINLO [34] set of tuned parameters.

To estimate systematic uncertainties, the SHERPA2.1.1 [35] generator is used to simulate QCD multi-jet and $Z(\rightarrow \mu\mu)$+jets production. SHERPA uses multi-leg $2 \rightarrow N$ matrix elements that are matched to parton showers following the CKKW [36] prescription. The CT10 PDF set and default SHERPA set of tuned parameters are used. For the studies of the close-by hadronic activity in QCD multijet events, the HERWIG 7.0.4 [37] LO generator with the NNPDF 3.0 NLO [38] parton distribution functions and the H7UE tune [37] was used.

For all the MC simulation samples, multiple pp interactions from the same (in-time pile-up) and neighbouring (out-of-time pile-up) bunch crossings are incorporated by overlaying inelastic minimum-bias events, which are generated with PYTHIA8.210 [39] using the A3 tune [40] and the NNPDF2.3 LO PDF set. The average number of inelastic pp collisions in the same bunch crossing is 13.7, 24.9, and 37.8 in the 2015, 2016, and 2017 datasets, respectively [6].

The particles in the final state produced by all event generators are passed through the full ATLAS detector simulation [41] based on the GEANT4 software tool kit [42]. Tracks, vertices, jets and muons are reconstructed in simulated samples using the same version of the ATLAS software as used to process the data [43]. Finally, the generated events are weighted to reproduce the observed distribution of the average number of collisions per bunch crossing in data.

4 Jet reconstruction

The AR jets are reconstructed with the anti-k_t algorithm and radius parameters $R = 0.2$ and 0.6 using the FASTJET 2.4.3 software package [3]. The inputs to the jet algorithm are massless four-momenta associated with three-dimensional topological clusters known as "topoclusters" [44]. Topoclusters are built from neighbouring calorimeter cells containing a significant energy above a noise threshold that is estimated from measurements of calorimeter electronic noise and simulated pile-up noise. The calorimeter cell energies are initially measured at the EM scale, corresponding to the energy deposited by electromagnetically interacting particles. All ATLAS calorimeters are non-compensating, meaning their response to hadrons is smaller than for electrons or photons with the same energy. The (η, ϕ) coordinates of topoclusters are corrected to point to the hard-scatter primary vertex [45] rather than the centre of the detector, while keeping their energy constant. In addition, corrections for dead material, out-of-cluster losses for pions and calorimeter response for hadronic clusters (identified using their topology and energy density) are implemented with a local cell weighting (LCW) method [44].

Jets are reconstructed from LCW clusters and are required to satisfy a minimum p_{T} threshold of 7 GeV and to be within $|\eta| < 3$. Higher p_{T} thresholds that are used for specific aspects of the analyses are explicitly mentioned in the respective sections. Well-calibrated reference jets used in the *in situ* direct matching method of Sect. 5.2 are reconstructed from topoclusters at the EM scale [4] using the anti-k_t algorithm with radius $R = 0.4$. While this approach creates a dependency of the AR jets reconstructed from topoclusters at the LCW scale on $R = 0.4$ jets reconstructed from topoclusters at the EM scale, their energy scale difference is mitigated by doing the comparisons after simulation-based AR jet calibrations and all $R = 0.4$ jet calibrations are applied.

Tracks from charged particles are used in the jet calibrations and are reconstructed within the full acceptance of the ID ($|\eta| < 2.5$). The track reconstruction uses a neural network clustering algorithm [46]. Reconstructed tracks are required to have $p_{\mathrm{T}} > 500$ MeV and to be associated with the hard-scatter vertex, defined as the primary vertex with at least two associated tracks and the largest $\sum {p_{\mathrm{T}}}^2$ of associated tracks. Tracks must satisfy quality criteria based on the number of hits in the ID subdetectors and are assigned to jets using a ghost association method [47], which ensures that each track is uniquely assigned to a jet.

Muon track segments are used in jet calibration to correct for the uncaptured jet energy from energetic hadrons passing through the calorimeters without being fully absorbed. The segments are partial tracks constructed from hits in the muon spectrometer [48], which serve as inputs to fully reconstructed tracks. Segments are also assigned to jets using the ghost association method.

To determine the energy scale and resolution of jets reconstructed with the ATLAS detector, they are compared with particle-level truth jets. Truth jets are reconstructed with the same algorithm (anti-k_t with $R = 0.2$ and 0.6) using stable, final-state particles from MC generators as input. Candidate particles are required to have a proper life time of $c\tau > 10$ mm, and exclude muons, neutrinos, and particles from pile-up. Truth jets are required to satisfy the same p_{T} threshold of 7 GeV as reconstructed jets, and fall within $|\eta| < 4.5$.

5 Jet energy scale calibrations

The goal of the JES calibration is to match the average JES to that of truth jets. Each calibration step corrects the full four-momentum unless otherwise stated, scaling the jet p_{T}, energy, and mass. The JES calibration consists of two stages:

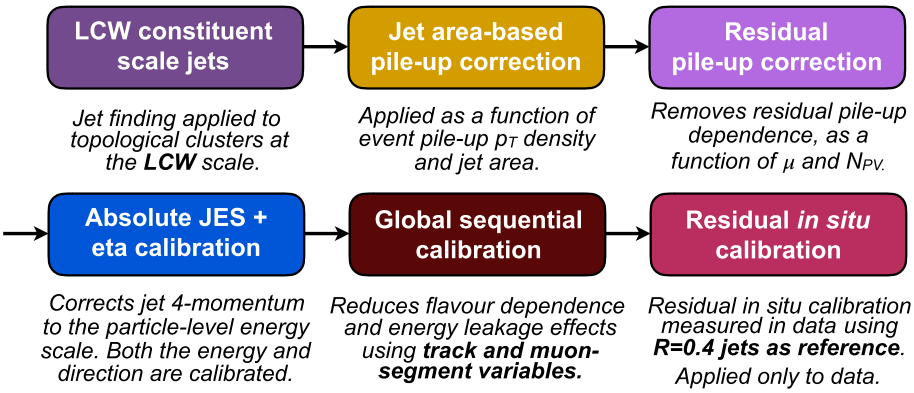

Fig. 2 An overview of the AR reconstruction and calibration scheme. Differences relative to the standard calibration scheme [15] for $R=0.4$ jets reconstructed from EM-scale topoclusters are highlighted in bold font. The global sequential calibration does not take into account calorimeter-based observables as they are already considered in the LCW corrections. The *in situ* correction is derived using $R=0.4$ jets reconstructed from EM-scale topoclusters as a reference

1. In the first stage, MC-based corrections adjust the reconstructed jet four-momentum to match truth jets. These calibrations apply the same "standard" procedure for $R=0.4$ jets detailed in Ref. [15] to AR jets, with modifications discussed in detail in Sect. 5.1.
2. In the second stage, the direct matching method is used to correct jet response differences between data and MC simulation. In this approach, AR jets are compared with fully calibrated anti-$k_t R = 0.4$ [15] jets reconstructed from topoclusters at the EM scale. This stage is discussed in Sect. 5.2.

The individual steps of the calibration procedure (depicted in Fig. 2) are briefly discussed in the following.

5.1 Calibrations based on Monte Carlo simulations

The calibrations based on MC simulations comprise four steps: the jet area-based pile-up correction, the residual pile-up correction, the absolute JES and η calibration, and finally the global sequential calibration.

5.1.1 Jet area-based pile-up correction

Similar to $R = 0.4$ jets, the first calibration step aims to remove the per-event pile-up contribution from the AR jet with a jet area-based correction [15]. In this correction, the catchment area of a jet is defined using the ghost association method and is correlated with its susceptibility to pile-up. The per-unit-area pile-up contribution in y–ϕ space is estimated from ρ, the median p_{T} density of $R=0.4$ jets built with the k_t algorithm [49]. Only the central, lower-occupancy regions of the calorimeter ($|\eta| < 2.0$) are used to calculate ρ, as $\rho \to 0$ for $|\eta| > 2$ due to interplay in occupancy and segmentation [4]. The jet four-momentum is corrected by a scale factor given by the ratio of the pile-up-subtracted jet p_{T} to the uncorrected jet p_{T}, leaving the direction of the jet invariant.

5.1.2 Residual pile-up correction

The jet p_{T} still shows come dependence on the pile-up activity after the jet area-based correction; so a residual pile-up correction is applied. The residual p_{T} dependence on the pile-up is measured as the difference between the reconstructed jet p_{T} before any pile-up correction ($p_{\mathrm{T}}^{\mathrm{reco}}$) and the p_{T} of a matched truth jet following

$$p_{\mathrm{T}}^{\mathrm{corr}} = p_{\mathrm{T}}^{\mathrm{reco}} - \rho \times A - \alpha \times (N_{\mathrm{PV}} - 1) - \beta \times \mu, \qquad (1)$$

where AR jets are considered matched to a truth jet if $\Delta R < 0.3$. The pile-up dependence in Eq. (1) is investigated as a function of the number of reconstructed primary vertices N_{PV} (sensitive to in-time pile-up and parameterised by α) and the average number of interactions per bunch crossing μ (sensitive to the in-time and out-of-time pile-up and parameterised by β) following the procedure from Ref. [4]. The residual p_{T} dependence on N_{PV} and μ is analysed in bins of $|\eta_{\mathrm{det}}|$, and is found to be fairly linear and independent of one another. The jet η pointing from the geometric centre of the detector (η_{det}) is used to remove any ambiguity about which region of the detector the jet is reconstructed. The correction is derived for $20 < p_{\mathrm{T}}^{\mathrm{true}} < 30$ GeV because the importance of the pile-up contamination is greatest in the low-energy region, and the values of the α and β coefficients is taken at $p_{\mathrm{T}}^{\mathrm{true}} = 25$ GeV. To reduce the effects of statistical fluctuations, linear fits are performed to the coefficients in bins of $|\eta_{\mathrm{det}}|$.

The p_{T} dependence on N_{PV} and μ as a function of $|\eta_{\mathrm{det}}|$ before any pile-up correction, and after the area-based and

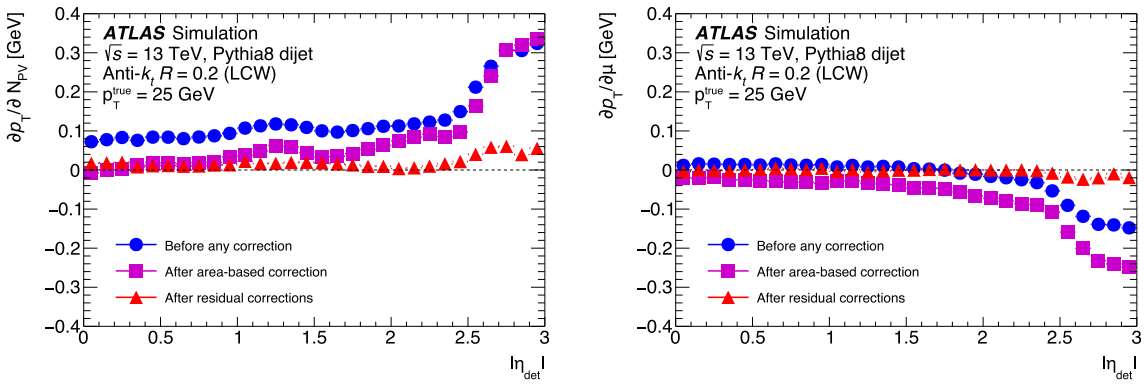

(a) (b)

Fig. 3 Dependence of $R=0.2$ jet p_{T} on **a** N_{PV} as a measure of in-time pile-up and **b** μ that is sensitive to out-of-time pile-up, as a function of $|\eta_{\mathrm{det}}|$ for $p_{\mathrm{T}}^{\mathrm{true}} = 25$ GeV, before any pile-up correction (circles), after the area-based correction (squares), and after the residual corrections (triangles)

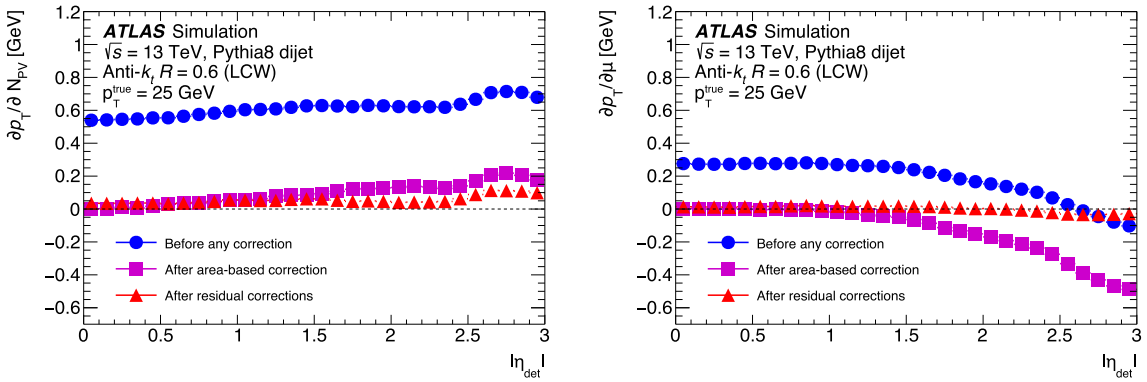

(a) (b)

Fig. 4 Dependence of $R=0.6$ jet p_{T} on **a** in-time pile-up (N_{PV} averaged over μ) and **b** out-of-time pile-up (μ averaged over N_{PV}) as a function of $|\eta_{\mathrm{det}}|$ for $p_{\mathrm{T}}^{\mathrm{true}} = 25$ GeV before any pile-up correction (circles), after the area-based correction (squares), and after the residual corrections (triangles)

residual corrections for $R=0.2$ and $R=0.6$ jets is shown in Figs. 3 and 4. The area-based correction as a function of μ is seen to slightly overcorrect for $R=0.2$ jets. This is due to their smaller catchment area compared to $R=0.4$ jets that affects the sensitivity to pile-up energy, which is corrected by the residual correction. Generally, a stronger residual pile-up dependence is found for $|\eta_{\mathrm{det}}| > 2$ due to different detector geometries and because the jet area-based correction is derived for $|\eta_{\mathrm{det}}| < 2$, as described in Sect. 5.1.1.

5.1.3 Absolute jet energy scale and η calibration

After the pile-up corrections, an absolute jet energy scale and η calibration corrects the reconstructed jet four-momentum to the truth energy scale. This calibration accounts for non-compensating calorimeter response, energy losses in dead material, and biases in the jet η reconstruction. Such η biases are primarily caused by the transition between different calorimeter technologies and sudden changes in calorimeter granularity. The technique used to derive the calibration is the same as the one used for $R = 0.4$ jets, detailed in Ref. [15].

To derive the absolute jet energy scale and η calibration, the AR jets are geometrically matched to truth jets within $\Delta R = 0.3$. In addition, AR (truth) $R=0.2$ jets are required to have no other AR (truth) $R=0.2$ jet of $p_{\mathrm{T}} > 7$ GeV within $\Delta R = 0.6$ ($\Delta R = 1.0$). These selection requirements are tightened to $\Delta R = 0.9$ ($\Delta R = 1.5$) for AR (truth) $R=0.6$ jets. The average response, defined as the mean of a Gaussian function fit to the core of the $E^{\mathrm{reco}}/E^{\mathrm{true}}$ distribution, is measured in narrow bins of E^{true} and η_{det} using a PYTHIA8 MC simulation sample. The response is then parameterised as a function of E^{reco} using a numerical inversion procedure and the jet calibration factor is taken as the inverse of the average energy response, as described in Section 8.3 of Ref. [10]. The average response for AR jets as a function of reconstructed jet p_{T} for representative $|\eta_{\mathrm{det}}|$ bins is shown in Fig. 5. The observed region with lower energy response

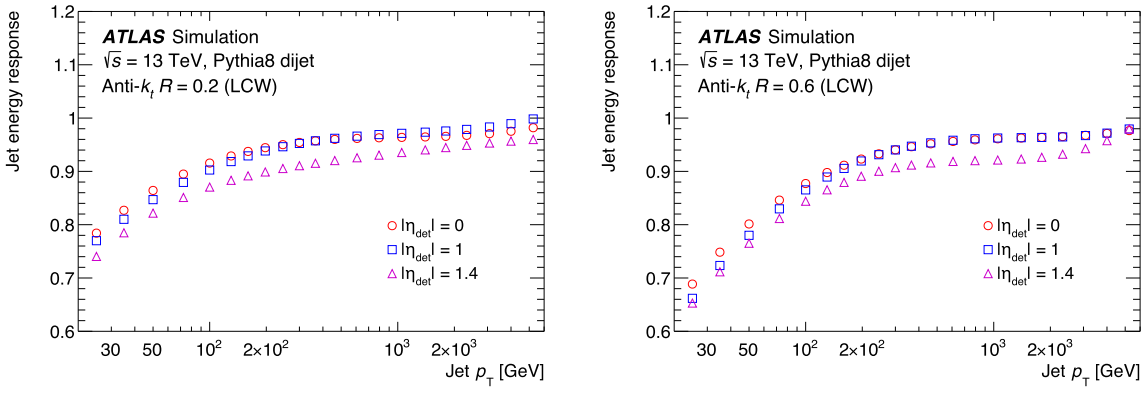

(a) (b)

Fig. 5 The average energy response provided by the calibration method described in the text, as a function of reconstructed jet p_{T} for AR jets with **a** $R=0.2$ and **b** $R=0.6$. The energy calibration factor is given by the inverse of this response

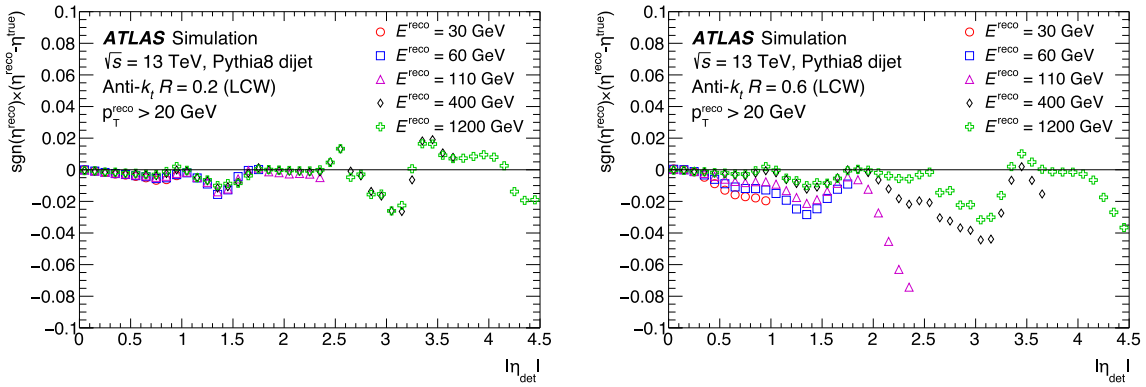

(a) (b)

Fig. 6 The signed difference in η between the reconstructed jet (η^{AR}) and truth jet (η^{true}) for AR jets with $p_{\mathrm{T}}^{\mathrm{reco}} > 20$ GeV and **a** $R=0.2$ and **b** $R=0.6$. This is applied as a correction to the reconstructed jet

at $|\eta_{\mathrm{det}}| \sim 1.4$ corresponds to the barrel-endcap transition region due to absorbed or undetected particles. The average responses tend to be somewhat closer to unity for $R=0.2$ jets compared with $R=0.6$ jets, which is attributed to a better calorimeter response in the energetic core of the jet. Good closure is observed across the entire η_{det} range, except at low E^{true} where a small non-closure of the order of a few percent is seen due to a slightly non-Gaussian energy response caused by jet reconstruction threshold effects.

After the application of the absolute jet energy scale calibration, a difference between the η coordinates of the reconstructed AR jet η^{AR} and that of the matched truth jet η^{true} is observed, as shown in Fig. 6 for $p_{\mathrm{T}}^{\mathrm{reco}} > 20$ GeV as a function of $|\eta_{\mathrm{det}}|$. This is driven by the variations in the energy response of the calorimeters as a function of $|\eta_{\mathrm{det}}|$ that stems from changes in detector technology and geometry [4]. The effect is largest for jets reconstructed in a region spanning calorimeters of different geometry or technology, like in the barrel-endcap ($|\eta_{\mathrm{det}}| \sim 1.4$) and endcap-forward ($|\eta_{\mathrm{det}}| \sim 3.1$) transition regions. This difference, parameterised as a function of E^{true} and η_{det}, is therefore used to apply an additional correction to the η^{AR} coordinate. Again, a numerical inversion procedure is used to derive corrections in E^{reco} bins instead of E^{true} bins. This calibration only alters the jet p_{T} and η, leaving ϕ, E and invariant. AR jets calibrated with the full jet energy scale and η corrections are considered to be at the LCW+JES scale.

5.1.4 *Global sequential calibration*

The detector response to a hadronic jet is sensitive to its composition of various particle types and their momentum fractions, driven by the stochastic nature of parton showering and hadronization. It is also sensitive to stochastic fluctuations in the material interactions producing electromagnetic and hadronic showers in the detector. The former effect is also affected by the jet production mechanism: a quark-initiated jet tends to produce fewer hadrons that hence carry a larger average fraction of the jet p_{T} compared with a gluon initiated jet. Therefore, quark-initiated jets tend to penetrate further

into the calorimeter, while gluon-initiated jets will typically have a lower calorimeter response and a wider transverse profile.

A series of multiplicative corrections, known as the global sequential calibration (GSC) [15], is used to reduce fluctuations in energy and the dependence on the flavour of the parton that initiated the jet, hence advancing the precision of the JES and improving the JER. By construction, the GSC does not change the average jet energy response set by the preceding calibration stage. The jet resolution $\sigma_{\mathcal{R}}$ is defined as the standard deviation of a Gaussian functional fit to the core of the jet response distribution. The GSC is based on global jet observables using tracking information associated with the jet and information related to the activity in the muon chambers behind the jet. As in the previous MC-based calibrations, the AR jets used to derive the GSC are required to be isolated from other jets and to be matched to an isolated truth jet. The GSC procedure is a set of independent and sequential jet four-momentum corrections derived as functions of $p_{\mathrm{T}}^{\mathrm{true}}$, $|\eta_{\mathrm{det}}|$ and a jet observable that is described further down. The GSC is obtained by inverting the reconstructed jet response in simulated events generated with PYTHIA8. In a second step, a numerical inversion is used to obtain calibration factors as a function of $p_{\mathrm{T}}^{\mathrm{AR}}$ instead of $p_{\mathrm{T}}^{\mathrm{true}}$. Three jet observables are found to improve the jet energy resolution:

- n_{track}, the number of tracks with $p_{\mathrm{T}} > 1$ GeV ghost-associated with the jet ($|\eta_{\mathrm{det}}| < 2.5$);
- w^{track}, the average p_{T}-weighted transverse distance in the η–ϕ plane between the jet axis and all tracks of $p_{\mathrm{T}} > 1$ GeV ghost-associated with the jet ($|\eta_{\mathrm{det}}| < 2.5$);
- n_{seg}, the number of muon track segments ghost-associated with the jet ($|\eta_{\mathrm{det}}| < 2.7$).

Another consideration for choosing these GSC observables is that their effects on the jet response have been found to be minimally correlated with one another, reducing the interference between individual GSC corrections. Finally, observables that are typically used for the GSC of jets reconstructed from clusters calibrated at the EM scale, like fractions of the jet p_{T} measured in specific regions of the calorimeter [4], are not used, as they were found to give negligible improvement for jets reconstructed from LCW clusters.

The corrections as a function of n_{track} and w^{track} are derived in fine bins of $\Delta\eta^{\mathrm{AR}} = 0.1$ to account for variations as a function of η^{AR}. The correction based on n_{seg} reduces the tails of the response distribution caused by high-p_{T} jets that are not fully contained in the calorimeters. This correction is derived as a function of jet energy instead of jet p_{T} since it is more correlated with the energy escaping the calorimeters. In this derivation only two η^{AR} regions are used, $0 < |\eta^{\mathrm{AR}}| < 1.3$ and $1.3 < |\eta^{\mathrm{AR}}| < 2.7$, as the muon spectrometer extends to $|\eta| < 2.7$ and two regions are found to be enough to adequately capture the behaviour.

Figure 7 shows the average jet p_{T} response as a function of each of the observables for $R = 0.2$ jets for representative $p_{\mathrm{T}}^{\mathrm{true}}$ ranges and in the most central η^{AR} region. Figure 8 shows the equivalent distributions for $R = 0.6$ jets. The dependence of the jet response on each observable is reduced to less than 2% after the GSC for both $R = 0.2$ and $R = 0.6$ jets.

After the GSC corrections, the fractional jet resolution, defined as $\sigma_{\mathcal{R}}/\mathcal{R}$, where $\mathcal{R}$ is the average jet response, is found to be similar to that reported for $R = 0.4$ jets reconstructed from topoclusters at the electromagnetic scale [15]. The bulk of the improvements are driven by the n_{track} correction, which is applied first and captures the difference of the calorimeter response to jets originating from quarks and gluons. Additional small improvements in the fractional jet resolution are obtained from the w^{track} and n_{seg} corrections. The improvements in the fractional resolution of AR jets due to the combined GSC correction reach up to 10% at $p_{\mathrm{T}} = 20$ GeV and 5% at $p_{\mathrm{T}} = 100$ GeV for both $R = 0.2$ and $R = 0.6$ AR jets. The level of improvement is similar to $R = 0.4$ jets reconstructed from topoclusters at the electromagnetic scale.

5.2 *In situ* calibrations and their combination

The final stage of the jet energy scale calibration corrects for jet response differences between data and MC simulation. Such differences are expected primarily due to an imperfect simulation of the detector (both its energy response and its geometry), but also due to the modelling of the physics processes. Biases in the energy scale due to these effects are corrected for using the direct matching method. Reference jets are reconstructed with the anti-k_t algorithm with radius parameter $R = 0.4$ from topoclusters at the electromagnetic scale. The reference jets are calibrated with the full jet energy scale discussed in detail in Ref. [4], which consists of dedicated MC-based calibrations using the same procedure presented in Sect. 5.1, with two extra GSC stages based on the longitudinal structure of the energy depositions within the calorimeters, and followed by *in situ* calibrations using γ+jet, Z+jet, multijet p_{T} balance techniques, considering data collected in 2015 and 2016 for consistency.

In the direct matching method, AR jets are geometrically matched to a reference jet. Hence, the AR jet and the reference jet are reconstructed using different reconstruction algorithms from similar sets of topoclusters. To cover a wide jet p_{T} range, two topologies are used to derive *in situ* calibrations: multijet and $Z(\rightarrow \mu^+\mu^-)$+jets. The multijet sample is relevant at high p_{T} as its statistical power at $p_{\mathrm{T}} \lesssim 100$ GeV is reduced due to the use of prescaled jet triggers. The Z+jets sample is relevant at low p_{T} due to the clean signature of

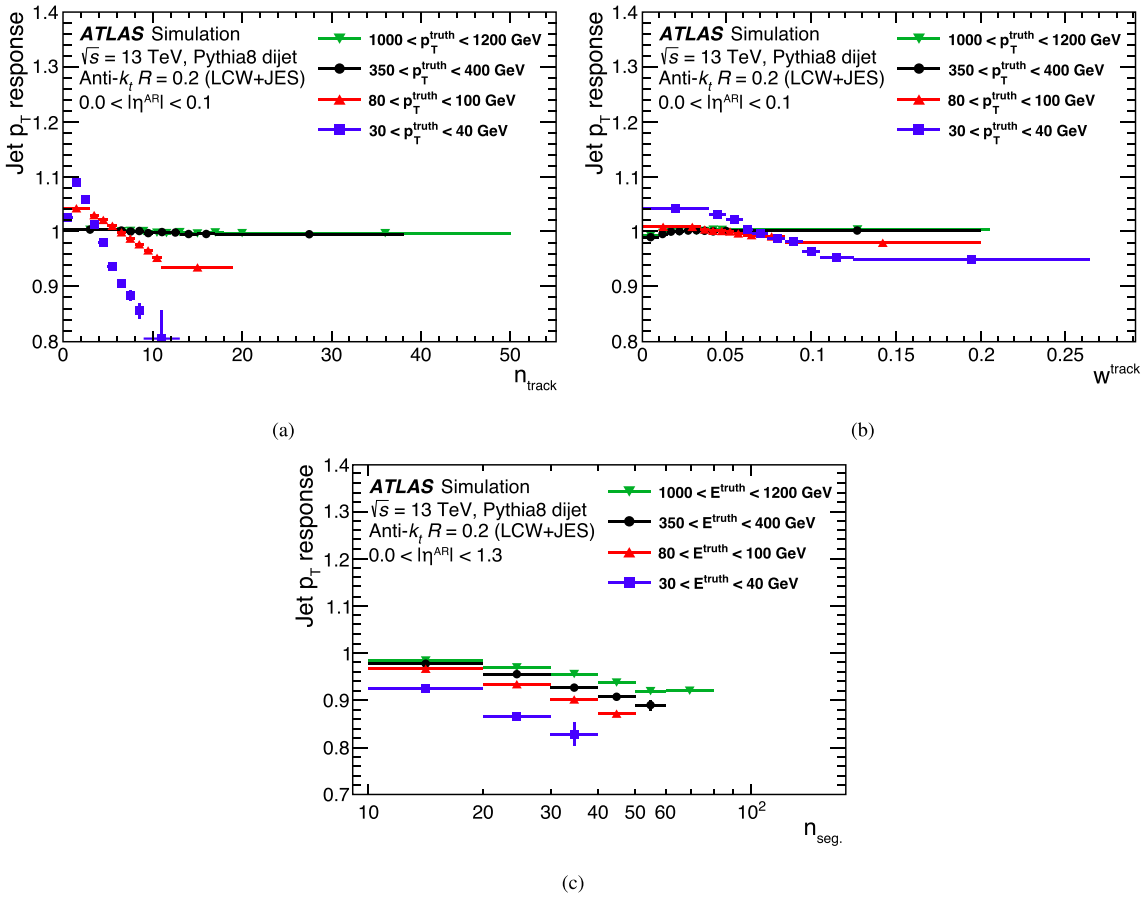

Fig. 7 Average jet p_{T} response as a function of **a** n_{track}, **b** w^{track}, and **c** n_{seg} for AR jets with $R=0.2$ calibrated up to the absolute jet energy and η calibration. The effect as a function of n_{track} and w^{track} is shown in the $0.0 < |\eta^{\mathrm{AR}}| < 0.1$ region, while for n_{seg} the range $0.0 < |\eta^{\mathrm{AR}}| < 1.3$ is used

the muon triggers; however, it is statistically limited for $p_{\mathrm{T}} \gtrsim 200\,\mathrm{GeV}$ due to its steeply falling p_{T} spectrum in combination with lower production cross-section compared with multijet processes.

Events used in the *in situ* calibrations are required to satisfy quality criteria designed to reject events with jets from beam-induced background due to proton losses upstream of the interaction point, cosmic-ray air showers overlapping with collision events and calorimeter noise from large-scale coherent noise or isolated pathological cells, while keeping a high efficiency to select events produced in pp collisions [25]. In addition, events must have at least one reconstructed primary vertex with at least two associated tracks of $p_{\mathrm{T}} > 500\,\mathrm{MeV}$. Furthermore, spurious reference jets from pile-up with $p_{\mathrm{T}} < 60$ GeV and $|\eta_{\mathrm{det}}| < 2.4$ are rejected through the jet vertex tagger (JVT) [50], accepting 92% of the hard-scatter jets and rejecting 98% of the pile-up jets. Pile-up reference jets are only used to ensure that reference jets are isolated from other hadronic activity but otherwise are not considered in the derivation of the *in situ* calibrations.

All isolated jets with $p_{\mathrm{T}} > 20\,\mathrm{GeV}$ and $|\eta| < 3.0$ in the event are selected for the *in situ* direct matching calibration procedure. A jet is considered isolated if the ΔR to the nearest jet reconstructed with the same algorithm and with $p_{\mathrm{T}} > 7$ GeV and $|\eta| < 3.0$ is at least twice the jet radius, i.e., $\Delta R > 0.4$ for $R=0.2$ jets, $\Delta R > 0.8$ for $R=0.4$ jets, and $\Delta R > 1.2$ for $R=0.6$ jets.

The multijet sample is recorded using a suite of single-jet triggers that require an anti-$k_t$jet with $R = 0.4$ reconstructed from topoclusters at the EM scale in the pseudorapidity region $|\eta| < 3.2$. The jet triggers have varying p_{T} thresholds between 15 and 400 GeV. For a given leading jet p_{T} range considered in the *in situ* analysis, the trigger with the highest threshold that is at least 99% efficient is required to have fired.

The Z+jets sample is recorded by the logical OR of two single-lepton triggers: one requiring an isolated muon with $p_{\mathrm{T}} > 20$ (26) GeV for 2015 (2016) data, and another one requiring a muon with $p_{\mathrm{T}} > 50$ GeV without isolation selections. Events with exactly two opposite-charge muons satisfying $|\eta| < 2.4$ and $p_{\mathrm{T}} > 25\,\mathrm{GeV}$ are selected

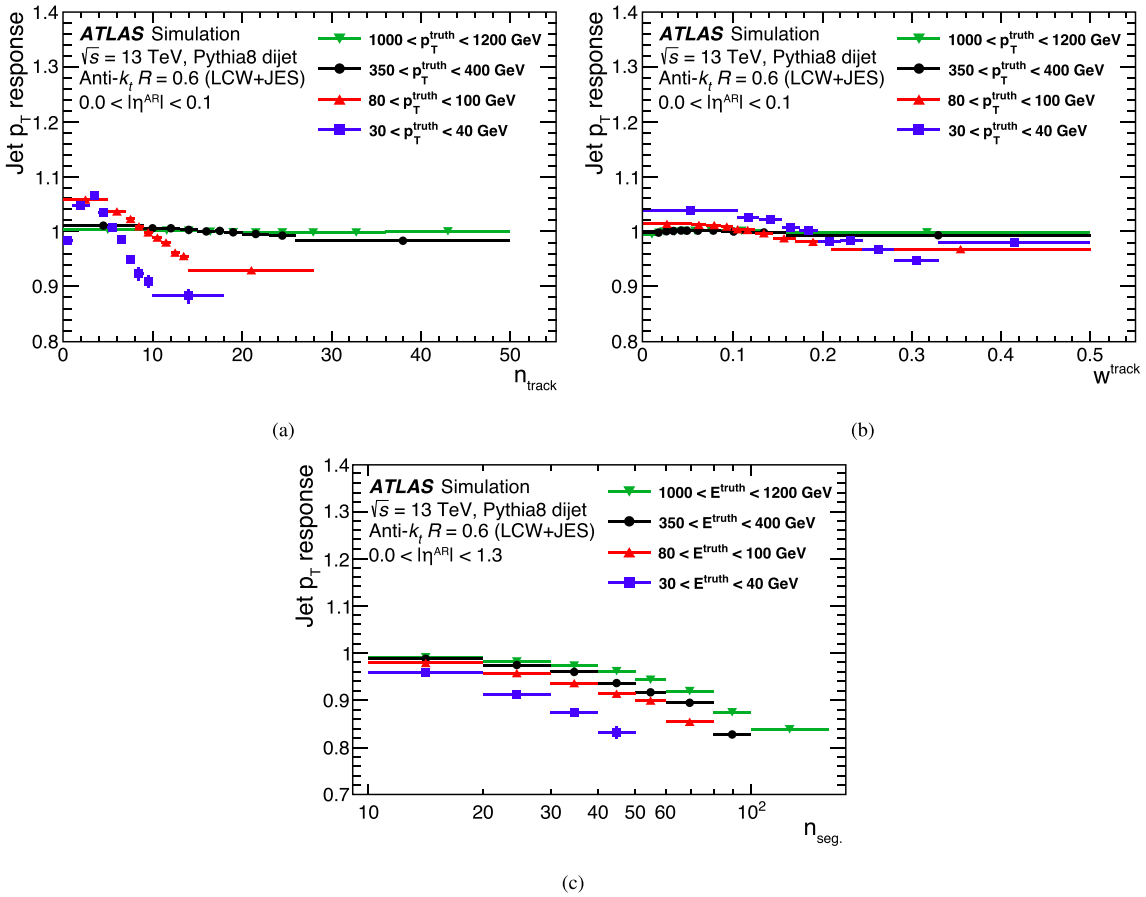

Fig. 8 Average jet p_{T} response as a function of **a** n_{track}, **b** w^{track}, and **c** n_{seg} for AR jets with $R=0.6$ calibrated up to the absolute jet energy and η calibration. The effect as a function of n_{track} and w^{track} is shown in the $0.0 < |\eta^{\mathrm{AR}}| < 0.1$ region, while for n_{seg} the range $0.0 < |\eta^{\mathrm{AR}}| < 1.3$ is used

after full reconstruction. Both muons must satisfy medium (loose) identification (isolation) requirements [48]. Events with a Z boson candidate are identified by requiring $80 < m_{\mu\mu}/\mathrm{GeV} < 116$, where $m_{\mu\mu}$ is the invariant mass of the two muons. Furthermore, both the reference jet and the AR jet with $R=0.2$ are required to satisfy $\Delta R(\text{jet, muons}) > 0.35$. This requirement is increased to 0.6 for $R = 0.6$ jets to account for the larger radius parameter.

The *in situ* calibration is derived for AR jets matched to a reference hard-scatter jet, where a pair of jets is considered matched if $\Delta R(\text{AR, reference}) < 0.2$, which is reasonable given the isolation requirements above. The derivation of the *in situ* calibration factor starts from the *in situ* p_{T} ratio for matched AR–reference jet pairs:

$$\mathcal{R}_{\text{in situ}} = \frac{p_{\mathrm{T}}^{\mathrm{AR}}}{p_{\mathrm{T}}^{\mathrm{ref}}},$$

where $p_{\mathrm{T}}^{\mathrm{AR}}$ is the transverse momentum of an AR jet, and $p_{\mathrm{T}}^{\mathrm{ref}}$ is the p_{T} of the matched reference jet. The calibration is derived only from matched AR–reference jet pairs; in particular in the Z+jet topology the $Z \to \mu\mu$ decay serves only for triggering and topology selection. The average ratio $\langle \mathcal{R}_{\text{in situ}} \rangle$ is extracted by fitting the p_{T} ratio distributions to a Gaussian function in regions of η^{AR} and $p_{\mathrm{T}}^{\mathrm{ref}}$, for η^{AR} bins of size 0.1 and varying bin size for $p_{\mathrm{T}}^{\mathrm{ref}}$ due to its steeply falling production cross-section distribution. The direct matching *in situ* correction factor $\mathcal{C}$ is then defined by:

$$\mathcal{C}(p_{\mathrm{T}}^{\mathrm{ref}}, \eta^{\mathrm{AR}}) = \frac{\langle \mathcal{R}_{\text{in situ}} \rangle_{\mathrm{MC}}}{\langle \mathcal{R}_{\text{in situ}} \rangle_{\mathrm{Data}}}. \tag{2}$$

To derive the *in situ* correction factorsas a function of $p_{\mathrm{T}}^{\mathrm{AR}}$, a translation is applied using the correction factors in Eq. (2). This procedure involves obtaining $\langle p_{\mathrm{T}}^{\mathrm{AR}} \rangle$ for each $(p_{\mathrm{T}}^{\mathrm{ref}}, \eta^{\mathrm{AR}})$ bin, and providing the correction factors $\mathcal{C}$ at $\langle p_{\mathrm{T}}^{\mathrm{AR}} \rangle$ instead of $p_{\mathrm{T}}^{\mathrm{ref}}$.

Figure 9 shows the average p_{T} ratio $\langle \mathcal{R}_{\text{in situ}} \rangle$ in data and MC simulations obtained with PYTHIA8 and SHERPA as a function of $p_{\mathrm{T}}^{\mathrm{ref}}$ for representative η^{AR} bins for AR jets with $R=0.2$ and $R=0.6$ jets in the multijet topology. The observed $\langle \mathcal{R}_{\text{in situ}} \rangle$ tend to be below unity for $R = 0.2$ and above unity for $R = 0.6$ jets due to the difference of the catchment area relative to reference $R = 0.4$ jets. At high

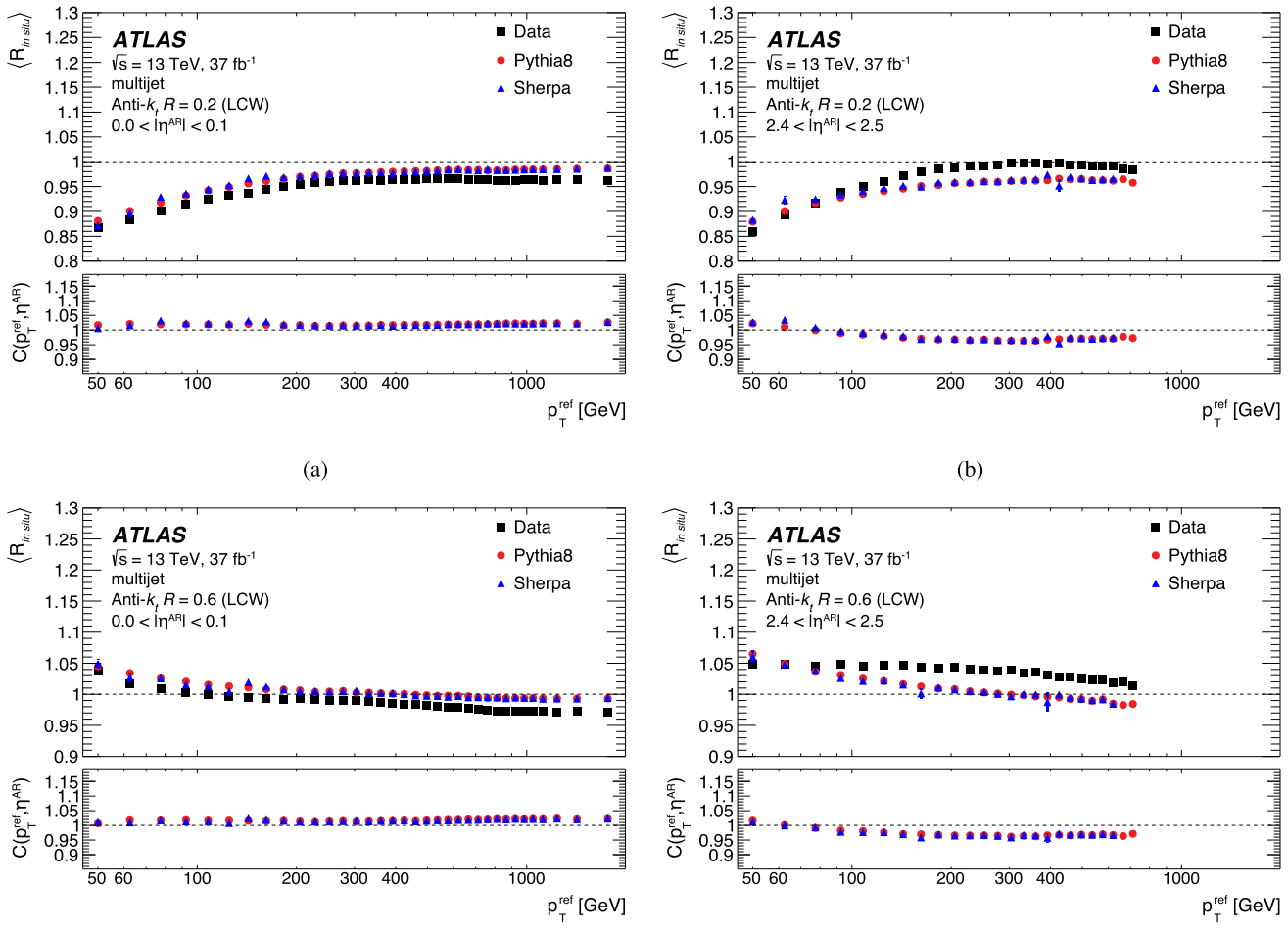

Fig. 9 Average p_{T} ratio $\langle \mathcal{R}_{\mathrm{in\,situ}} \rangle$ as a function of $p_{\mathrm{T}}^{\mathrm{ref}}$ in multijet events from data (squares), PYTHIA8 (circles) and SHERPA (triangles) for $R = 0.2$ jets in the **a** $|\eta^{\mathrm{AR}}| < 0.1$ and **b** $2.4 < |\eta^{\mathrm{AR}}| < 2.5$ regions. The corresponding distributions for $R = 0.6$ jets are shown in panels **c** and **d**. The *in situ* correction factors $\mathcal{C}(p_{\mathrm{T}}^{\mathrm{ref}}, \eta^{\mathrm{AR}})$ are shown in the bottom panels

$p_{\mathrm{T}} \gtrsim 0.5$ TeV where jets are highly collimated, $\langle \mathcal{R}_{\mathrm{in\,situ}} \rangle$ is a couple of percent below unity for $R = 0.6$ jets. This is likely due to small biases from the isolation requirement for $R = 0.4$ jets and from a small non-closure of MC based calibrations because of the merging of electromagnetic and hadronic components. For $R = 0.2$ jets, $\langle \mathcal{R}_{\mathrm{in\,situ}} \rangle$ reaches down to 0.85 at $p_{\mathrm{T}}^{\mathrm{ref}} = 50$ GeV and increases towards unity with greater $p_{\mathrm{T}}^{\mathrm{ref}}$ due to the increasing collimation. The opposite effect is found for $R = 0.6$ jets, where $\langle \mathcal{R}_{\mathrm{in\,situ}} \rangle$ reaches up to 1.05 at $p_{\mathrm{T}}^{\mathrm{ref}} = 50$ GeV and decreases towards unity with greater $p_{\mathrm{T}}^{\mathrm{ref}}$. Similar trends are found across the studied η^{AR} range. Overall, reasonable agreement between data and simulations is found, and the correction factor $\mathcal{C}(p_{\mathrm{T}}^{\mathrm{ref}}, \eta^{\mathrm{AR}})$ ranges within [0.95, 1.05] and tends to fall within a couple of per cent of unity for $\eta^{\mathrm{AR}} < 0.7$.

The average p_{T} ratio $\langle \mathcal{R}_{\mathrm{in\,situ}} \rangle$ in data is also studied in the Z+jets topology, which allows probing low momenta down to $p_{\mathrm{T}}^{\mathrm{ref}} = 20$ GeV. The results found in data and MC simulations with POWHEG +PYTHIA8 and SHERPA are shown in Fig. 10. Similar trends as in the multijet topology are observed. At $p_{\mathrm{T}}^{\mathrm{ref}} = 20$ GeV, $\langle \mathcal{R}_{\mathrm{in\,situ}} \rangle$ reaches down to 0.70 for $R = 0.2$ jets, and up to 1.20 for $R = 0.6$ jets.

As can be appreciated by comparing Figs. 9 and 10, a similar level of agreement between data and MC simulations and hence similar $\mathcal{C}(p_{\mathrm{T}}^{\mathrm{ref}}, \eta^{\mathrm{AR}})$ values are observed for both multijet and Z+jets topologies across the relevant kinematic range. The good agreement is further quantified in Sect. 5.2.1 in Fig. 11. This consistent level of agreement is attributed to the cluster-level LCW correction that captures some of the flavour dependence.

In a closure test after applying the *in situ* calibrations, data and MC simulations are found to typically agree within 0.5%, and the disagreement is never larger than 1%, except for $p_{\mathrm{T}} < 20$ GeV for $R = 0.2$ jets in the Z+jets topology,

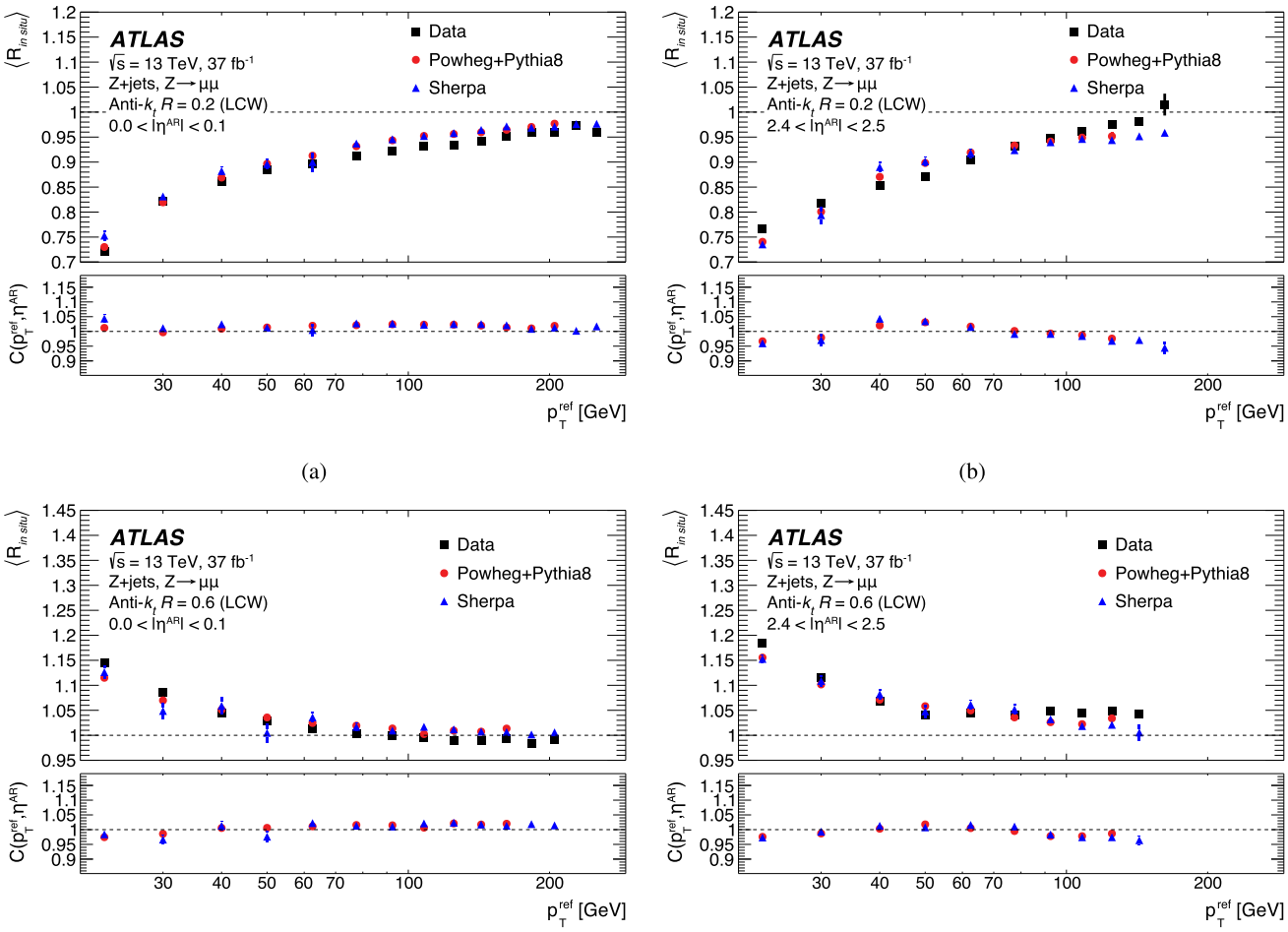

Fig. 10 Average p_{T} ratio $\langle \mathcal{R}_{\mathrm{in\,situ}} \rangle$ as a function of $p_{\mathrm{T}}^{\mathrm{ref}}$ in Z+jets events from data (squares), POWHEG+PYTHIA8 (circles) and SHERPA (triangles) for $R = 0.2$ jets in the **a** $|\eta^{\mathrm{AR}}| < 0.1$ and **b** $2.4 < |\eta^{\mathrm{AR}}| < 2.5$ regions. The corresponding distributions for $R = 0.6$ jets are shown in panels **a** and **b**. The *in situ* correction factors $C(p_{\mathrm{T}}^{\mathrm{ref}}, \eta^{\mathrm{AR}})$ are shown in the bottom panels

where it reaches a couple of percent. This behaviour at low p_{T} is driven by acceptance effects and potential contributions from pile-up events.

5.2.1 *Statistical combination of* in situ *calibrations*

Given the consistency of the *in situ* calibrations in the multijet and Z+jets topologies, the results are statistically combined to assure adequate coverage of the entire p_{T} spectrum and to reduce the overall uncertainty. The statistical combination of calibration results is based on the JES *in situ* combination method described in Ref. [10]. This method combines an arbitrary number of p_{T}-dependent calibrations by assigning a p_{T}-dependent weight to each of them, correctly propagating all the uncertainties and correlations, while minimising the bias from statistical fluctuations and the overall variance caused by systematic uncertainties, which are discussed in the next section. The distribution of the relative weights of the multijet and Z+jets calibrations in representative η bins are shown in Fig. 11a for $R = 0.2$ and Fig. 11b for $R = 0.6$ jets. As expected, the relative contribution from the Z+jet topology dominates at low p_{T}, while for $p_{\mathrm{T}} \gtrsim 100$ GeV the multijet topology takes over. Statistical uncertainties both in the central values and in the systematic variations are assessed using the bootstrap method [51]. The consistency of the two input calibrations is quantified using the $\sqrt{\chi^2/n_{\mathrm{d.o.f.}}}$ metric, which is evaluated as a function of p_{T} and considers the number of degrees of freedom $n_{\mathrm{d.o.f.}}$. In few regions of phase space with $\sqrt{\chi^2/n_{\mathrm{d.o.f.}}} > 1$ the uncertainties in the input calibrations are conservatively rescaled such that $\sqrt{\chi^2/n_{\mathrm{d.o.f.}}} = 1$ is obtained by construction. Example $\sqrt{\chi^2/n_{\mathrm{d.o.f.}}}$ distributions in a representative η bin before applying the rescaling procedure are shown in Fig. 11c and d for $R = 0.2$ and $R = 0.6$ jets, respectively.

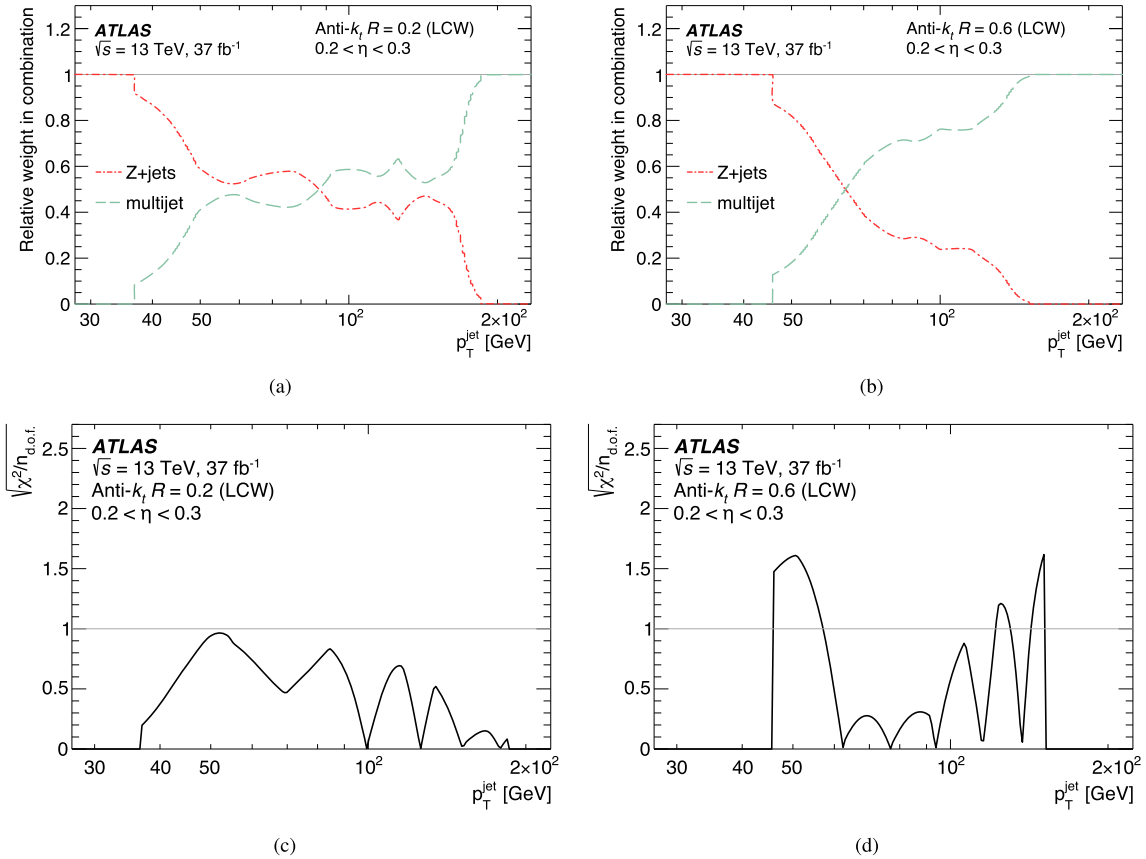

Fig. 11 Relative contributions to the combined *in situ* calibration from the multijet and Z+jet topologies in the $0.2 < \eta < 0.3$ range, for **a** $R=0.2$ and **b** $R=0.6$ jets. Consistency between the *in situ* combination inputs from multijet and Z+jet topologies within their respective uncertainties is quantified through the $\sqrt{\chi^2/n_{\text{d.o.f.}}}$ metric, for **c** $R=0.2$ and **d** $R=0.6$ jets

The JES *in situ* combination method from Ref. [10] described above considers only p_{T}-dependent calibrations. To account for the η_{det} dependence of the calibration factors, the combined calibrations per η_{det} bin are first concatenated into a single (p_{T}, η) dependent distribution, which is shown in Fig. 12a for $R=0.2$ and Fig. 12c for $R=0.6$ jets. The concatenated $(p_{\text{T}}, \eta_{\text{det}})$ dependent distribution is then smoothed with a two-dimensional Gaussian kernel. The kernel parameters are optimised to reduce statistical fluctuations while preserving genuine features of the distribution. The effect of the smoothing is small and examples demonstrating this effect are shown in Fig. 12b and d illustrating the difference between the smoothed distribution and the unsmoothed one. The smoothed *in situ* calibration results are then extended to the uncovered kinematic η_{det}, p_{T}space through a constant extrapolation of the closest neighbouring statistically significant bin across p_{T}, in a given η_{det} range.

The combination procedure considers systematic uncertainties related to the *in situ* direct matching technique. They are captured in the uncertainty category "absolute AR *in situ* JES" that is discussed in Sect. 5.3. Some of these systematic uncertainties are derived with a coarser granularity in η than the calibrations. Hence, the coarse variable-sized binning of the systematic uncertainties in η is mapped onto the regularly spaced 60 η bins of the calibrations. In this procedure, the boundaries of the coarse bins always coincide with those of some of the 60 η bins of the calibrations. The systematic uncertainties are then extended to the uncovered kinematic η, p_{T}space using the same procedure as in the calibrations.

This statistical combination is then performed separately for each of the 60 η_{det} bins in the inputs. The combined $\mathcal{C}(p_{\text{T}}^{\text{ref}}, \eta^{\text{AR}})$ (from Eq. (2)) results are found to be consistent with each individual Z+jet and multijet calibration. This is demonstrated for representative η_{det} bins in Fig. 13 for $R = 0.2$ and $R = 0.6$ jets, where the input calibrations are compared with their combined result and its uncertainty band representing the statistical and systematic uncertainties discussed in Sect. 5.3. The central values of the combined calibration factors remain within a few percent of unity. In the well-instrumented central region with $|\eta| \lesssim 1$ the $\mathcal{C}(p_{\text{T}}^{\text{ref}}, \eta^{\text{AR}})$ factor is approximately constant as a function of p_{T}above 50 GeV, and drops slightly below that, which is due

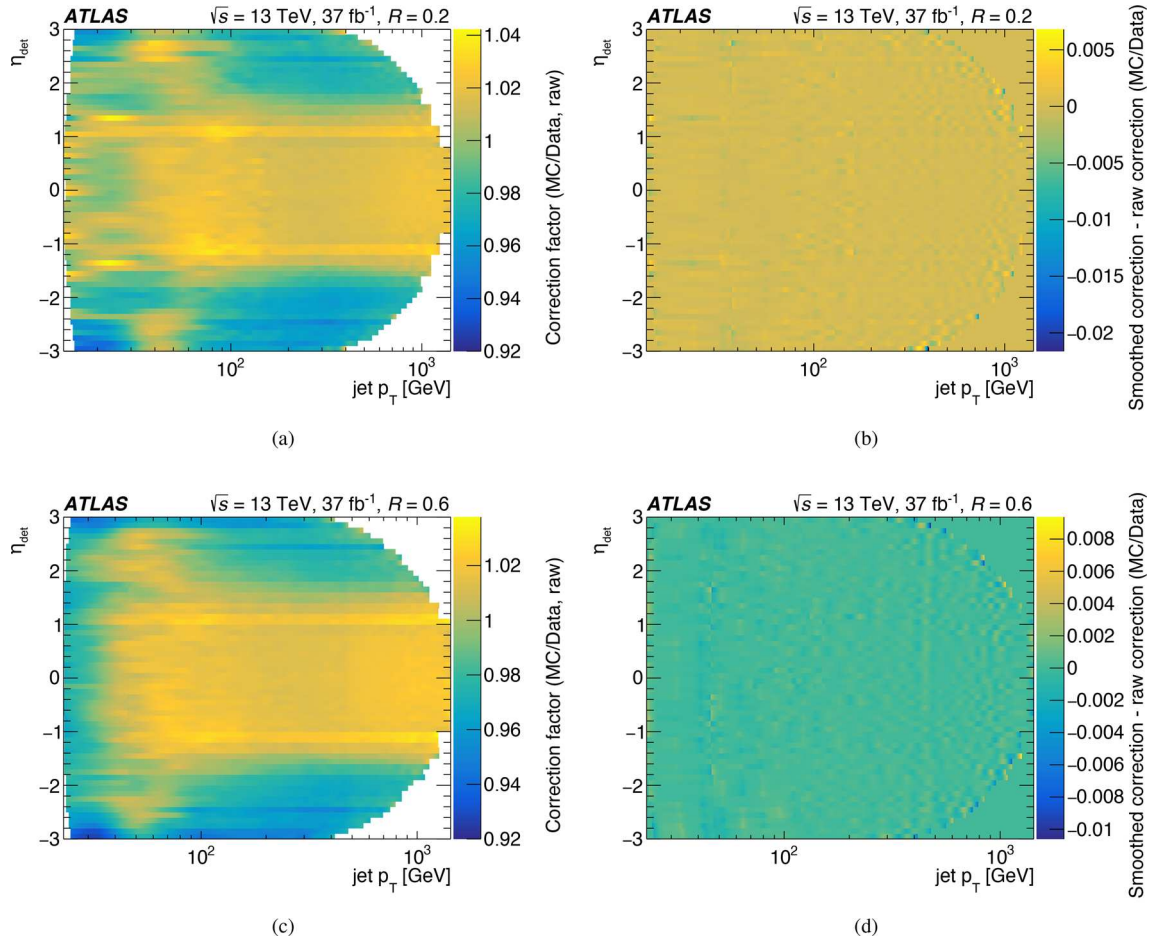

Fig. 12 The effect of the smoothing procedure for the combined calibration. The combined calibration before smoothing (raw) is shown for **a** $R=0.2$ and **c** $R=0.6$ jets. The residual of the smoothing procedure obtained by subtracting the combined calibration parameters after the smoothing from those before the smoothing is shown for **b** $R=0.2$ and **d** $R=0.6$ jets

to single-hadron calorimeter response differences between data and MC simulations [17]. The resulting uncertainties in the combined result, as propagated from the inputs, are typically within a fraction of a percent in the bulk of the distribution, increasing to a couple of percent towards low and high p_{T}.

5.3 Systematic uncertainties

The total uncertainty in the JES consists of 69 individual components. Of those, 18 terms account for uncertainties specific to AR jets derived from the *in situ* measurements, pile-up effects, flavour dependence and MC modelling effects. The other 51 terms correspond to the propagation of uncertainties from the $R=0.4$ reference jets. An additional uncertainty term accounting for the non-closure of the *in situ* measurements for $R=0.2$ jets in the challenging kinematic regime of $p_{\mathrm{T}} < 20$ GeV is provided. These include the absolute and relative *in situ*, punch-through and single-particle response systematic uncertainties. All systematic uncertainties are treated as fully correlated across $p_{\mathrm{T}}$and η, and independent of each other. The sole exception is the case of the JVT-related uncertainty in the absolute *in situ* JES for reference jets and AR jets that are both derived in the Z+jets topology and hence treated as fully correlated.

The uncertainties apply to the entire calibrated phase space defined by $|\eta| < 3$ and $p_{\mathrm{T}} > 20$ GeV or $p_{\mathrm{T}} > 25$ GeV for $R=0.2$ and $R=0.6$ jets, respectively. The calibration phase space can be extended to $p_{\mathrm{T}} > 15$ GeV for $R=0.2$ jets, in which case an additional uncertainty term that accounts for the small non-closure in the $15 < p_{\mathrm{T}} < 20$ GeV range is added. The η boundary was chosen to be slightly larger than the coverage of the tracker of $|\eta| \lesssim 2.5$.

The uncertainties related to the *in situ* direct matching technique are captured in the category "absolute AR *in situ* JES". They include systematic uncertainties due to the choices of topological selections in the direct matching procedure. The value of the angular matching parameter

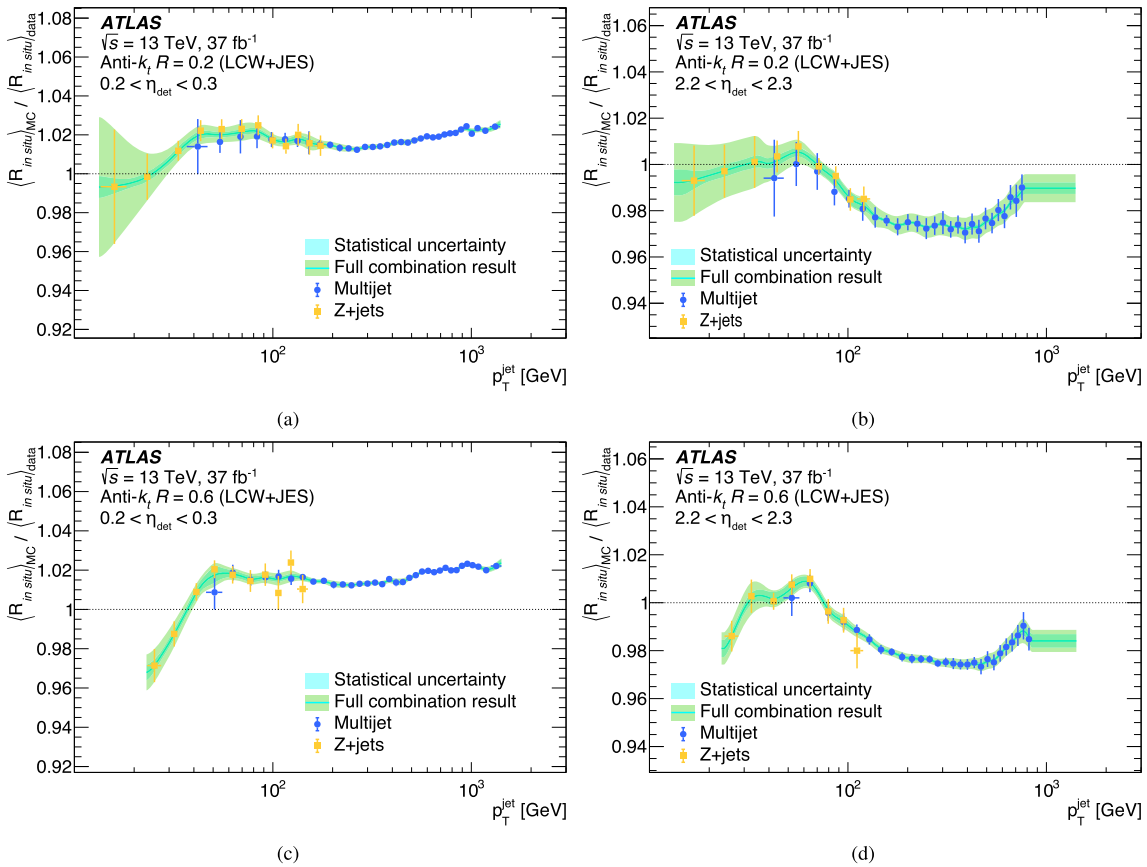

Fig. 13 Combined *in situ* calibration factor together with the individual calibration inputs from multijet and Z+jets events. The ranges of **a** $0.2 < \eta_{\text{det}} < 0.3$ and **b** $2.2 < \eta_{\text{det}} < 2.3$ are shown for $R = 0.2$ jets. The same ranges of **c** $0.2 < \eta_{\text{det}} < 0.3$ and **d** $2.2 < \eta_{\text{det}} < 2.3$ are shown for $R = 0.6$ jets. Uncertainty bands on the full combination result reflect uncertainties from the AR direct matching technique, and do not include propagated *in situ* uncertainties from the reference $R = 0.4$ jets

$\Delta R(\text{AR, ref})$ is varied from its nominal value of 0.2 to values of 0.1 and 0.3. The parameter f for isolation to nearby jets $\Delta R(\text{AR, nearby jet}) > f \times R$ is varied from its nominal value of 2.0 to values of 1.5 and 2.5. The JVT working point [25] is varied from its nominal value of 'medium' to 'loose' and 'tight'. Furthermore, the *in situ* JES calibration using the direct matching method may be sensitive to generator-specific choices and tunings of the parton shower, hadronisation, and matching scale. Therefore a MC modelling uncertainty, estimated by comparing the nominal calibration to the one evaluated using a MC sample generated with SHERPA, is considered.

Since in the *in situ* direct matching technique AR jets are calibrated against $R = 0.4$ anti-k_t reference jets at the EM scale, the uncertainties that apply to those reference jets [4] with a few exceptions discussed in the following are propagated to AR jets. For this propagation, the uncertainties that were originally derived for reference jets are evaluated after scaling them by the ratio of the energy scales of AR jets and reference jets after all calibrations. For consistency, the *in situ* uncertainties documented in Ref. [4] only considering data collected in 2015 and 2016 are used. The propagated uncertainties from $R = 0.4$ anti-k_t reference jets are from the "absolute *in situ* JES" category, which accounts for the *in situ* calibration uncertainties for reference $R = 0.4$ jets in Z+jet and γ + jet, and the "relative *in situ* JES" category, which considers *in situ* calibration uncertainties for reference $R = 0.4$ jets in QCD multijet events.

Several of the systematic uncertainties that were originally evaluated for reference jets are expected to explicitly depend on the jet radius parameter. They are evaluated for AR jets directly instead of propagating the corresponding uncertainties in reference jets. These are the pile-up-related uncertainties, jet flavour related uncertainties, and out-of-cone corrections, which follow the procedures outlined in Refs. [13,14,14,52], respectively.

Finally, two additional sources of uncertainty related to the punch-through correction and to the calorimeter response to highly energetic single particles determined through test-beam measurements and simulations are considered.

Table 1 Summary of the sources of systematic uncertainties in the JES for AR jets, including those propagated from reference jets. Uncertainties marked with an asterisk are derived using reference jets, i.e., anti-$k_t R = 0.4$ jets at the EM scale

Name	Description
Multijet (absolute AR *in situ* JES)	
ΔR matching	Variation of the matching criteria
Isolation	Variation of the isolation requirement
JVT for reference jets	Jet vertex tagger uncertainty
Statistical	Statistical uncertainty over all regions of jet $p_{\mathrm{T}}$and η
Z+jets (absolute AR *in situ* JES)	
ΔR matching	Variation of the matching criteria
Isolation	Variation of the isolation requirement
JVT for reference jets	Jet vertex tagger uncertainty
Statistical	Statistical uncertainty over all regions of jet $p_{\mathrm{T}}$and η
Non-closure	Only $R = 0.2$ jets, accounts for non-closure in Z+jet analysis for the first p_{T}bin.
Pile-up	
μ offset	Uncertainty in the μ modelling in MC simulation
N_{PV} offset	Uncertainty in the N_{PV} modelling in MC simulation
ρ topology	Uncertainty in the per-event p_{T}density modelling in MC simulation
p_{T}dependence	Uncertainty in the residual p_{T}dependence
Jet flavour	
Flavour composition	Uncertainty in the jet composition between quarks and gluons
Flavour response	Uncertainty in the jet response of gluon-initiated jets
b-jet	Uncertainty in the jet response of b-quark-initiated jet
Out-of-cone	Contribution of particles outside the jet cone
Absolute *in situ* JES*	*in situ* calibration uncertainties for reference $R = 0.4$ jets in Z+jet and γ + jet
Relative *in situ* JES*	*in situ* calibration uncertainties for reference $R = 0.4$ jets in QCD multijet events
Punch-through*	Uncertainty in punch-through GSC
Single-particle response*	High-p_{T}jet uncertainty from single-particle and test-beam measurements

The full list of systematic uncertainties considered for AR jets is summarised in Table 1. Figure 14 shows a breakdown of the JES uncertainty into the individual sources for AR jets as a function of $p_{\mathrm{T}}$for $\eta = 0$ and Fig. 15 shows the breakdown as a function of η for $p_{\mathrm{T}} = 60$ GeV. All uncertainties related to the absolute *in situ* calibration of reference jets using Z+jet, γ + jet, and multijet topologies are added in quadrature and shown as "Absolute *in situ* JES ($R = 0.4$)". These uncertainties are dominant for $R = 0.2$ jets, and tend to be dominant at high $p_{\mathrm{T}} \gtrsim 100$ GeV for $R = 0.6$ jets. The uncertainties associated with the relative JES calibration of reference jets between the forward ($0.8 \leq |\eta_{\mathrm{det}}| < 4.5$) and central ($|\eta_{\mathrm{det}}| < 0.8$) regions using QCD multijet production, i.e., the η intercalibration analysis, are also quadratically combined and labelled "Relative *in situ* JES ($R = 0.4$)". These uncertainties apply only to the region $|\eta| > 0.8$ and tend to increase with $|\eta|$, typically not exceeding 1%.

The uncertainties from the absolute *in situ* calibration of AR jets using the direct matching procedure are very small, typically below 0.5% and tend to increase with $|\eta|$. A sample composition of 50% quark jets and 50% gluon jets is assumed, with 100% uncertainties. The uncertainties due to the unknown flavour composition of the jet sample contribute up to a few percent at low $p_{\mathrm{T}} \lesssim 100$ GeV, followed by the uncertainties in the calorimeter response to jets initiated by gluons vs. quarks. For $R = 0.6$ jets, the uncertainty due to pile-up is dominant below $p_{\mathrm{T}} \lesssim 100$ GeV and contributes up to 7%. For $R = 0.2$ jets, this uncertainty is small, at about 0.5%, and the dominant uncertainties are the absolute *in situ* JES of reference jets, closely followed by the uncertainty due to the unknown flavour composition.

The total uncertainty, calculated as the sum in quadrature of all components, is shown in Figs. 14 and 15 as a filled region topped by a solid line. Overall, the total uncertainty for AR jets is of similar magnitude to that of reference jets. This demonstrates the power of the direct matching *in situ* procedure that can be used to calibrate jets with alternative radius parameters.

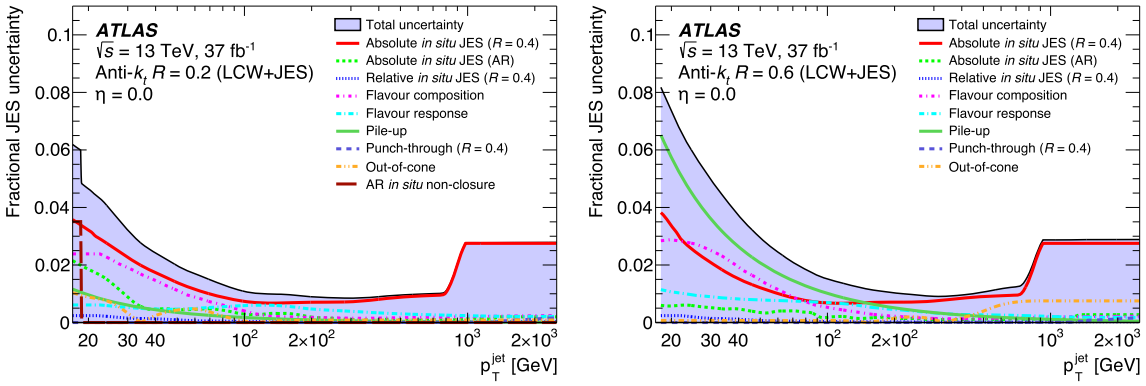

(a) (b)

Fig. 14 Fractional jet energy scale uncertainty components as a function of jet p_{T} at $\eta = 0$ for **a** $R = 0.2$ and **b** $R = 0.6$ jets. The total uncertainty, calculated as the sum in quadrature of all components, is shown as a filled region topped by a solid line. An unknown composition of the sample is assumed in the determination of the flavour terms. The definitions of the uncertainty components are given in Table 1

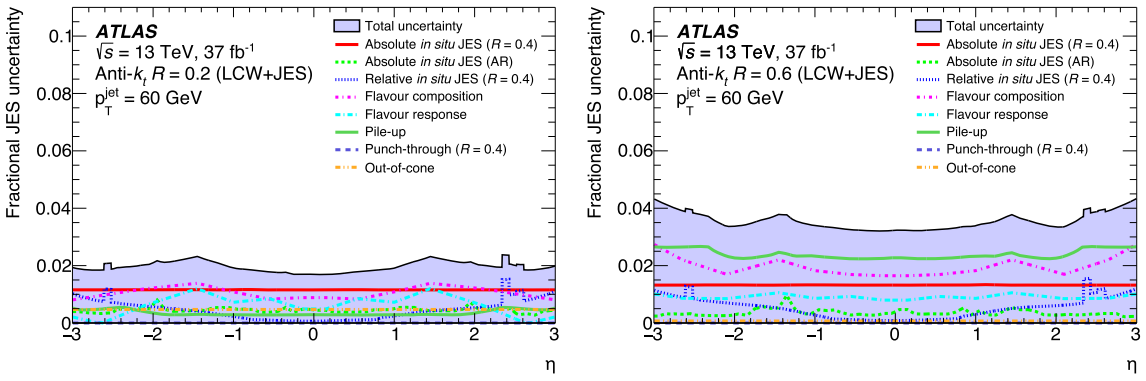

(a) (b)

Fig. 15 Fractional jet energy scale uncertainty components as a function of jet η at $p_{\mathrm{T}} = 60$ GeV for **a** $R = 0.2$ and **b** $R = 0.6$ jets. The total uncertainty, calculated as the sum in quadrature of all components, is shown as a filled region topped by a solid line. An unknown composition of the sample is assumed in the determination of the flavour terms. The definitions of the uncertainty components are given in Table 1

5.3.1 Uncertainty correlations and reductions

The 69 individual uncertainty components preserve correlations between the JES calibrations of individual jets. These correlations are shown as a function of p_{T} in Fig. 16a and b for $R = 0.2$ and $R = 0.6$ jets, respectively, where both jets fall into the central η bin. As expected, the correlations are typically maximal for jets with similar p_{T}, and minimal where the they are very different.

While 69 uncertainty components represent the best estimate of the correlations between JES calibrations, considering all components may be unpractical for data analyses that display a small sensitivity to those correlations. Hence, two simplified uncertainty schemes are provided for these analyses. In both of these schemes, the number of uncertainties is reduced by combining the 44 terms arising from the absolute *in situ* components inherited from the reference jets and the out-of-cone term into a smaller number of uncertainties. This is easily possible since all of those uncertainties are functions of p_{T} only. The standard procedure from Section 5.3.1 of Ref. [4] for the reduction of the number of uncertainties is followed. First, the covariance matrix is built out of the reducible, i.e., p_{T}-dependent terms, as shown in Fig. 16a and b for $R = 0.2$ and $R = 0.6$ jets, respectively. This correlation matrix is then diagonalized and the eigenvectors corresponding to the largest eigenvalues are kept and treated as new independent effective uncertainty components. The remaining eigenvector components are then quadratically combined into a single residual uncertainty term. The number of effective uncertainty components retained is determined by the uncovered correlation loss, which is measured by the maximum absolute difference

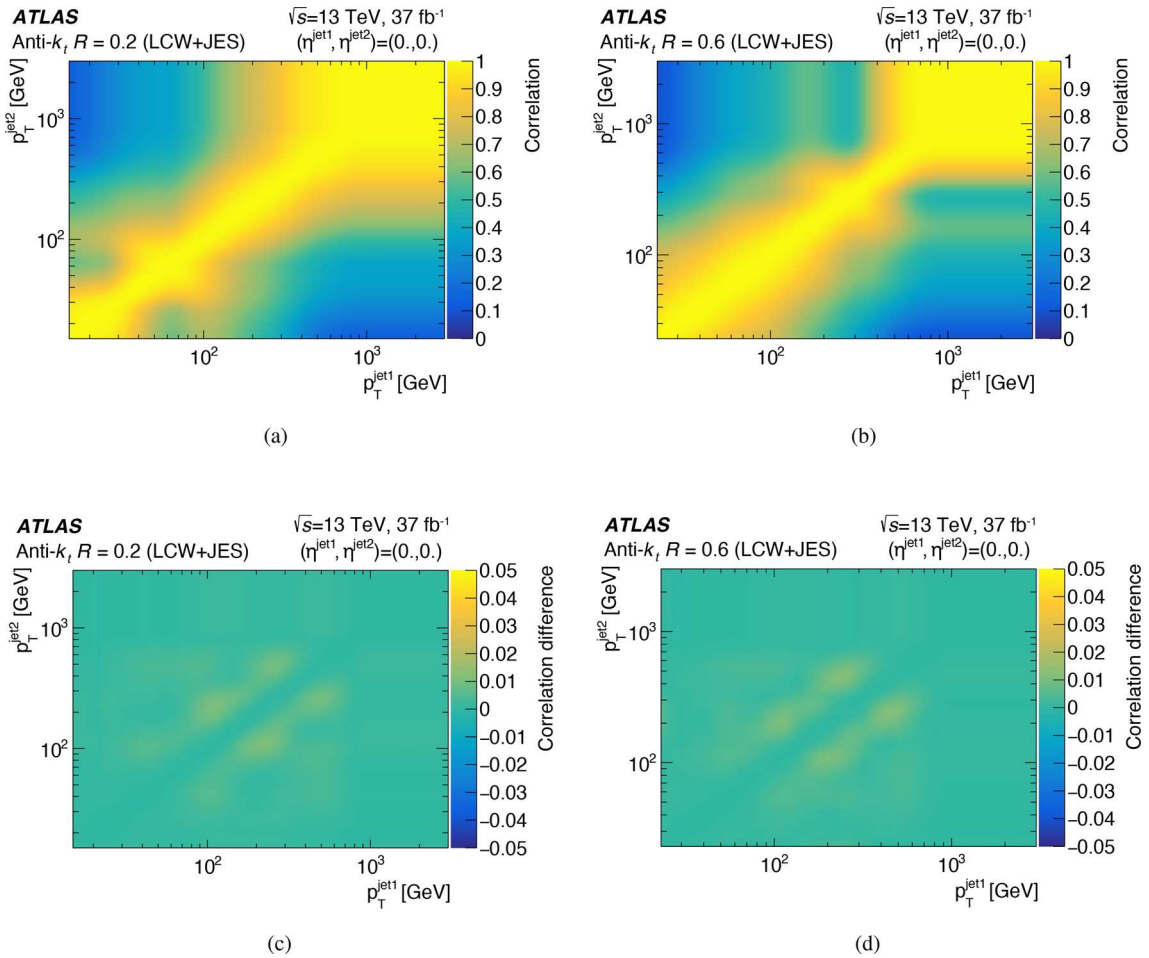

Fig. 16 Correlations of the JES calibration between pairs of **a** $R=0.2$ and **b** $R=0.6$ jets at $\eta=0$ using the full reducible set of 45 p_{T}-dependent *in situ* uncertainty components. Difference between the pair-wise JES correlations for the full reducible set of uncertainty components and the reduced per category set for **c** $R=0.2$ and **d** $R=0.6$ jets, yielding a maximum correlation difference close to 0.01 for both jet radii

observed between the correlations for the full and reduced set of uncertainties.

In the first reduction scheme, all the reducible uncertainty components are considered in the reduction procedure, independent of their origin. This results in 7 (8) effective nuisance parameters for the $R=0.2$ ($R=0.6$) jets, adding up to a total count of 30 (31) nuisance parameters, keeping the uncovered correlation loss around 0.02 (0.01). In the second reduction scheme the uncertainties are grouped into categories with the same origin (detector, statistical, modelling or mixed) and a reduction procedure is performed separately for each of these categories. This results in 17 effective terms, for a total count of 40 nuisance parameters for AR jets. The uncovered correlation loss is close to 0.01 for both jet radii, as shown in Fig. 16c for $R=0.2$ and Fig. 16d for $R=0.6$ jets.

6 Jet energy resolution

Similar to the JES, a precise knowledge of JER is important for all measurements involving jets, ranging from precision measurements of jet production rates or of the top quark mass, to searches for physics beyond the Standard Model.

The dependence of the relative JER $\sigma(p_{\mathrm{T}})/p_{\mathrm{T}}$ on the transverse momentum of the jet may be parameterised using a functional form expected for calorimeter-based resolutions, with three independent contributions:

$$\frac{\sigma(p_{\mathrm{T}})}{p_{\mathrm{T}}} = \frac{N}{p_{\mathrm{T}}} \oplus \frac{S}{\sqrt{p_{\mathrm{T}}}} \oplus C. \tag{3}$$

The noise term N is due to the contributions from pile-up in the detector and due to the effect of electronic noise on

the measured detector signal. Since both contribute directly to the energy measured in the calorimeter but are approximately independent of the energy deposited from the hard momentum transfer interaction, the relative noise term contribution to the JER scales as p_{T}^{-1}. The noise term is expected to be significant in the low-p_{T} region, below ~ 30 GeV. Statistical fluctuations in the amount of energy registered by the ATLAS calorimeter, especially considering its sampling concept, are captured by the stochastic term S. This term represents the limiting term in the resolution up to several hundred GeV. The relative contribution of the S term to the JER scales as $p_{\mathrm{T}}^{-1/2}$. The constant term C corresponds to effects that are a constant fraction of the jet p_{T}, such as the starting point of the hadron showers and non-uniformities of response across the calorimeter. The C term is expected to dominate the high-p_{T} region, above approximately 0.5 TeV.

The contribution from the N term that dominates the JER at low jet momenta is determined using dedicated methods that are sensitive to both pile-up and electronics noise. This measurement and the associated systematic uncertainties are discussed in Sect. 6.1. The noise term is then used as an external constraint when measuring the JER in the $p_{\mathrm{T}} > 50$ GeV regime with the direct balance method, which uses the requirement that the two leading jets, reconstructed with the same algorithm and the same calibrations, be balanced against one another in a well-defined dijet system. This method, together with the final JER results, is presented in Sect. 6.2. Finally, the systematic uncertainties in the JER measurement from the direct balance method are estimated in Sect. 6.3.

6.1 Noise measurement with the random cones method

The noise term N in Eq. (3) captures the contributions from both pile-up noise N_{PU} and noise from other factors $N_{\mu=0}$. The two contributions are measured independently and N is taken to be the quadrature sum of N_{PU} and $N_{\mu=0}$. To determine the N_{PU} contribution, the random cones method is applied to 2.4 pb^{-1} of randomly triggered, i.e., "zero-bias," data to measure the energy deposits within $R = 0.2$ and $R = 0.6$ cones. A dedicated dijet MC simulation sample with $\mu = 0$ is analysed to determine $N_{\mu=0}$ originating from factors other than pile-up such as electronics noise. This sample was generated as described in Sect. 3 but without any pile-up overlay. This methodology is detailed in Refs. [4,14] for $R = 0.4$ jets. Therefore, the following discussion focuses on quantitative results when applying this procedure to AR jets.

In the random cones method, the fluctuations in energy deposits due to pile-up are estimated by taking the difference between two randomly distributed cones analogous to the jet area for AR jets, since the pile-up energy deposits are randomly distributed in ϕ. The energy deposits inside a cone are summed at the energy scale of the jet constituents, i.e., LCW scale topo-clusters. The cone radius is taken to be the same as the radius parameter of AR jets, i.e., $R = 0.2$ and $R = 0.6$. For each event, multiple non-overlapping cone pairs on opposite sides of the detector in η and within a restricted $|\eta|$ range are selected to account for the different detector technologies across $|\eta|$. The random cone p_{T} balance of a cone pair C_1 and C_2 is given by

$$\Delta p_{\mathrm{T}}^{\mathrm{RC}} = p_{\mathrm{T}}^{\mathrm{C}_1} - p_{\mathrm{T}}^{\mathrm{C}_2}. \tag{4}$$

An example $\Delta p_{\mathrm{T}}^{\mathrm{RC}}$ distribution for $R = 0.6$ cones within $|\eta| < 0.7$ is shown Fig. 17a. The pile-up noise at constituent scale $N_{\mathrm{PU}}^{\mathrm{constituent}}$ is hence estimated as one-half of the central 68% confidence interval σ_{RC} of the $\Delta p_{\mathrm{T}}^{\mathrm{RC}}$ distribution divided by $\sqrt{2}$. The resulting measurements of $N_{\mathrm{PU}}^{\mathrm{constituent}}$ are given in Fig. 17b as a function of μ. As expected, $N_{\mathrm{PU}}^{\mathrm{constituent}}$ increases with growing R parameter values. To estimate the JER contribution from pile-up noise N_{PU} for a fully calibrated jet, the nominal JES calibration factors are applied to $N_{\mathrm{PU}}^{\mathrm{constituent}}$.

The noise $N_{\mu=0}$ originating from factors other than pile-up such as electronics noise, is extracted from MC events that are simulated without any pile-up overlay. This is done by extracting the JER from those pile-up-free MC simulations using truth jet information and fitting the results with the standard JER parameterisation in Eq. (3) to extract the N term.

The total noise terms along with their systematic uncertainties are shown in Fig. 18 for AR jets with $p_{\mathrm{T}} = 30$ GeV. Generally, the N term is larger for $R = 0.6$ than for $R = 0.2$ jets, as expected from the radius parameters. For both $R = 0.2$ and $R = 0.6$ jets, the magnitude of the N term is influenced by the detector layout and is largest in the inter-cryostat region around $|\eta| \approx 1.5$. This dependence on $|\eta|$ is more pronounced for $R = 0.2$ jets because of their smaller catchment area, which reduces averaging effects across detector regions that are prominent for $R = 0.6$ jets. A comparison with Ref. [4] shows that the N term is larger for AR jets reconstructed from topoclusters calibrated at the LCW scale compared with particle-flow jets. This is because LCW clusters do not benefit from the matching to low-p_{T} tracks.

The systematic uncertainties affecting the N_{PU} measurement using the random cone measurement are dominated by the non-closure of the method. It is estimated by comparing the N_{PU} derived in zero-bias MC events to an alternative derivation that takes the quadratic difference of the JER determined in MC events with and without pile-up. Other, typically small, systematic uncertainties are related to the conversion from $N_{\mathrm{PU}}^{\mathrm{constituent}}$ to N_{PU}, variations in the σ_{RC} definition, and the parameterisation of the fit function used to extract N_{PU} that includes an additional term proportional to $p_{\mathrm{T}}^{-1.5}$.

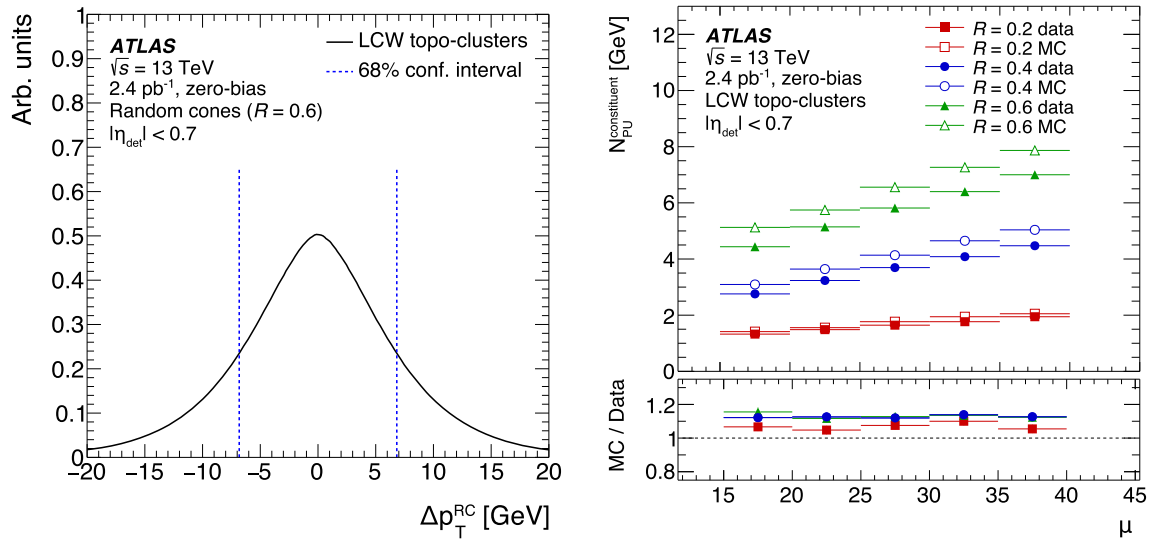

(a) (b)

Fig. 17 **a** The difference of energy deposits $\Delta p_{\mathrm{T}}^{\mathrm{RC}}$ within two randomly chosen cones with $R = 0.6$, measured in the central detector region ($|\eta| < 0.7$) in randomly triggered data using topoclusters calibrated at the LCW scale. The vertical dotted lines indicate the 68% confidence interval. **b** The pile-up noise N_{PU} at the energy scale of topoclusters calibrated at the LCW scale, estimated with the random cones method in the central detector region ($|\eta| < 0.7$), as a function of the number of hard pile-up interactions μ is compared between data (filled markers) and MC (open markers). Only statistical uncertainties are considered, but are hidden by the markers. The ratio of MC simulation to data is shown in the bottom panel

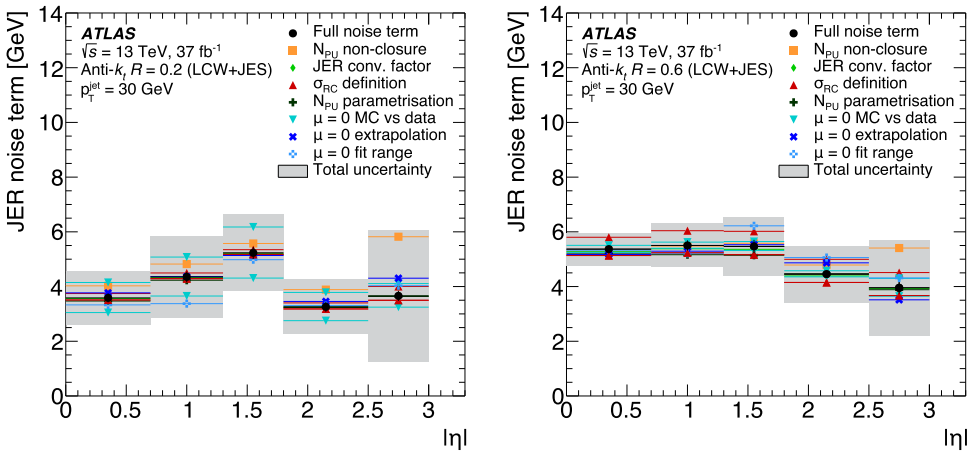

(a) (b)

Fig. 18 Noise term due to pile-up and electronics noise estimated by using the random cones method and its uncertainties as a function of η for **a** $R = 0.2$ jets and **b** $R = 0.6$ jets with $p_{\mathrm{T}} = 30$ GeV. The full noise term is shown as a solid circle marker, while other symbols indicate systematic variations

The systematic uncertainties related to the $N_{\mu=0}$ extraction tend to be dominated by the JER difference between MC simulations without pile-up and low-μ data taken in 2010 [12]. Other systematic uncertainties account for the non-closure of the method, which is estimated by simulating MC events at different μ values and extrapolating to $\mu = 0$, and the impact of the fit range when extracting $N_{\mu=0}$ in the fit with the standard JER parameterisation from Eq. (3).

6.2 Resolution measurement with the direct balance method

Dijet events have two jets that are well-balanced in the transverse direction. Hence, the dijet topology is used to measure the JER using the dijet balance method that relies on the approximate scalar balance between the transverse momenta of the two leading jets. The direct balance method is detailed in Ref. [4] and will only be summarised briefly here.

The goal of the direct balance method is to probe deviations in the balance between two jets via the asymmetry

$$\mathcal{A} \equiv \frac{p_{\mathrm{T}}^{\mathrm{probe}} - p_{\mathrm{T}}^{\mathrm{ref}}}{p_{\mathrm{T}}^{\mathrm{avg}}}, \tag{5}$$

where $p_{\mathrm{T}}^{\mathrm{ref}}$ is the p_{T} of a reference jet that must fall in the central calorimeter region $0.2 \leq |\eta_{\mathrm{det}}| < 0.7$, and $p_{\mathrm{T}}^{\mathrm{probe}}$ is the p_{T} of a probe jet within $|\eta_{\mathrm{det}}| < 3$. Both probe and central jet are defined consistently using the same R parameter, i.e., either both $R=0.2$ or both $R=0.6$.

The standard deviation of the asymmetry in Eq. (5) $\sigma_{\mathcal{A}}$ may be generally expressed as

$$\sigma_{\mathcal{A}}^{\mathrm{probe}} = \frac{\sigma_{p_{\mathrm{T}}}^{\mathrm{probe}} \oplus \sigma_{p_{\mathrm{T}}}^{\mathrm{ref}}}{\langle p_{\mathrm{T}}^{\mathrm{avg}} \rangle} = \left\langle \frac{\sigma_{p_{\mathrm{T}}}}{p_{\mathrm{T}}} \right\rangle^{\mathrm{probe}} \oplus \left\langle \frac{\sigma_{p_{\mathrm{T}}}}{p_{\mathrm{T}}} \right\rangle^{\mathrm{ref}},$$

where $\sigma_{p_{\mathrm{T}}}^{\mathrm{probe}}$ and $\sigma_{p_{\mathrm{T}}}^{\mathrm{ref}}$ are the resolutions of $p_{\mathrm{T}}^{\mathrm{probe}}$ and $p_{\mathrm{T}}^{\mathrm{ref}}$ and $p_{\mathrm{T}}^{\mathrm{avg}}$ is the mean $p_{\mathrm{T}}^{\mathrm{avg}} = (p_{\mathrm{T}}^{\mathrm{probe}} + p_{\mathrm{T}}^{\mathrm{ref}})/2$. The relationship above allows to extract the resolution of the probe jet from the measured $\mathcal{A}$ distribution by quadratically subtracting $\left\langle \frac{\sigma_{p_{\mathrm{T}}}}{p_{\mathrm{T}}} \right\rangle^{\mathrm{ref}}$.

The measured $\mathcal{A}$ distribution is affected on an event-by-event basis by effects such as the underlying event, additional radiation, non-perturbative processes such as hadronisation, and others that may lead to particle losses and additions in the measured jets. Consequently, the measured dijet balance asymmetry distribution represents a convolution of those effects with the intrinsic detector resolution. The intrinsic detector resolution is extracted by determining the width parameter of a Gaussian kernel convolution of the $\mathcal{A}$ distribution obtained using truth jets, where the kernel mean captures the residual non-closure of the calibration. The truth level $\mathcal{A}$ is determined using PYTHIA8 MC simulation following the same event-level selection criteria that are used for the measurement at detector level, which are then fitted with an ad hoc function based on exponential functions [14].

The direct balance measurement uses collision data recorded by the same suite of jet triggers as in the *in situ* JES measurement, where the triggers are selected to be at least 99% efficient in a given range of $p_{\mathrm{T}}^{\mathrm{avg}}$. The $p_{\mathrm{T}}^{\mathrm{avg}}$ range for a given trigger p_{T} threshold tends to be lower for $R=0.2$ jets due to their smaller catchment area than for $R=0.6$ jets. To minimise any effects from pile-up, the AR jets must satisfy the same JVT selection requirements as in the *in situ* JES measurement.

Topological selection criteria are applied to obtain a sample enriched in dijet production processes with minimal contributions from additional radiation or higher-order processes. The azimuthal angle $\Delta\phi$ between the two leading jets in the event must fulfil $\Delta\phi \geq 2.7$. Events with an energetic third jet $p_{\mathrm{T}}^{j_3}$ with $p_{\mathrm{T}}^{j_3} > \max(25\ \mathrm{GeV}, 0.25 \cdot p_{\mathrm{T}}^{\mathrm{avg}})$ are vetoed.

Example $\mathcal{A}$ distributions are compared between truth jets in MC simulations and reconstructed jets in data for $R=0.2$ and $R=0.6$ jets in two representative bins of $p_{\mathrm{T}}^{\mathrm{avg}}$ and η_{det} in Fig. 19. As expected, the JER is generally better for $R=0.6$ jets than for $R=0.2$ jets since the larger jet cone allows to better capture the energy of the particle shower at the origin of the jet before any interaction with the detector. As an overall trend, the JER improves with increasing $p_{\mathrm{T}}^{\mathrm{avg}}$ and is generally superior in better instrumented central detector regions.

Figure 20 shows the individual measurements of the JER in a representative range of $0.2 < |\eta| < 0.7$ for $R=0.2$ and $R=0.6$ jets. These JER measurements obtained with the direct balance method presented above are combined using a chi-squared minimisation of the function in Eq. (3). In this fit, the N term is a constant set to the central value found in Sect. 6.1 for a given η bin, while the S and C terms are free parameters to be determined. The S and C terms tend to be strongly anti-correlated. Generally, the data are reasonably well described by the parameterisation of the detector resolution according to Eq. (3), which is indicated by an approximately flat χ^2 probability distribution ranging between 0.0 and 1.0 for all kinematic regions studied.

6.3 Systematic uncertainties

The uncertainties in the S and C terms are estimated by re-evaluating the JER measurement after a 1σ shift of each of the individual uncertainty sources. These encompass uncertainties in the direct balance method itself, the JES calibration of AR jets and hence the JES calibration of $R=0.4$ jets.

For the uncertainties in the direct balance method itself, the established procedure from Ref. [4] is followed. These uncertainties tend to be dominated by the uncertainty due to the ad hoc selections defining the dijet topology such as the $\Delta\phi$ requirement and the extra jet veto. These uncertainties are evaluated by independently varying the selection values up ($\Delta\phi \geq 2.9$ and $p_{\mathrm{T}}^{j_3} < \max(20\ \mathrm{GeV}, 0.20 \cdot p_{\mathrm{T}}^{\mathrm{avg}})$) and down ($\Delta\phi \geq 2.5$ and $p_{\mathrm{T}}^{j_3} < \max(30\ \mathrm{GeV}, 0.30 \cdot p_{\mathrm{T}}^{\mathrm{avg}})$). Another important uncertainty is the method closure. This uncertainty is obtained by comparing the JER measured in MC with the direct balance method with the JER obtained by comparing the transverse momenta of reconstructed jets and the truth jet to which they are matched. Sub-dominant uncertainty contributions come from modelling of dijet events in MC simulations, the JVT requirement, and the finite number of events in the dijet sample used in direct balance measurements. The uncertainties in the JES calibration of AR jets as per Sect. 5.3 are considered and propagated through the S, C fit. Typically, all the uncertainties in the direct balance method display a very weak dependence on jet p_{T}, and tend to grow with increasing $|\eta|$.

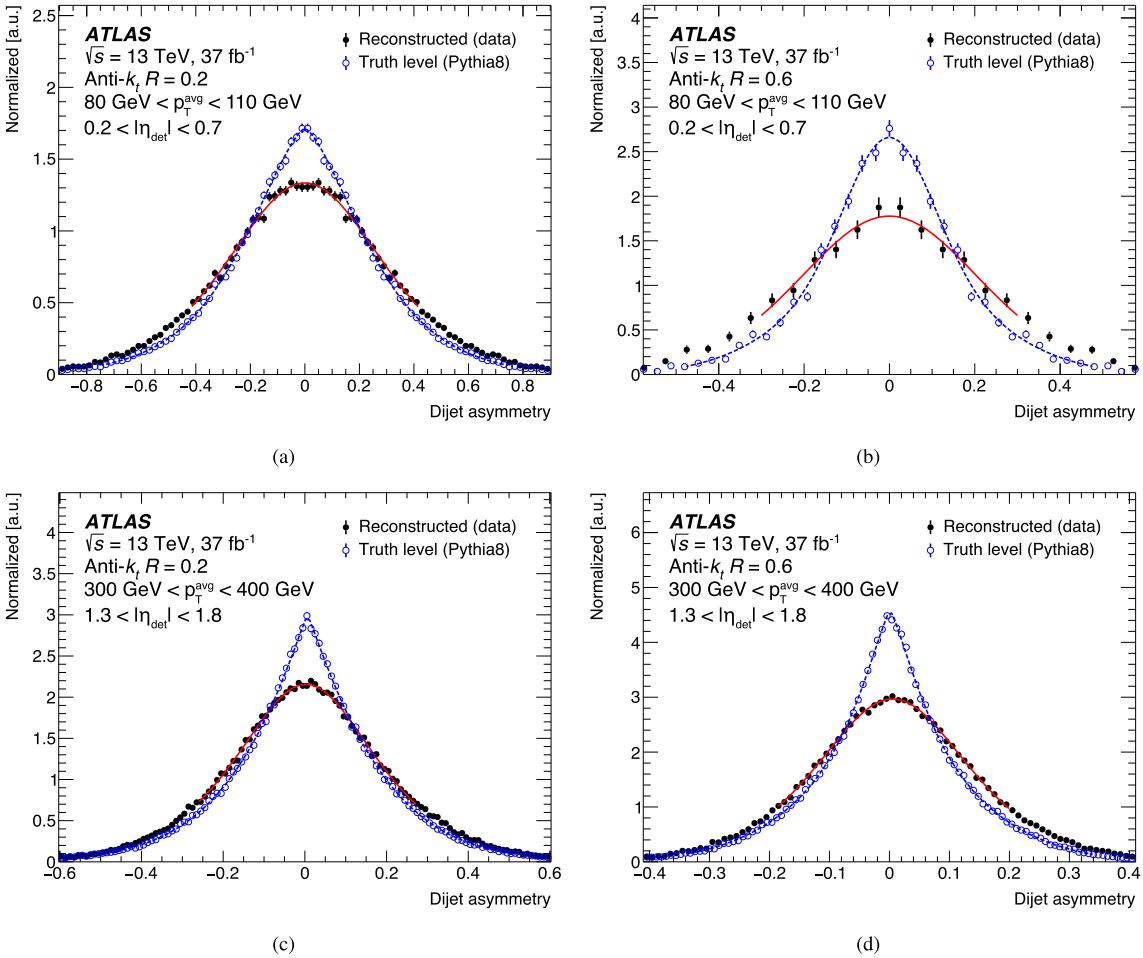

Fig. 19 Reconstructed (solid markers) asymmetry of the jet system in data in the range of 80 GeV $< p_{\mathrm{T}}^{\mathrm{avg}} <$ 110 GeV and $0.2 < |\eta^{\mathrm{probe}}| <$ 0.7 for **a** $R = 0.2$ and **b** $R = 0.6$ jets, shown together with the corresponding fit (solid line). The corresponding particle level (open markers) truth asymmetry and fits (dashed line) are overlaid. The same distributions are shown for 300 GeV $< p_{\mathrm{T}}^{\mathrm{avg}} <$ 400 GeV and $1.3 < |\eta^{\mathrm{probe}}| < 1.8$ for **c** $R = 0.2$ and **d** $R = 0.6$ jets

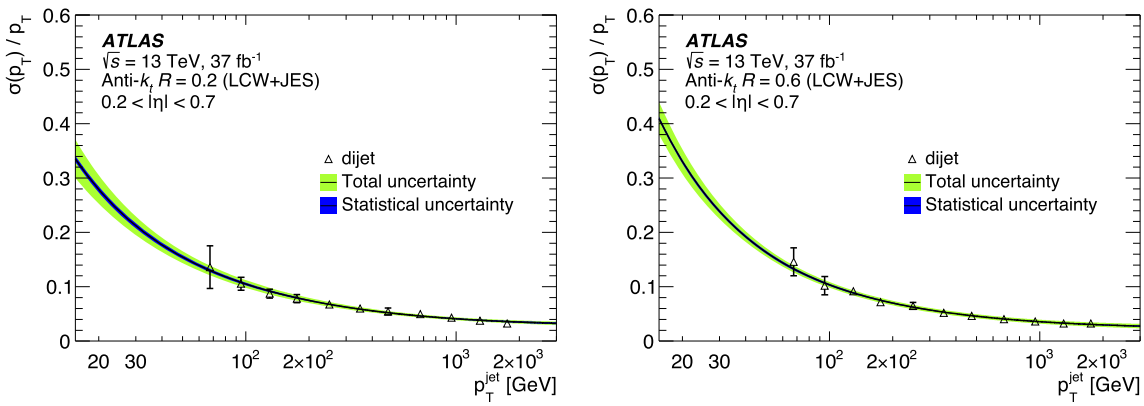

Fig. 20 Relative jet energy resolution as a function of jet p_{T} in the $0.2 < |\eta| < 0.7$ range for **a** $R = 0.2$ and **b** $R = 0.6$ jets, evaluated using the direct balance method. The final fit using the function in Eq. 3 is included along with its associated statistical and total uncertainties. In this fit, the region below jet $p_{\mathrm{T}} < 60$ GeV is constrained by fixing the noise term to the value obtained with the random cones method as described in Sect. 6.1

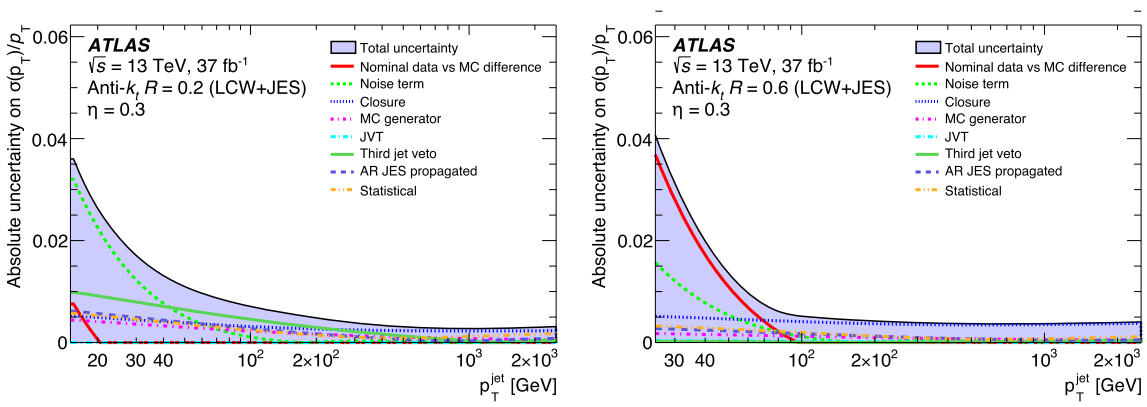

(a) (b)

Fig. 21 Relative uncertainty in the jet energy resolution as a function of jet p_{T} at $\eta = 0.3$ values for **a** $R = 0.2$ and **b** $R = 0.6$ jets. The contributions from the uncertainty sources are shown individually. The total uncertainty, determined as the quadrature sum of all components, is shown as a filled region topped by a solid line. Flavour-dependent components of the JES uncertainties assume a dijet flavour composition

The uncertainties in the noise term estimated in Sect. 6.1 are propagated to the final JER results by fixing N to the maximum and minimum values corresponding to the boundaries of the 68% confidence interval, and re-evaluating the fit to the S and C terms. The relative uncertainties in N grow with $1/p_{\mathrm{T}}$ as expected given the functional parameterisation of JER with Eq. (3), and tend to dominate the JER measurement at low jet transverse momenta $p_{\mathrm{T}} \lesssim 50$ GeV.

The accuracy of the random cone and direct balance methods is limited by the agreement between data and MC simulations. This is checked by comparing the nominal JER results in data to those obtained in MC simulations. Typically, MC simulations result in a smaller resolution, and can be brought into agreement with data by smearing jet momenta. In this case, no systematic uncertainty is assigned. In regions of phase space where MC simulations result in a larger resolution than data, the net difference between nominal data and MC is assigned as a systematic uncertainty, in analogy to Ref. [4].

After the propagation of the individual systematic effects through the S, C fit as described above, a smooth p_{T} dependence is observed for the absolute uncertainties in $\sigma(p_{\mathrm{T}})/p_{\mathrm{T}}$, as demonstrated in Fig. 21. The uncertainties are of similar magnitude for $R = 0.2$ and $R = 0.6$ jets. The noise term uncertainty dominates for $R = 0.2$ jets, which can be understood considering their smaller catchment area compared with $R = 0.6$ jets, resulting in larger fluctuations in $\sigma(p_{\mathrm{T}})/p_{\mathrm{T}}$ for $p_{\mathrm{T}} \lesssim 50$ GeV due to noise. This effect is more pronounced in the transition region between the barrel and forward calorimeters, and at $|\eta| \gtrsim 2$. The nominal data vs MC difference is the dominant systematic uncertainty below $p_{\mathrm{T}} \lesssim 100$ GeV for $R = 0.6$ jets, and is significantly larger than for $R = 0.2$ jets. This is attributed to challenges in modelling low-energetic contributions like pile-up for jets with a large catchment area, where they can account for a sizeable fraction of the total jet energy at $p_{\mathrm{T}} \lesssim 100$ GeV.

The absolute uncertainties in $\sigma(p_{\mathrm{T}})/p_{\mathrm{T}}$ as a function of η are shown in Fig. 22. Upward and downward shifts of systematic uncertainties are found to induce variations of very similar amplitude in the relative JER fit. Generally, the uncertainties tend to grow with $|\eta|$, in particular the dominant uncertainties in the noise term and in the nominal data vs MC difference discussed above. Another uncertainty that can be sizeable at $|\eta| \gtrsim 2$ is from the choice of the MC generator. The uncertainty is highest in $2.5 \leq |\eta| \leq 3$ for $R = 0.2$ jets due to the noise term, and can be as large as 5%. This effect is significantly less pronounced for $R = 0.6$ jets due to averaging over their larger catchment area.

6.3.1 *Uncertainty correlations and reductions*

Two JER uncertainties are treated as correlated with the corresponding JES uncertainties: the dijet modelling uncertainty in MC simulation is derived from the comparison of the nominal MC generator `PYTHIA8` with the alternative generator `SHERPA`; and the JVT uncertainty that is estimated by using the same procedure for JER and JES. All other sources of uncertainty are treated as uncorrelated.

The systematic uncertainties in the JER amount to a total of 101 (102) components for $R = 0.2$ ($R = 0.6$) jets, where each source of uncertainty is represented by a nuisance parameter. The correlations between JERs for pairwise combination of jets in the central range of $|\eta| < 0.2$ are shown as a function of p_{T} in Fig. 23a and b for $R = 0.2$ and $R = 0.6$ jets, respectively. The correlations are maximal for jets with similar p_{T}, as expected. Similarly to the JES, a

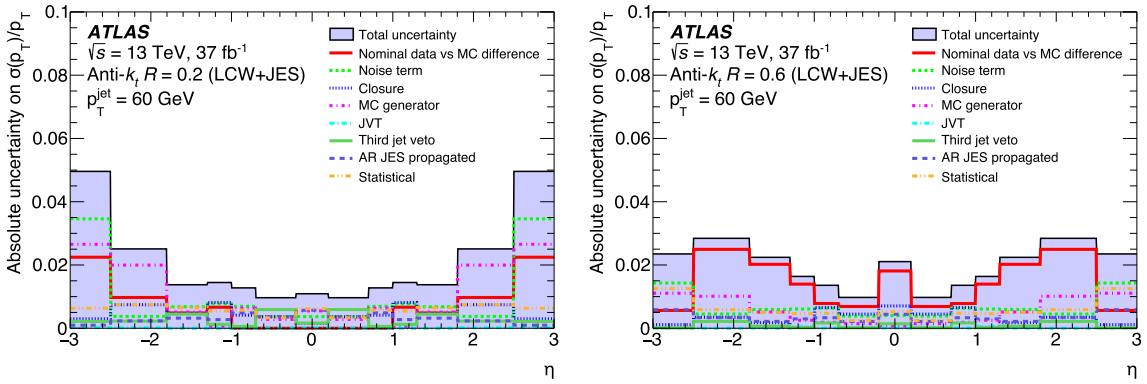

Fig. 22 Relative uncertainty in the jet energy resolution as a function of jet η at $p_{\mathrm{T}} = 60$ GeV for **a** $R = 0.2$ and **b** $R = 0.6$ jets. The contributions from the uncertainty sources are shown individually. The total uncertainty, determined as the quadrature sum of all components, is shown as a filled region topped by a solid line. Flavour-dependent components of the JES uncertainties assume a dijet flavour composition

reduction in the number of JER components is performed to make the data analysis tractable. This is done following the same procedure of an eigenvector decomposition of the total covariance matrix, accounting for dependencies on both p_{T} and $|\eta|$. Technically, this is done using 200 logarithmic p_{T} bins for each of the seven $|\eta|$ ranges considered. The uncertainty accounting for the disagreement between MC and data is not considered in the reduction of the number of uncertainty terms.

The first reduction scheme targets a maximum correlation loss of 5%. By retaining 16 uncertainty terms plus the rest term, a maximum correlation loss of $\lesssim 0.01\%$ was achieved, as shown in Fig. 23c for $R = 0.2$ and Fig. 23d for $R = 0.6$ jets. Retaining one uncertainty term fewer would result in a maximum correlation loss of up to 13%. In the second reduction scheme a maximum correlation loss of 30% is targeted, which is achieved by retaining 10 uncertainty terms plus the rest term. Considering the term accounting for the disagreement between MC and data, this results in 18 and 12 uncertainty terms in the first and second reduction scenarios, respectively.

7 Jet energy scale biases due to close-by hadronic activity

One of the main applications for $R = 0.2$ jets is to recluster them into a large-R jet to reconstruct boosted massive objects decaying hadronically into several particles. A prominent example for this is the track assisted reclustering (TAR) algorithm [8,53,54], which uses fully calibrated anti-k_t jets with $R = 0.2$ as inputs. This algorithm reclusters $R = 0.2$ into larger jets with $R = 1.0$ using trimming parameters optimised for ATLAS [18] and associates ID tracks to the $R = 0.2$ subjets of the reclustered jet. The transverse momenta of matched tracks are then rescaled such that the $R = 0.2$ jet p_{T} matches the sum of the p_{T} of the associated tracks. Hence, the TAR algorithm allows the resolution of the substructure within the jet using track information, while preserving the correct energy scale by using $R = 0.2$ jets.

In the dense environment of a hadronically decaying boosted massive particle, individual $R = 0.2$ jets are likely to have one or several other $R = 0.2$ jets close-by, i.e., within $\Delta R \lesssim 0.4$. The presence of close-by hadronic activity constitutes a different topology from the one used to calibrate the energy scale and derive uncertainties for AR jets described earlier. In the following, the impact of close-by hadronic activity on the jet energy scale is studied. In addition, the modelling of these effects in the Monte Carlo simulations is investigated.

The study of close-by effects considers multijet final states, which allows to minimise statistical uncertainties inherent to *in situ* calibration methods in sparsely populated kinematic regions. Potential biases to the JES are evaluated using the momenta of tracks associated with the $R = 0.2$ jets, since these track momenta are independent of the JES calibration and its associated uncertainties. This analysis uses 80.4 fb^{-1} of pp collision data at $\sqrt{s} = 13$ TeV recorded in 2015–2017 using a suite of single jet triggers with p_{T} thresholds ranging from 60 to 420 GeV. At least two $R = 0.4$ jets with $p_{\mathrm{T}} > 100$ GeV are required in the event to ensure that the 60 GeV trigger is fully efficient. At least two $R = 0.2$ jets with the same p_{T} threshold falling into the full acceptance of the inner tracker of $|\eta| < 2.1$ and matched to the $R = 0.4$ jets within $\Delta R \leq 0.2$ are required.

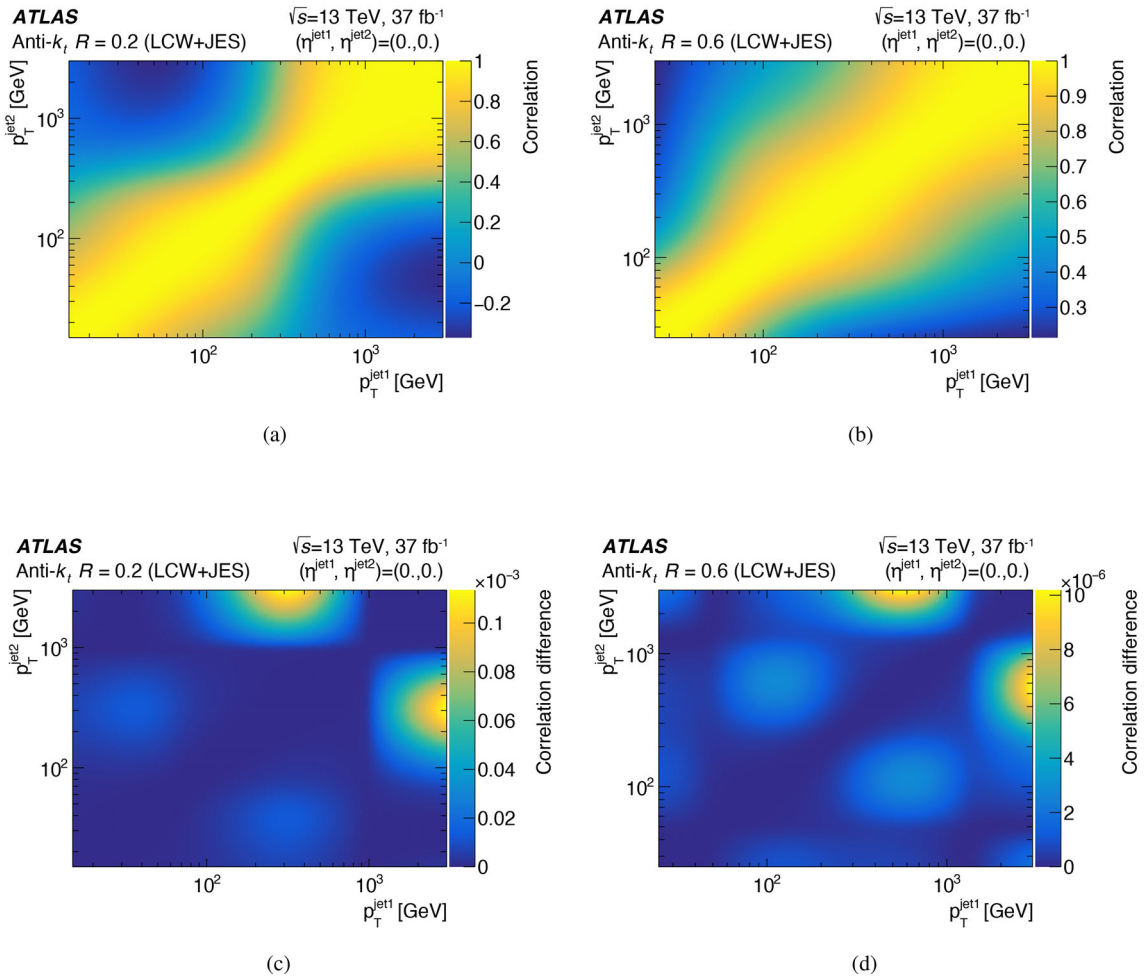

Fig. 23 Correlations of the JER calibration between pairs of **a** $R=0.2$ and **b** $R=0.6$ jets at $\eta=0$ using the full reducible set of 45 p_{T}-dependent *in situ* uncertainty components. Difference between the pair-wise JES correlations (correlation loss) for the full reducible set of uncertainty components and the reduced per category set for **c** $R=0.2$ and **d** $R=0.6$ jets, yielding a maximum correlation difference close to 0.01 for both jet radii

Table 2 Ranges of p_{T} of $R=0.2$ jets used in the study of close-by hadronic activity

$100\,\mathrm{GeV} \leq p_{\mathrm{T}} \leq 250\,\mathrm{GeV}$
$250\,\mathrm{GeV} < p_{\mathrm{T}} \leq 600\,\mathrm{GeV}$
$600\,\mathrm{GeV} < p_{\mathrm{T}} \leq 1200\,\mathrm{GeV}$
$1200\,\mathrm{GeV} < p_{\mathrm{T}} \leq 2400\,\mathrm{GeV}$

Track-jets are clustered from inner detector tracks associated with the primary vertex using the anti-k_t algorithm with $R=0.2$ and are required to have $p_{\mathrm{T}} \geq 15\,\mathrm{GeV}$. The two leading $R=0.2$ jets are selected as "probe $R=0.2$ jets". Each probe $R=0.2$ jet is required to be matched to a track jet within $\Delta R \leq 0.2$. In addition to probe $R=0.2$ jets, "other $R=0.2$ jets" are selected if they exceed $p_{\mathrm{T}} > 20$ GeV. All systematic uncertainties in the JES, as discussed in Sect. 5.3, are considered. The studies are carried out in four bins of $R=0.2$ jet p_{T} as shown in Table 2 with boundaries optimised to capture the physics effects as a function of jet p_{T} while providing a sufficiently small statistical uncertainty.

The main observable of the close-by activity analysis is the inverse charged fraction

$$r_{\mathrm{trk}} = \frac{p_{\mathrm{T}}^{\mathrm{probe}}}{p_{\mathrm{T}}^{\mathrm{trk}}}, \tag{6}$$

where the numerator is the p_{T} of a calibrated probe $R=0.2$ jet, and the denominator the p_{T} of a matched track $R=0.2$ jet. The distribution of r_{trk} is shown in Fig. 24 for two representative p_{T} ranges. The distribution peaks around a value of 1.5, with a pronounced tail to higher r_{trk} values. This observation can be understood considering that only electrically charged particles are registered by tracking detectors and contribute to $p_{\mathrm{T}}^{\mathrm{trk}}$, while both charged and neutral parti-

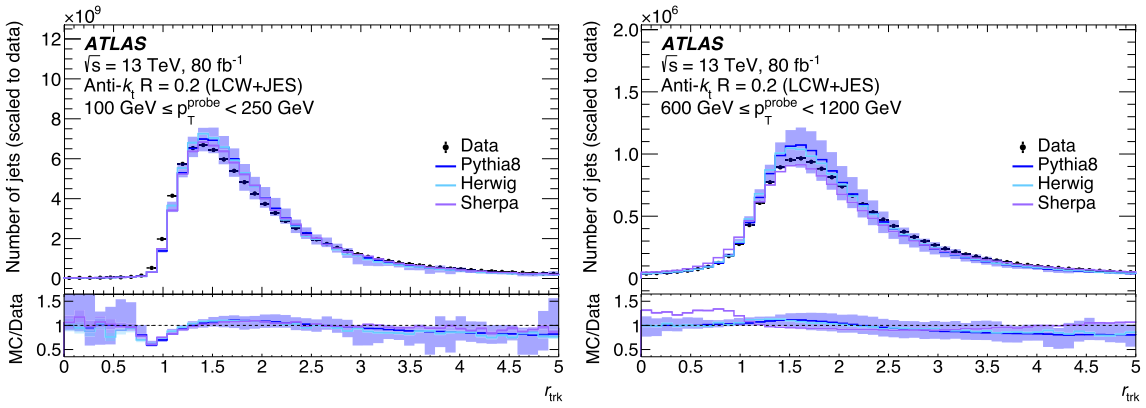

Fig. 24 Distribution of the inverse charged fraction r_{trk} for **a** $100\,\text{GeV} \leq p_{\text{T}}^{\text{probe}} < 250\,\text{GeV}$ and **b** $600\,\text{GeV} \leq p_{\text{T}}^{\text{probe}} < 1200\,\text{GeV}$. The filled band around the PYTHIA8 curve represents the systematic uncertainty due to the JES and the finite number of MC events. The ratio of MC simulation to data for all generators is shown in the bottom panel

cles will contribute to $p_{\text{T}}^{\text{probe}}$. Generally, the r_{trk} distribution is described well by the three MC simulations (PYTHIA8, HERWIG , and SHERPA) within uncertainties, except for the sparsely populated region at $r_{\text{trk}} \lesssim 1$ where some disagreement is observed. This region corresponds to jets where charged particles carry almost all of the jet energy, which are challenging to model in MC simulations especially considering that MC simulations have a smaller JER than data. All MC simulations tend to predict a slightly narrower r_{trk} distribution with a slightly higher mean than the one found in data. An alternative definition of r_{trk} using ghost-associated tracks was tested and found to yield consistent results.

The proximity of hadronic activity is measured using two further observables. One of them is the angular distance of a given probe $R = 0.2$ jet to the closest other $R = 0.2$ jet (ΔR_{min}). The ΔR_{min} distribution is shown in Fig. 25 for two representative p_{T} ranges. The distribution shows a distinct peak around $\Delta R_{\text{min}} \sim 0.25$ and exponentially decreases as a function of ΔR_{min}, as expected from gluon radiation and gluon splitting QCD processes. From the maximum at $\Delta R_{\text{min}} \sim 0.25$, the distribution rapidly drops with decreasing ΔR_{min} values due to the merging of close-by hadronic activity into a single $R = 0.2$ jet. The ΔR_{min} distribution is well modelled in MC simulations, except for HERWIG , which, with the settings described in Sect. 3, has a wider distribution than the data, especially at high p_{T}.

The other observable sensitive to the close-by hadronic activity for a given probe $R = 0.2$ jet is the projected momentum fraction $f_{\text{close-by}}$ of all other $R = 0.2$ jets that are close-by, normalised by its momentum squared. This is given as:

$$f_{\text{close-by}} = \sum_i \frac{(\vec{p} \cdot \vec{p}_i)}{|\vec{p}|^2}, \tag{7}$$

where the index i runs over all other $R = 0.2$ jets within $\Delta R = 0.6$. The distribution of $f_{\text{close-by}}$ is shown in Fig. 26 for the same two representative p_{T} ranges. The distribution displays an exponential decrease as a function of $f_{\text{close-by}}$ for $f_{\text{close-by}} \lesssim 1$, which again can be understood considering the $q \to qg$ and other QCD splitting functions. The rate of the drop increases dramatically for $f_{\text{close-by}} \gtrsim 1$ due to kinematic phase space constraints. Also this distribution is well modelled in MC simulations, except for the HERWIG set-up, which generally predicts smaller values of $f_{\text{close-by}}$ than are observed.

In the following, the inverse charged fraction r_{trk} is studied as a function of the ΔR_{min} and $f_{\text{close-by}}$ observables sensitive to the proximity of hadronic activity. For this, r_{trk} is independently averaged in bins of ΔR_{min} and $f_{\text{close-by}}$, respectively. The averages are constructed per given p_{T} range as defined in Table 2.

The average inverse charged fraction $\langle r_{\text{trk}} \rangle$ as a function of ΔR_{min} is shown for two representative p_{T} ranges in Fig. 27. The distribution of $\langle r_{\text{trk}} \rangle$ is generally fairly constant, and displays a slight decrease towards smaller $\Delta R_{\text{min}} \lesssim 0.5$ for probe $R = 0.2$ jets with $p_{\text{T}} > 250$ GeV. This decrease is more pronounced for probe $R = 0.2$ jets with greater p_{T}, as it becomes more likely for a probe $R = 0.2$ jet to radiate off an energetic parton that would fulfil the selection criteria for other $R = 0.2$ jets. This confirms the presence of an effect on the JES from close-by hadronic activity. The simulations display a constant offset relative to the data. This offset increases with p_{T} from being consistent with unity for $100\,\text{GeV} \leq p_{\text{T}}^{\text{probe}} < 250\,\text{GeV}$ to values as low as 0.9 for $1200\,\text{GeV} \leq p_{\text{T}}^{\text{probe}} < 2400\,\text{GeV}$. This offset is due to the mismodelling of the width of the r_{trk} peak, which shifts $\langle r_{\text{trk}} \rangle$ due to the asymmetry of the r_{trk} distribution around the

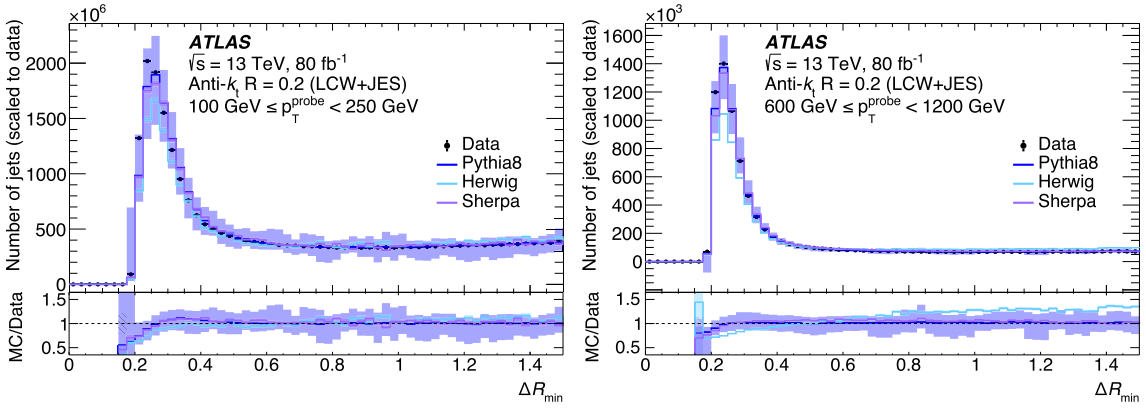

(a) (b)

Fig. 25 Distribution of the angular distance ΔR_{min} from the leading probe to the closest other jet with a $p_{\text{T}} > 20$ GeV for **a** $100\,\text{GeV} \leq p_{\text{T}}^{\text{probe}} < 250\,\text{GeV}$ and **b** $600\,\text{GeV} \leq p_{\text{T}}^{\text{probe}} < 1200\,\text{GeV}$. The filled band around the PYTHIA8 curve represents the systematic uncertainty due to the JES and the finite number of MC events. The ratio of MC simulation to data for all generators is shown in the bottom panel

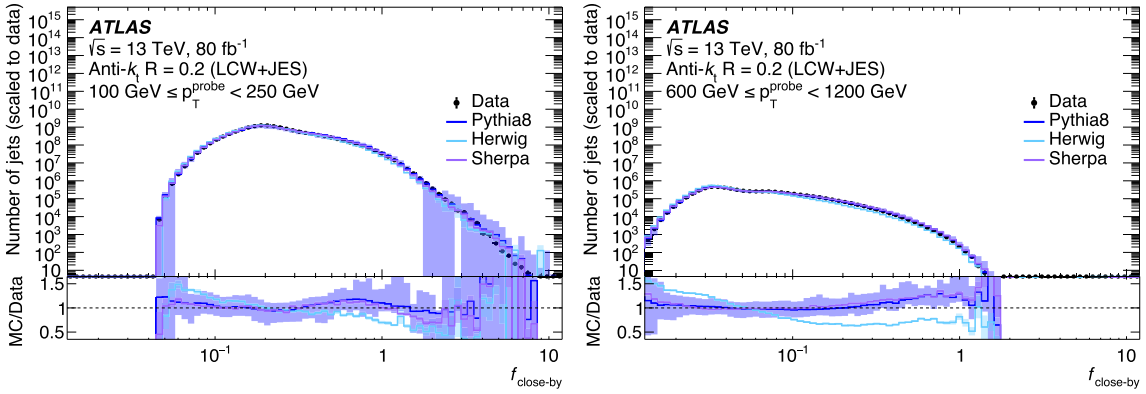

(a) (b)

Fig. 26 Distribution of $f_{\text{close-by}}$ for **a** $100\,\text{GeV} \leq p_{\text{T}}^{\text{probe}} < 250\,\text{GeV}$ and **b** $600\,\text{GeV} \leq p_{\text{T}}^{\text{probe}} < 1200\,\text{GeV}$. The filled band around the PYTHIA8 curve represents the systematic uncertainty due to the JES and the finite number of MC events. The ratio of MC simulation to data for all generators is shown in the bottom panel

mode. As a consequence, PYTHIA8 and HERWIG predict too low an $\langle r_{\text{trk}} \rangle$ because they predict a peak that is too narrow for the r_{trk} distribution compared with data. Conversely, SHERPA predicts a wider r_{trk} spread than observed in data, and an $\langle r_{\text{trk}} \rangle$ higher than in data. However, it is worth pointing out that, despite their overall offset, all studied MC generators describe the decrease in $\langle r_{\text{trk}} \rangle$ with decreasing ΔR_{min} in data well.

The behaviour of the $\langle r_{\text{trk}} \rangle$ is also studied as a function of $f_{\text{close-by}}$, as shown in Fig. 28 for two representative p_{T} bins. The observed trends are similar to the ones reported above as a function of ΔR_{min}: $\langle r_{\text{trk}} \rangle$ decreases as a function of $f_{\text{close-by}}$, i.e., with close-by hadronic activity. The MC generators display again an overall offset, but describe the general trends in $\langle r_{\text{trk}} \rangle$ as a function of $f_{\text{close-by}}$ well. Overall, it is more difficult to draw solid conclusions from $f_{\text{close-by}}$ due to the larger statistical uncertainties in sparsely populated regions of $f_{\text{close-by}} \lesssim 0.1$ and $f_{\text{close-by}} \gtrsim 1$, which are driven by the variations in the $f_{\text{close-by}}$ distributions over eight orders of magnitude.

It can be concluded that the observations in data confirm an effect due to close-by hadronic activity, and that this effect is well modelled in the MC simulations considered. To study the effect further, it is desirable to look beyond $\langle r_{\text{trk}} \rangle$ values determined over the entire sample. This is addressed by carrying out the studies below where $\langle r_{\text{trk}} \rangle$ is determined for parts of the sample that correspond to densely or sparsely populated kinematic regions and varying relative contributions from close-by effects. To this end, the triple ratio is

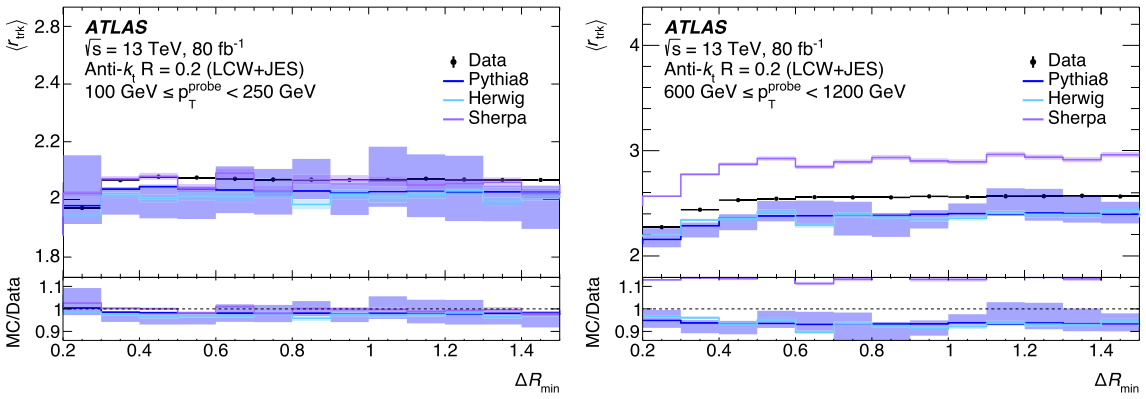

(a) (b)

Fig. 27 Average inverse charged fraction $\langle r_{\text{trk}} \rangle$ as a function of ΔR_{min} for **a** $100\,\text{GeV} \leq p_{\text{T}}^{\text{probe}} < 250\,\text{GeV}$ and **b** $600\,\text{GeV} \leq p_{\text{T}}^{\text{probe}} < 1200\,\text{GeV}$. The filled band around the PYTHIA8 curve represents the systematic uncertainty due to the JES and the finite number of MC events. The ratio of MC simulation to data for all generators is shown in the bottom panel

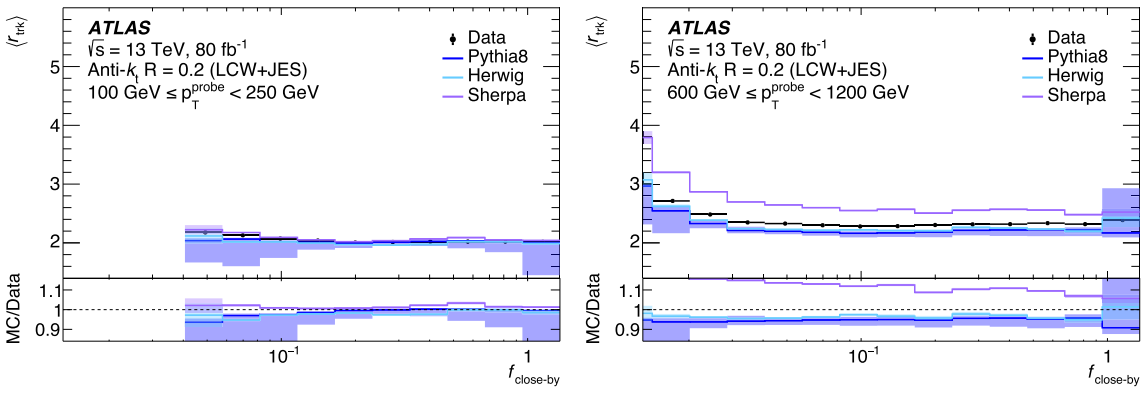

(a) (b)

Fig. 28 Average inverse charged fraction $\langle r_{\text{trk}} \rangle$ as a function of $f_{\text{close-by}}$ for **a** $100\,\text{GeV} \leq p_{\text{T}}^{\text{probe}} < 250\,\text{GeV}$ and **b** $600\,\text{GeV} \leq p_{\text{T}}^{\text{probe}} < 1200\,\text{GeV}$. The filled band around the PYTHIA8 curve represents the systematic uncertainty due to the JES and the finite number of MC events. The ratio of MC simulation to data for all generators is shown in the bottom panel

used

$$\mathcal{T} \equiv \frac{\left(\frac{\langle r_{\text{trk}} \rangle_{\text{high}}}{\langle r_{\text{trk}} \rangle_{\text{low}}}\right)_{\text{Data}}}{\left(\frac{\langle r_{\text{trk}} \rangle_{\text{high}}}{\langle r_{\text{trk}} \rangle_{\text{low}}}\right)_{\text{MC}}}, \tag{8}$$

where $\langle r_{\text{trk}} \rangle_{\text{high}}$ is determined in the quantile of data above a given threshold in ΔR_{min} or $f_{\text{close-by}}$, and conversely $\langle r_{\text{trk}} \rangle_{\text{low}}$ in the quantile below. To probe for any potential deviations, the quantiles are defined as the lower quartile, the median, and the upper quartile of the distribution of the cut variable in the given bin of probe jet p_{T}, as shown in Figs. 25 and 26 for ΔR_{min} and $f_{\text{close-by}}$, respectively. Furthermore, the quantiles corresponding to $\Delta R_{\text{min}} = 0.3, 0.4$, and 0.6 that correspond to 1.5, two, and three jet radii are considered.

The triple ratio $\mathcal{T}_{\Delta R_{\text{min}}}$ for ΔR_{min} is shown in Fig. 29 for two representative p_{T} bins. Overall, the $\mathcal{T}_{\Delta R_{\text{min}}}$ values are found to be consistent with unity within uncertainties, for all quantiles considered. The best description of data is provided by PYTHIA8. The values of $\mathcal{T}_{\Delta R_{\text{min}}}$ for HERWIG and SHERPA have an overall offset that is approximately constant across the quantiles. This offset is consistent with the observations above. The triple ratio $\mathcal{T}_{f_{\text{close-by}}}$ for $f_{\text{close-by}}$ is shown in Fig. 30 for two representative p_{T} bins. Also here the simulations are found to agree with data within uncertainties for all quantiles that were studied. This confirms the absence of any mismodelling of the effect of close-by hadronic radiation on the transverse momentum of calibrated $R = 0.2$ anti-k_t jets. Hence, no additional corrections or calibrations to account for such close-by effects are necessary when reclustering small-R jets into large-R jets. The large kinematic reach of the analysis from 100 GeV up to 2.4 TeV in p_{T} allows

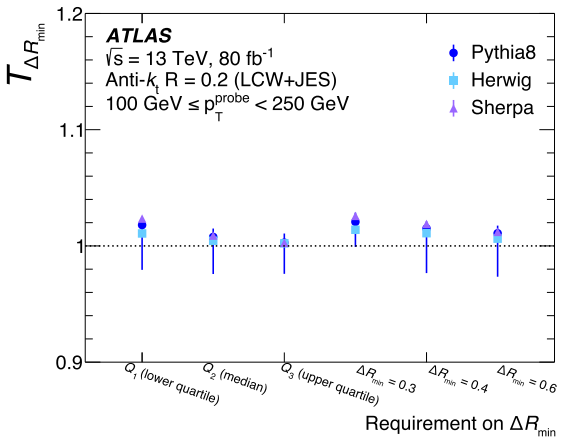

(a)

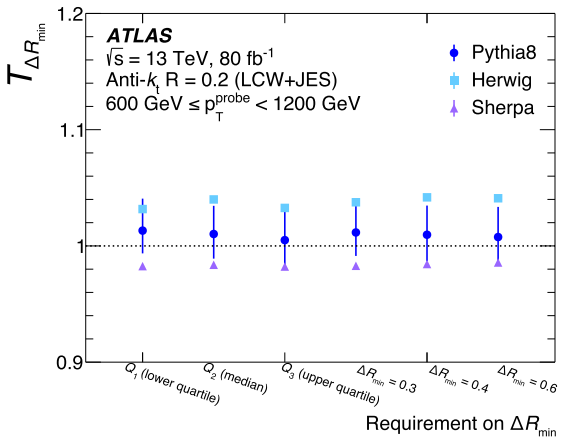

(b)

Fig. 29 Triple ratios $\mathcal{T}_{\Delta R_{\text{min}}}$, defined in Eq. 8, in various regions of ΔR_{min} for **a** $100\,\text{GeV} \leq p_{\text{T}}^{\text{probe}} < 250\,\text{GeV}$ and **b** $600\,\text{GeV} \leq p_{\text{T}}^{\text{probe}} < 1200\,\text{GeV}$. The systematic uncertainty due to the JES and the finite number of MC events is indicated by the vertical bars crossing the PYTHIA8 points. The error bars in the lowest p_{T} bin are asymmetric due to acceptance effects from the requirement of a lower p_{T} threshold. The statistical uncertainty in the HERWIG and SHERPA ratios is shown but is too small to be visible

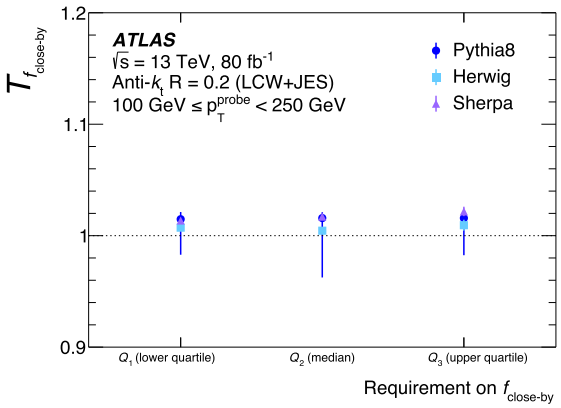

(a)

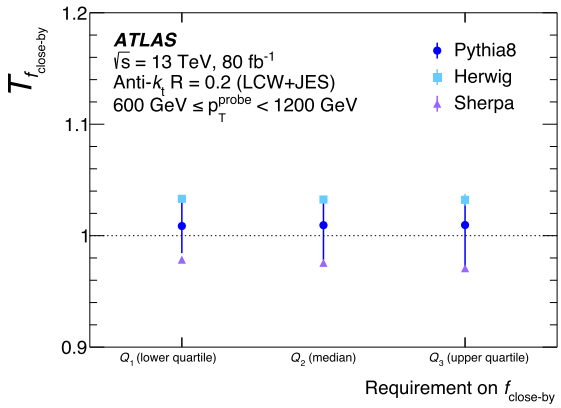

(b)

Fig. 30 Triple ratios $\mathcal{T}_{f_{\text{close-by}}}$, defined in Eq. 8, in various regions of $f_{\text{close-by}}$ for **a** $100\,\text{GeV} \leq p_{\text{T}}^{\text{probe}} < 250\,\text{GeV}$ and **b** $600\,\text{GeV} \leq p_{\text{T}}^{\text{probe}} < 1200\,\text{GeV}$. The systematic uncertainty due to the JES and the finite number of MC events is indicated by the vertical bars crossing the PYTHIA8 points. The error bars in the lowest p_{T} bin are asymmetric due to acceptance effects from the requirement of a lower p_{T} threshold. The statistical uncertainty in the HERWIG and SHERPA ratios is shown but is too small to be visible

to extend this statement to moderately and highly boosted topologies.

The statistical uncertainty in the HERWIG and SHERPA ratios is shown but is too small to be visible.

8 Conclusions

In conclusion, this document presents the measurement of the jet energy scale for jets reconstructed from energy deposits forming topologically connected, locally weighted, clusters of calorimeter cells using the anti-k_t algorithm with $R = 0.2$ and 0.6, referred to as AR jets.

The jet energy scale of AR jets is measured with the ATLAS detector in pp collisions at $\sqrt{s} = 13$ TeV, corresponding to an integrated luminosity of $37\,\text{fb}^{-1}$ collected during 2015 and 2016 at the LHC. These results can be used for calibrating pp collision data recorded in the entire Run 2 of the LHC between 2015 and 2018. AR jets are calibrated with a series of Monte Carlo simulation-based corrections similar to those employed to standard $R = 0.4$ jets, and *in situ* techniques in data. A new *in situ* method to measure differences between data and Monte Carlo simulation is presented.

This direct matching method, compares the p_{T} of AR jets against fully calibrated $R = 0.4$ jets, as a function of η and p_{T}. Consequently, the current method of statistically combining calibration results in multijet and Z+jets topologies as a function of p_{T} is extended to consider the dependence on η for the first time. These techniques were found to be robust and can therefore be used for deriving similar calibrations in the future, or for validating alternative methods like calibrations using single particle responses. The systematic uncertainties associated with the jet energy scale calibration of AR jets are reported. These comprise the uncertainties from the $R = 0.4$ jets used as a reference, uncertainties from the direct matching *in situ* method, and additional uncertainty sources specifically pertaining to $R = 0.2$ and 0.6 AR jets. A fractional uncertainty of around 1% on the JES is achieved in the kinematic range of $100 \lesssim p_{\mathrm{T}} \lesssim 800$ GeV for both $R = 0.2$ and 0.6 jets. Below this p_{T} range, the uncertainties are dominated by the absolute *in situ* JES uncertainty for reference $R = 0.4$ jets and the unknown flavour composition that can respectively reach 4% and 3% around $p_{\mathrm{T}} \simeq 20$ GeV. In addition, the pile-up uncertainty contributes up to 7% for $R = 0.6$ jets. The total uncertainty for AR jets is of similar magnitude to that of reference jets, which demonstrates the power of the direct matching method.

The jet energy resolution for $R = 0.2$ and 0.6 AR jets calibrated following the procedure of this document is then determined. First, the noise term that drives the jet energy resolution at low $p_{\mathrm{T}} \lesssim 50$ GeV is determined using the random cones method. The uncertainty in this term is dominant in the low p_{T} range for $R = 0.2$ jets and contributes an absolute uncertainty in $\sigma(p_{\mathrm{T}})/p_{\mathrm{T}}$ of up to 4% for $p_{\mathrm{T}} \simeq 20$ GeV. For $R = 0.6$ jets, this uncertainty reaches up to 2%. The full JER is then determined using the direct balance method, where the resolutions are extracted by comparing asymmetries in energies of AR jets measured in data to those found in truth jet simulations, in the Z+jets and dijet topologies. The uncertainty from the JES calibration of reference $R = 0.4$ jets contributes about 0.5% to the absolute uncertainty in $\sigma(p_{\mathrm{T}})/p_{\mathrm{T}}$ and is approximately constant in p_{T} and η. At low $p_{\mathrm{T}} \lesssim 70$ GeV, the uncertainty in the nominal data vs MC difference that is driven by the modelling of pile-up is dominant for $R = 0.6$ AR jets and contributes an absolute uncertainty in $\sigma(p_{\mathrm{T}})/p_{\mathrm{T}}$ of up to 4% for $p_{\mathrm{T}} \simeq 20$ GeV. The energy resolution ranges from $(35 \pm 6)\%$ at $p_{\mathrm{T}} = 20$ GeV to $(4 \pm 0.5)\%$ at $p_{\mathrm{T}} = 300$ GeV for central $R = 0.2$ jets, and is found to be slightly higher at $p_{\mathrm{T}} \lesssim 50$ GeV for $R = 0.6$ jets. Overall, the JER for AR jets is comparable to that of $R = 0.4$ reference jets.

Finally, the effect of close-by hadronic activity on the jet energy scale is investigated. This effect is quantified by inspecting the inverse charged fraction of $R = 0.2$ jets as a function of variables sensitive to close-by hadronic activity, and is found to be well modelled in Monte Carlo simulations. These findings confirm that the JES uncertainties presented here adequately account for close-by effects even in experimentally challenging boosted topologies from decays of energetic W, Z, and Higgs bosons and top quarks, studied through reclustering small-R jets into large-R jets.

Acknowledgements We thank CERN for the very successful operation of the LHC and its injectors, as well as the support staff at CERN and at our institutions worldwide without whom ATLAS could not be operated efficiently. The crucial computing support from all WLCG partners is acknowledged gratefully, in particular from CERN, the ATLAS Tier-1 facilities at TRIUMF/SFU (Canada), NDGF (Denmark, Norway, Sweden), CC-IN2P3 (France), KIT/GridKA (Germany), INFN-CNAF (Italy), NL-T1 (Netherlands), PIC (Spain), RAL (UK) and BNL (USA), the Tier-2 facilities worldwide and large non-WLCG resource providers. Major contributors of computing resources are listed in Ref. [55]. We gratefully acknowledge the support of ANPCyT, Argentina; YerPhI, Armenia; ARC, Australia; BMWFW and FWF, Austria; ANAS, Azerbaijan; CNPq and FAPESP, Brazil; NSERC, NRC and CFI, Canada; CERN; ANID, Chile; CAS, MOST and NSFC, China; Minciencias, Colombia; MEYS CR, Czech Republic; DNRF and DNSRC, Denmark; IN2P3-CNRS and CEA-DRF/IRFU, France; SRNSFG, Georgia; BMBF, HGF and MPG, Germany; GSRI, Greece; RGC and Hong Kong SAR, China; ICHEP and Academy of Sciences and Humanities, Israel; INFN, Italy; MEXT and JSPS, Japan; CNRST, Morocco; NWO, Netherlands; RCN, Norway; MNiSW, Poland; FCT, Portugal; MNE/IFA, Romania; MSTDI, Serbia; MSSR, Slovakia; ARIS and MVZI, Slovenia; DSI/NRF, South Africa; MICIU/AEI, Spain; SRC and Wallenberg Foundation, Sweden; SERI, SNSF and Cantons of Bern and Geneva, Switzerland; NSTC, Taipei; TENMAK, Türkiye; STFC/UKRI, United Kingdom; DOE and NSF, United States of America. Individual groups and members have received support from BCKDF, CANARIE, CRC and DRAC, Canada; CERN-CZ, FORTE and PRIMUS, Czech Republic; COST, ERC, ERDF, Horizon 2020, ICSC-NextGenerationEU and Marie Skłodowska-Curie Actions, European Union; Investissements d'Avenir Labex, Investissements d'Avenir Idex and ANR, France; DFG and AvH Foundation, Germany; Herakleitos, Thales and Aristeia programmes co-financed by EU-ESF and the Greek NSRF, Greece; BSF-NSF and MINERVA, Israel; NCN and NAWA, Poland; La Caixa Banking Foundation, CERCA Programme Generalitat de Catalunya and PROMETEO and GenT Programmes Generalitat Valenciana, Spain; Göran Gustafssons Stiftelse, Sweden; The Royal Society and Leverhulme Trust, United Kingdom. In addition, individual members wish to acknowledge support from Armenia: Yerevan Physics Institute (FAPERJ); CERN: European Organization for Nuclear Research (CERN DOCT); Chile: Agencia Nacional de Investigación y Desarrollo (FONDECYT 1230812, FONDECYT 1230987, FONDECYT 1240864); China: Chinese Ministry of Science and Technology (MOST-2023YFA1605700, MOST-2023YFA1609300), National Natural Science Foundation of China (NSFC - 12175119, NSFC 12275265, NSFC-12075060); Czech Republic: Czech Science Foundation (GACR - 24-11373S), Ministry of Education Youth and Sports (FORTE CZ.02.01.01/00/22_008/0004632), PRIMUS Research Programme (PRIMUS/21/SCI/017); EU: H2020 European Research Council (ERC - 101002463); European Union: European Research Council (ERC - 948254, ERC 101089007, ERC, BARD, 101116429), European Union, Future Artificial Intelligence Research (FAIR-NextGenerationEU PE00000013), Italian Center for High Performance Computing, Big Data and Quantum Computing (ICSC, NextGenerationEU); France: Agence Nationale de la Recherche (ANR-20-CE31-0013, ANR-21-CE31-0013, ANR-21-CE31-0022, ANR-22-EDIR-0002); Germany: Baden-Württemberg Stiftung (BW Stiftung-Postdoc Eliteprogramme), Deutsche Forschungsgemeinschaft (DFG - 469666862, DFG - CR 312/5-2); Italy: Istituto Nazionale di

Fisica Nucleare (ICSC, NextGenerationEU), Ministero dell'Università e della Ricerca (PRIN - 20223N7F8K - PNRR M4.C2.1.1); Japan: Japan Society for the Promotion of Science (JSPS KAKENHI JP22H01227, JSPS KAKENHI JP22H04944, JSPS KAKENHI JP22KK0227, JSPS KAKENHI JP23KK0245); Norway: Research Council of Norway (RCN-314472); Poland: Ministry of Science and Higher Education (IDUB AGH, POB8, D4 no 9722), Polish National Agency for Academic Exchange (PPN/PPO/2020/1/00002/U/00001), Polish National Science Centre (NCN 2021/42/E/ST2/00350, NCN OPUS 2023/51/B/ST2/02507, NCN OPUS nr 2022/47/B/ST2/03059, NCN UMO-2019/34/E/ST2/00393, NCN & H2020 MSCA 945339, UMO-2020/37/B/ST2/01043, UMO-2021/40/C/ST2/00187, UMO-2022/47/O/ST2/00148, UMO-2023/49/B/ST2/04085, UMO-2023/51/B/ST2/00920); Spain: Generalitat Valenciana (Artemisa, FEDER, IDIFEDER/2018/048), Ministry of Science and Innovation (MCIN & NextGenEU PCI2022-135018-2, MICIN & FEDER PID2021-125273NB, RYC2019-028510-I, RYC2020-030254-I, RYC2021-031273-I, RYC2022-038164-I); Sweden: Carl Trygger Foundation (Carl Trygger Foundation CTS 22:2312), Swedish Research Council (Swedish Research Council 2023-04654, VR 2018-00482, VR 2022-03845, VR 2022-04683, VR 2023-03403, VR grant 2021-03651), Knut and Alice Wallenberg Foundation (KAW 2018.0458, KAW 2019.0447, KAW 2022.0358); Switzerland: Swiss National Science Foundation (SNSF - PCEFP2_194658); United Kingdom: Leverhulme Trust (Leverhulme Trust RPG-2020-004), Royal Society (NIF-R1-231091); United States of America: U.S. Department of Energy (ECA DE-AC02-76SF00515), Neubauer Family Foundation.

Data Availability Statement This manuscript has no associated data. [Author's' comment: Data sharing not applicable to this article as no datasets were generated or analysed during the current study.]

Code Availability Statement This manuscript has no associated code/software. [Author's comment: Code/Software sharing not applicable to this article as no code/software was generated or analysed during the current study.]

Funded by SCOAP[3].

References

1. L. Evans, P. Bryant, L.H.C. Machine, J. Instrum. **3**, S08001 (2008)
2. M. Cacciari, G.P. Salam, G. Soyez, The anti-k_t jet clustering algorithm. JHEP **04**, 063 (2008). https://doi.org/10.1088/1126-6708/2008/04/063. arXiv:0802.1189 [hep-ph]
3. M. Cacciari, G.P. Salam, G. Soyez, FastJet user manual. Eur. Phys. J. C **72**, 1896 (2012). https://doi.org/10.1140/epjc/s10052-012-1896-2. arXiv:1111.6097 [hep-ph]
4. ATLAS Collaboration, Jet energy scale and resolution measured in proton–proton collisions at $\sqrt{s} = 13$ TeV with the ATLAS detector. Eur. Phys. J. C **81**, 689 (2021). https://doi.org/10.1140/epjc/s10052-021-09402-3. arXiv:2007.02645 [hep-ex]
5. ATLAS Collaboration, Jet radius dependence of dijet momentum balance and suppression in Pb+Pb collisions at 5.02 TeV with the ATLAS detector. Phys. Rev. C **110**, 054912 (2024). https://doi.org/10.1103/PhysRevC.110.054912. arXiv:2407.18796 [nucl-ex]
6. ATLAS Collaboration, Luminosity determination in pp collisions at $\sqrt{s} = 13$ TeV using the ATLAS detector at the LHC. Eur. Phys. J. C **83**, 982 (2023). https://doi.org/10.1140/epjc/s10052-023-11747-w. arXiv:2212.09379 [hep-ex]
7. G. Avoni et al., The new LUCID-2 detector for luminosity measurement and monitoring in ATLAS. JINST **13**, P07017 (2018). https://doi.org/10.1088/1748-0221/13/07/P07017
8. ATLAS Collaboration, Search for dark matter produced in association with a dark Higgs boson decaying into W^+W^- in the one-lepton final state at $\sqrt{s} = 13$ TeV using 139 fb^{-1} of pp collisions recorded with the ATLAS detector. JHEP **07**, 116 (2023). https://doi.org/10.1007/JHEP07(2023)116. arXiv:2211.07175 [hep-ex]
9. ATLAS Collaboration, Search for boosted low-mass resonances decaying into hadrons produced in association with a photon in pp collisions at $\sqrt{s} = 13$ TeV with the ATLAS detector. JHEP 1, 99 (2025). https://doi.org/10.1007/JHEP01(2025)099. arXiv:2408.00049 [hep-ex]
10. ATLAS Collaboration, Jet energy measurement with the ATLAS detector in proton–proton collisions at $\sqrt{s} = 7$ TeV. Eur. Phys. J. C **73**, 2304 (2013). https://doi.org/10.1140/epjc/s10052-013-2304-2. arXiv:1112.6426 [hep-ex]
11. ATLAS Collaboration, Single hadron response measurement and calorimeter jet energy scale uncertainty with the ATLAS detector at the LHC. Eur. Phys. J. C **73**, 2305 (2013). https://doi.org/10.1140/epjc/s10052-013-2305-1. arXiv:1203.1302 [hep-ex]
12. ATLAS Collaboration, Jet energy resolution in proton–proton collisions at $\sqrt{s} = 7$ TeV recorded in 2010 with the ATLAS detector. Eur. Phys. J. C **73**, 2306 (2013). https://doi.org/10.1140/epjc/s10052-013-2306-0. arXiv:1210.6210 [hep-ex]
13. ATLAS Collaboration, Jet energy measurement and its systematic uncertainty in proton–proton collisions at $\sqrt{s} = 7$ TeV with the ATLAS detector. Eur. Phys. J. C **75**, 17 (2015). https://doi.org/10.1140/epjc/s10052-014-3190-y. arXiv:1406.0076 [hep-ex]
14. ATLAS Collaboration, Determination of jet calibration and energy resolution in proton–proton collisions at $\sqrt{s} = 8$ TeV using the ATLAS detector. Eur. Phys. J. C **80**, 1104 (2020). https://doi.org/10.1140/epjc/s10052-020-08477-8. arXiv:1910.04482 [hep-ex]
15. ATLAS Collaboration, Jet energy scale measurements and their systematic uncertainties in proton–proton collisions at $\sqrt{s} = 13$ TeV with the ATLAS detector. Phys. Rev. D **96**, 072002 (2017). https://doi.org/10.1103/PhysRevD.96.072002. arXiv:1703.09665 [hep-ex]
16. ATLAS Collaboration, New techniques for jet calibration with the ATLAS detector. Eur. Phys. J. C **83**, 761 (2023). https://doi.org/10.1140/epjc/s10052-023-11837-9. arXiv:2303.17312 [hep-ex]
17. ATLAS Collaboration, A precise measurement of the jet energy scale derived from single-particle measurements and in situ techniques in proton–proton collisions at $\sqrt{s} = 13$ TeV with the ATLAS detector (2024). arXiv:2407.15627 [hep-ex]
18. ATLAS Collaboration, In situ calibration of large-radius jet energy and mass in 13 TeV proton–proton collisions with the ATLAS detector. Eur. Phys. J. C **79**, 135 (2019). https://doi.org/10.1140/epjc/s10052-019-6632-8. arXiv:1807.09477 [hep-ex]
19. ATLAS Collaboration, Jet reclustering and close-by effects in ATLAS Run 2. ATLAS-CONF-2017-062 (2017). https://cds.cern.ch/record/2275649
20. ATLAS Collaboration, The ATLAS experiment at the CERN large hadron collider. JINST **3**, S08003 (2008). https://doi.org/10.1088/1748-0221/3/08/S08003
21. ATLAS Collaboration, ATLAS insertable B-layer technical design report. ATLAS-TDR-19; CERN-LHCC-2010-013 (2010). https://cds.cern.ch/record/1291633. [Addendum: ATLAS-TDR-

19-ADD-1; CERN-LHCC-2012-009 (2012). https://cds.cern.ch/record/1451888]
22. ATLAS Electromagnetic Liquid Argon Group, Construction, assembly and tests of the ATLAS electromagnetic end-cap calorimeters. JINST **3**, P06002 (2008). https://doi.org/10.1088/1748-0221/3/06/P06002
23. ATLAS Collaboration, ATLAS calorimeter performance: technical design report. ATLAS-TDR-1; CERN-LHCC-96-040 (1996). https://cds.cern.ch/record/331059
24. ATLAS Collaboration, Performance of the ATLAS trigger system in 2015. Eur. Phys. J. C **77**, 317 (2017). https://doi.org/10.1140/epjc/s10052-017-4852-3. arXiv:1611.09661 [hep-ex]
25. ATLAS Collaboration, ATLAS data quality operations and performance for 2015–2018 data-taking. JINST **15**, P04003 (2020). https://doi.org/10.1088/1748-0221/15/04/P04003. arXiv:1911.04632 [physics.ins-det]
26. T. Sjöstrand, S. Mrenna, P. Skands, A brief introduction to PYTHIA 8.1. Comput. Phys. Commun. **178**, 852 (2008). https://doi.org/10.1016/j.cpc.2008.01.036. arXiv:0710.3820 [hep-ph]
27. NNPDF Collaboration, Parton distributions with LHC data. Nucl. Phys. B **867**, 244 (2013). https://doi.org/10.1016/j.nuclphysb.2012.10.003. arXiv:1207.1303 [hep-ph]
28. B. Andersson, G. Gustafson, G. Ingelman, T. Sjöstrand, Parton fragmentation and string dynamics. Phys. Rep. **97**, 31 (1983). https://doi.org/10.1016/0370-1573(83)90080-7
29. ATLAS Collaboration, ATLAS Pythia 8 tunes to 7 TeV data. ATL-PHYS-PUB-2014-021 (2014). https://cds.cern.ch/record/1966419
30. D.J. Lange, The EvtGen particle decay simulation package. Nucl. Instrum. Methods A **462**, 152 (2001). https://doi.org/10.1016/S0168-9002(01)00089-4
31. S. Alioli, P. Nason, C. Oleari, E. Re, A general framework for implementing NLO calculations in shower Monte Carlo programs: the POWHEG BOX. JHEP **06**, 043 (2010). https://doi.org/10.1007/JHEP06(2010)043. arXiv:1002.2581 [hep-ph]
32. H.-L. Lai et al., New parton distributions for collider physics. Phys. Rev. D **82**, 074024 (2010). https://doi.org/10.1103/PhysRevD.82.074024. arXiv:1007.2241 [hep-ph]
33. J. Pumplin et al., New generation of parton distributions with uncertainties from global QCD analysis. JHEP **07**, 012 (2002). https://doi.org/10.1088/1126-6708/2002/07/012. arXiv:hep-ph/0201195
34. ATLAS Collaboration, Example ATLAS tunes of PYTHIA 8, PYTHIA 6 and POWHEG to an observable sensitive to Z boson transverse momentum. ATL-PHYS-PUB-2013-017 (2013). https://cds.cern.ch/record/1629317
35. E. Bothmann et al., Event generation with Sherpa 2.2. SciPost Phys. **7**, 034 (2019). https://doi.org/10.21468/SciPostPhys.7.3.034. arXiv:1905.09127 [hep-ph]
36. S. Catani, F. Krauss, B.R. Webber, R. Kuhn, QCD matrix elements + parton showers. JHEP **11**, 063 (2001). https://doi.org/10.1088/1126-6708/2001/11/063. arXiv:hep-ph/0109231
37. J. Bellm et al., Herwig 7.0/Herwig++ 3.0 release note. Eur. Phys. J. C **76**, 196 (2016). https://doi.org/10.1140/epjc/s10052-016-4018-8. arXiv:1512.01178 [hep-ph]
38. NNPDF Collaboration, Parton distributions for the LHC run II. JHEP **04**, 040 (2015). https://doi.org/10.1007/JHEP04(2015)040. arXiv:1410.8849 [hep-ph]
39. T. Sjöstrand et al., An introduction to PYTHIA 8.2. Comput. Phys. Commun. **191**, 159 (2015). https://doi.org/10.1016/j.cpc.2015.01.024. arXiv:1410.3012 [hep-ph]
40. ATLAS Collaboration, The Pythia 8 A3 tune description of ATLAS minimum bias and inelastic measurements incorporating the Donnachie–Landshoff diffractive model. ATL-PHYS-PUB-2016-017 (2016). https://cds.cern.ch/record/2206965
41. ATLAS Collaboration, The ATLAS simulation infrastructure. Eur. Phys. J. C **70**, 823 (2010). https://doi.org/10.1140/epjc/s10052-010-1429-9. arXiv:1005.4568 [physics.ins-det]
42. S. Agostinelli et al., GEANT4—a simulation toolkit. Nucl. Instrum. Methods A **506**, 250 (2003). https://doi.org/10.1016/S0168-9002(03)01368-8
43. ATLAS Collaboration, Software and computing for Run 3 of the ATLAS experiment at the LHC. Eur. Phys. J. C **85**, 234 (2025). https://doi.org/10.1140/epjc/s10052-024-13701-w arXiv:2404.06335 [hep-ex]
44. ATLAS Collaboration, Topological cell clustering in the ATLAS calorimeters and its performance in LHC Run 1. Eur. Phys. J. C **77**, 490 (2017). https://doi.org/10.1140/epjc/s10052-017-5004-5. arXiv:1603.02934 [hep-ex]
45. ATLAS Collaboration, Vertex reconstruction performance of the ATLAS detector at $\sqrt{s} = 13$ TeV. ATL-PHYS-PUB-2015-026 (2015). https://cds.cern.ch/record/2037717
46. ATLAS Collaboration, A neural network clustering algorithm for the ATLAS silicon pixel detector. JINST **9**, P09009 (2014). https://doi.org/10.1088/1748-0221/9/09/P09009. arXiv:1406.7690 [hep-ex]
47. M. Cacciari, G.P. Salam, Pileup subtraction using jet areas. Phys. Lett. B **659**, 119 (2008). https://doi.org/10.1016/j.physletb.2007.09.077. arXiv:0707.1378 [hep-ph]
48. ATLAS Collaboration, Muon reconstruction and identification efficiency in ATLAS using the full Run 2 pp collision data set at $\sqrt{s} = 13$ TeV. Eur. Phys. J. C **81**, 578 (2021). https://doi.org/10.1140/epjc/s10052-021-09233-2. arXiv:2012.00578 [hep-ex]
49. S.D. Ellis, D.E. Soper, Successive combination jet algorithm for hadron collisions. Phys. Rev. D **48**, 3160 (1993). https://doi.org/10.1103/PhysRevD.48.3160. arXiv:hep-ph/9305266
50. ATLAS Collaboration, Performance of pile-up mitigation techniques for jets in pp collisions at $\sqrt{s} = 8$ TeV using the ATLAS detector. Eur. Phys. J. C **76**, 581 (2016). https://doi.org/10.1140/epjc/s10052-016-4395-z. arXiv:1510.03823 [hep-ex]
51. ATLAS Collaboration, Evaluating statistical uncertainties and correlations using the bootstrap method. ATL-PHYS-PUB-2021-011 (2021). https://cds.cern.ch/record/2759945
52. ATLAS Collaboration, Pile-up subtraction and suppression for jets in ATLAS. ATLAS-CONF-2013-083 (2013). https://cds.cern.ch/record/1570994
53. ATLAS Collaboration, Track assisted techniques for jet substructure. ATL-PHYS-PUB-2018-012 (2018). https://cds.cern.ch/record/2630864
54. ATLAS Collaboration, Search for dark matter produced in association with a dark Higgs boson decaying into W^+W^- or ZZ in fully hadronic final states from $\sqrt{s} = 13$ TeV pp collisions recorded with the ATLAS detector. Phys. Rev. Lett. **126**, 121802 (2021). https://doi.org/10.1103/PhysRevLett.126.121802. arXiv:2010.06548 [hep-ex]
55. ATLAS Collaboration, ATLAS computing acknowledgements. ATL-SOFT-PUB-2023-001 (2023). https://cds.cern.ch/record/2869272

ATLAS Collaboration[★]

G. Aad[105], E. Aakvaag[17], B. Abbott[124], S. Abdelhameed[120a], K. Abeling[56], N. J. Abicht[50], S. H. Abidi[30], M. Aboelela[46], A. Aboulhorma[36e], H. Abramowicz[158], Y. Abulaiti[121], B. S. Acharya[70a,70b,n], A. Ackermann[64a], C. Adam Bourdarios[4], L. Adamczyk[87a], S. V. Addepalli[150], M. J. Addison[104], J. Adelman[119], A. Adiguzel[22c], T. Adye[138], A. A. Affolder[140], Y. Afik[41], M. N. Agaras[13], A. Aggarwal[103], C. Agheorghiesei[28c], F. Ahmadov[40,ac], S. Ahuja[98], X. Ai[144b], G. Aielli[77a,77b], A. Aikot[170], M. Ait Tamlihat[36e], B. Aitbenchikh[36a], M. Akbiyik[103], T. P. A. Åkesson[101], A. V. Akimov[152], D. Akiyama[175], N. N. Akolkar[25], S. Aktas[22a], G. L. Alberghi[24b], J. Albert[172], P. Albicocco[54], G. L. Albouy[61], S. Alderweireldt[53], Z. L. Alegria[125], M. Aleksa[37], I. N. Aleksandrov[40], C. Alexa[28b], T. Alexopoulos[10], F. Alfonsi[24b], M. Algren[57], M. Alhroob[174], B. Ali[136], H. M. J. Ali[94,w], S. Ali[32], S. W. Alibocus[95], M. Aliev[34c], G. Alimonti[72a], W. Alkakhi[56], C. Allaire[67], B. M. M. Allbrooke[153], J. S. Allen[104], J. F. Allen[53], P. P. Allport[21], A. Aloisio[73a,73b], F. Alonso[93], C. Alpigiani[143], Z. M. K. Alsolami[94], A. Alvarez Fernandez[103], M. Alves Cardoso[57], M. G. Alviggi[73a,73b], M. Aly[104], Y. Amaral Coutinho[84b], A. Ambler[107], C. Amelung[37], M. Amerl[104], C. G. Ames[112], D. Amidei[109], B. Amini[55], K. J. Amirie[162], A. Amirkhanov[40], S. P. Amor Dos Santos[134a], K. R. Amos[170], D. Amperiadou[159], S. An[85], V. Ananiev[129], C. Anastopoulos[146], T. Andeen[11], J. K. Anders[95], A. C. Anderson[60], A. Andreazza[72a,72b], S. Angelidakis[9], A. Angerami[43], A. V. Anisenkov[40], A. Annovi[75a], C. Antel[57], E. Antipov[152], M. Antonelli[54], F. Anulli[76a], M. Aoki[85], T. Aoki[160], M. A. Aparo[153], L. Aperio Bella[49], C. Appelt[158], A. Apyan[27], S. J. Arbiol Val[88], C. Arcangeletti[54], A. T. H. Arce[52], J.-F. Arguin[111], S. Argyropoulos[159], J.-H. Arling[49], O. Arnaez[4], H. Arnold[152], G. Artoni[76a,76b], H. Asada[114], K. Asai[122], S. Asai[160], N. A. Asbah[37], R. A. Ashby Pickering[174], A. M. Aslam[98], K. Assamagan[30], R. Astalos[29a], K. S. V. Astrand[101], S. Atashi[166], R. J. Atkin[34a], H. Atmani[36f], P. A. Atmasiddha[132], K. Augsten[136], A. D. Auriol[42], V. A. Austrup[104], G. Avolio[37], K. Axiotis[57], G. Azuelos[111,ag], D. Babal[29b], H. Bachacou[139], K. Bachas[159,r], A. Bachiu[35], E. Bachmann[51], M. J. Backes[64a], A. Badea[41], T. M. Baer[109], P. Bagnaia[76a,76b], M. Bahmani[19], D. Bahner[55], K. Bai[127], J. T. Baines[138], L. Baines[97], O. K. Baker[179], E. Bakos[16], D. Bakshi Gupta[8], L. E. Balabram Filho[84b], V. Balakrishnan[124], R. Balasubramanian[4], E. M. Baldin[38], P. Balek[87a], E. Ballabene[24a,24b], F. Balli[139], L. M. Baltes[64a], W. K. Balunas[33], J. Balz[103], I. Bamwidhi[120b], E. Banas[88], M. Bandieramonte[133], A. Bandyopadhyay[25], S. Bansal[25], L. Barak[158], M. Barakat[49], E. L. Barberio[108], D. Barberis[58a,58b], M. Barbero[105], M. Z. Barel[118], T. Barillari[113], M.-S. Barisits[37], T. Barklow[150], P. Baron[126], D. A. Baron Moreno[104], A. Baroncelli[63], A. J. Barr[130], J. D. Barr[99], F. Barreiro[102], J. Barreiro Guimarães da Costa[14], M. G. Barros Teixeira[134a], S. Barsov[38], F. Bartels[64a], R. Bartoldus[150], A. E. Barton[94], P. Bartos[29a], A. Basan[103], M. Baselga[50], S. Bashiri[88], A. Bassalat[67,b], M. J. Basso[163a], S. Bataju[46], R. Bate[171], R. L. Bates[60], S. Batlamous[102], M. Battaglia[140], D. Battulga[19], M. Bauce[76a,76b], M. Bauer[80], P. Bauer[25], L. T. Bayer[49], L. T. Bazzano Hurrell[31], J. B. Beacham[113], T. Beau[131], J. Y. Beaucamp[93], P. H. Beauchemin[165], P. Bechtle[25], H. P. Beck[20,q], K. Becker[174], A. J. Beddall[83], V. A. Bednyakov[40], C. P. Bee[152], L. J. Beemster[16], M. Begalli[84d], M. Begel[30], J. K. Behr[49], J. F. Beirer[37], F. Beisiegel[25], M. Belfkir[120b], G. Bella[158], L. Bellagamba[24b], A. Bellerive[35], P. Bellos[21], K. Beloborodov[38], D. Benchekroun[36a], F. Bendebba[36a], Y. Benhammou[158], K. C. Benkendorfer[62], L. Beresford[49], M. Beretta[54], E. Bergeaas Kuutmann[168], N. Berger[4], B. Bergmann[136], J. Beringer[18a], G. Bernardi[5], C. Bernius[150], F. U. Bernlochner[25], F. Bernon[37], A. Berrocal Guardia[13], T. Berry[98], P. Berta[137], A. Berthold[51], S. Bethke[113], A. Betti[76a,76b], A. J. Bevan[97], L. Bezio[57], N. K. Bhalla[55], S. Bharthuar[113], S. Bhatta[152], D. S. Bhattacharya[173], P. Bhattarai[150], Z. M. Bhatti[121], K. D. Bhide[55], V. S. Bhopatkar[125], R. M. Bianchi[133], G. Bianco[24a,24b], O. Biebel[112], M. Biglietti[78a], C. S. Billingsley[46], Y. Bimgdi[36f], M. Bindi[56], A. Bingham[178], A. Bingul[22b], C. Bini[76a,76b], G. A. Bird[33], M. Birman[176], M. Biros[137], S. Biryukov[153], T. Bisanz[50], E. Bisceglie[24a,24b], J. P. Biswal[138], D. Biswas[148], I. Bloch[49], A. Blue[60], U. Blumenschein[97], J. Blumenthal[103], V. S. Bobrovnikov[40], M. Boehler[55], B. Boehm[173], D. Bogavac[37], A. G. Bogdanchikov[38], L. S. Boggia[131], V. Boisvert[98], P. Bokan[37], T. Bold[87a], M. Bomben[5], M. Bona[97], M. Boonekamp[139], A. G. Borbély[60], I. S. Bordulev[38], G. Borissov[94], D. Bortoletto[130], D. Boscherini[24b], M. Bosman[13], K. Bouaouda[36a], N. Bouchhar[170], L. Boudet[4], J. Boudreau[133], E. V. Bouhova-Thacker[94], D. Boumediene[42], R. Bouquet[58a,58b], A. Boveia[123], J. Boyd[37], D. Boye[30], I. R. Boyko[40], L. Bozianu[57], J. Bracinik[21], N. Brahimi[4], G. Brandt[178], O. Brandt[33], B. Brau[106], J. E. Brau[127], R. Brener[176], L. Brenner[118], R. Brenner[168], S. Bressler[176], G. Brianti[79a,79b], D. Britton[60],

D. Britzger[113], I. Brock[25], R. Brock[110], G. Brooijmans[43], A. J. Brooks[69], E. M. Brooks[163b], E. Brost[30], L. M. Brown[172], L. E. Bruce[62], T. L. Bruckler[130], P. A. Bruckman de Renstrom[88], B. Brüers[49], A. Bruni[24b], G. Bruni[24b], D. Brunner[48a,48b], M. Bruschi[24b], N. Bruscino[76a,76b], T. Buanes[17], Q. Buat[143], D. Buchin[113], A. G. Buckley[60], O. Bulekov[38], B. A. Bullard[150], S. Burdin[95], C. D. Burgard[50], A. M. Burger[37], B. Burghgrave[8], O. Burlayenko[55], J. Burleson[169], J. T. P. Burr[33], J. C. Burzynski[149], E. L. Busch[43], V. Büscher[103], P. J. Bussey[60], J. M. Butler[26], C. M. Buttar[60], J. M. Butterworth[99], W. Buttinger[138], C. J. Buxo Vazquez[110], A. R. Buzykaev[40], S. Cabrera Urbán[170], L. Cadamuro[67], D. Caforio[59], H. Cai[133], Y. Cai[24a,24b,115c], Y. Cai[115a], V. M. M. Cairo[37], O. Cakir[3a], N. Calace[37], P. Calafiura[18a], G. Calderini[131], P. Calfayan[35], G. Callea[60], L. P. Caloba[84b], D. Calvet[42], S. Calvet[42], R. Camacho Toro[131], S. Camarda[37], D. Camarero Munoz[27], P. Camarri[77a,77b], M. T. Camerlingo[73a,73b], D. Cameron[37], C. Camincher[172], M. Campanelli[99], A. Camplani[44], V. Canale[73a,73b], A. C. Canbay[3a], E. Canonero[98], J. Cantero[170], Y. Cao[169], F. Capocasa[27], M. Capua[45a,45b], A. Carbone[72a,72b], R. Cardarelli[77a], J. C. J. Cardenas[8], M. P. Cardiff[27], G. Carducci[45a,45b], T. Carli[37], G. Carlino[73a], J. I. Carlotto[13], B. T. Carlson[133,s], E. M. Carlson[172], J. Carmignani[95], L. Carminati[72a,72b], A. Carnelli[139], M. Carnesale[37], S. Caron[117], E. Carquin[141f], I. B. Carr[108], S. Carrá[72a], G. Carratta[24a,24b], A. M. Carroll[127], M. P. Casado[13,i], M. Caspar[49], F. L. Castillo[4], L. Castillo Garcia[13], V. Castillo Gimenez[170], N. F. Castro[134a,134e], A. Catinaccio[37], J. R. Catmore[129], T. Cavaliere[4], V. Cavaliere[30], L. J. Caviedes Betancourt[23b], Y. C. Cekmecelioglu[49], E. Celebi[83], S. Cella[37], V. Cepaitis[57], K. Cerny[126], A. S. Cerqueira[84a], A. Cerri[75a,75b], L. Cerrito[77a,77b], F. Cerutti[18a], B. Cervato[148], A. Cervelli[24b], G. Cesarini[54], S. A. Cetin[83], P. M. Chabrillat[131], J. Chan[18a], W. Y. Chan[160], J. D. Chapman[33], E. Chapon[139], B. Chargeishvili[156b], D. G. Charlton[21], C. Chauhan[137], Y. Che[115a], S. Chekanov[6], S. V. Chekulaev[163a], G. A. Chelkov[40,a], B. Chen[158], B. Chen[172], H. Chen[115a], H. Chen[30], J. Chen[145a], J. Chen[149], M. Chen[130], S. Chen[90], S. J. Chen[115a], X. Chen[145a], X. Chen[15,af], C. L. Cheng[177], H. C. Cheng[65a], S. Cheong[150], A. Cheplakov[40], E. Cheremushkina[49], E. Cherepanova[118], R. Cherkaoui El Moursli[36e], E. Cheu[7], K. Cheung[66], L. Chevalier[139], V. Chiarella[54], G. Chiarelli[75a], N. Chiedde[105], G. Chiodini[71a], A. S. Chisholm[21], A. Chitan[28b], M. Chitishvili[170], M. V. Chizhov[40,t], K. Choi[11], Y. Chou[143], E. Y. S. Chow[117], K. L. Chu[176], M. C. Chu[65a], X. Chu[14,115c], Z. Chubinidze[54], J. Chudoba[135], J. J. Chwastowski[88], D. Cieri[113], K. M. Ciesla[87a], V. Cindro[96], A. Ciocio[18a], F. Cirotto[73a,73b], Z. H. Citron[176], M. Citterio[72a], D. A. Ciubotaru[28b], A. Clark[57], P. J. Clark[53], N. Clarke Hall[99], C. Clarry[162], S. E. Clawson[49], C. Clement[48a,48b], Y. Coadou[105], M. Cobal[70a,70c], A. Coccaro[58b], R. F. Coelho Barrue[134a], R. Coelho Lopes De Sa[106], S. Coelli[72a], L. S. Colangeli[162], B. Cole[43], P. Collado Soto[102], J. Collot[61], P. Conde Muiño[134a,134g], M. P. Connell[34c], S. H. Connell[34c], E. I. Conroy[130], F. Conventi[73a,ah], H. G. Cooke[21], A. M. Cooper-Sarkar[130], F. A. Corchia[24a,24b], A. Cordeiro Oudot Choi[131], L. D. Corpe[42], M. Corradi[76a,76b], F. Corriveau[107,ab], A. Cortes-Gonzalez[19], M. J. Costa[170], F. Costanza[4], D. Costanzo[146], B. M. Cote[123], J. Couthures[4], G. Cowan[98], K. Cranmer[177], L. Cremer[50], D. Cremonini[24a,24b], S. Crépé-Renaudin[61], F. Crescioli[131], M. Cristinziani[148], M. Cristoforetti[79a,79b], V. Croft[118], J. E. Crosby[125], G. Crosetti[45a,45b], A. Cueto[102], H. Cui[99], Z. Cui[7], W. R. Cunningham[60], F. Curcio[170], J. R. Curran[53], P. Czodrowski[37], M. J. Da Cunha Sargedas De Sousa[58a,58b], J. V. Da Fonseca Pinto[84b], C. Da Via[104], W. Dabrowski[87a], T. Dado[37], S. Dahbi[155], T. Dai[109], D. Dal Santo[20], C. Dallapiccola[106], M. Dam[44], G. D'amen[30], V. D'Amico[112], J. Damp[103], J. R. Dandoy[35], D. Dannheim[37], M. Danninger[149], V. Dao[152], G. Darbo[58b], S. J. Das[30], F. Dattola[49], S. D'Auria[72a,72b], A. D'Avanzo[73a,73b], T. Davidek[137], I. Dawson[97], H. A. Day-hall[136], K. De[8], C. De Almeida Rossi[162], R. De Asmundis[73a], N. De Biase[49], S. De Castro[24a,24b], N. De Groot[117], P. de Jong[118], H. De la Torre[119], A. De Maria[115a], A. De Salvo[76a], U. De Sanctis[77a,77b], F. De Santis[71a,71b], A. De Santo[153], J. B. De Vivie De Regie[61], J. Debevc[96], D. V. Dedovich[40], J. Degens[95], A. M. Deiana[46], J. Del Peso[102], L. Delagrange[131], F. Deliot[139], C. M. Delitzsch[50], M. Della Pietra[73a,73b], D. Della Volpe[57], A. Dell'Acqua[37], L. Dell'Asta[72a,72b], M. Delmastro[4], C. C. Delogu[103], P. A. Delsart[61], S. Demers[179], M. Demichev[40], S. P. Denisov[38], H. Denizli[22a,l], L. D'Eramo[42], D. Derendarz[88], F. Derue[131], P. Dervan[95], K. Desch[25], C. Deutsch[25], F. A. Di Bello[58a,58b], A. Di Ciaccio[77a,77b], L. Di Ciaccio[4], A. Di Domenico[76a,76b], C. Di Donato[73a,73b], A. Di Girolamo[37], G. Di Gregorio[37], A. Di Luca[79a,79b], B. Di Micco[78a,78b], R. Di Nardo[78a,78b], K. F. Di Petrillo[41], M. Diamantopoulou[35], F. A. Dias[118], T. Dias Do Vale[149], M. A. Diaz[141a,141b], A. R. Didenko[40], M. Didenko[170], E. B. Diehl[109], S. Díez Cornell[49], C. Diez Pardos[148], C. Dimitriadi[151], A. Dimitrievska[21], A. Dimri[152], J. Dingfelder[25], T. Dingley[130], I.-M. Dinu[28b], S. J. Dittmeier[64b], F. Dittus[37], M. Divisek[137], B. Dixit[95], F. Djama[105], T. Djobava[156b], C. Doglioni[101,104], A. Dohnalova[29a], Z. Dolezal[137], K. Domijan[87a], K. M. Dona[41], M. Donadelli[84d], B. Dong[110], J. Donini[42],

A. D'Onofrio[73a,73b], M. D'Onofrio[95], J. Dopke[138], A. Doria[73a], N. Dos Santos Fernandes[134a], P. Dougan[104], M. T. Dova[93], A. T. Doyle[60], M. A. Draguet[130], M. P. Drescher[56], E. Dreyer[176], I. Drivas-koulouris[10], M. Drnevich[121], M. Drozdova[57], D. Du[63], T. A. du Pree[118], F. Dubinin[38], M. Dubovsky[29a], E. Duchovni[176], G. Duckeck[112], P. K. Duckett[99], O. A. Ducu[28b], D. Duda[53], A. Dudarev[37], E. R. Duden[27], M. D'uffizi[104], L. Duflot[67], M. Dührssen[37], I. Duminica[28g], A. E. Dumitriu[28b], M. Dunford[64a], S. Dungs[50], K. Dunne[48a,48b], A. Duperrin[105], H. Duran Yildiz[3a], M. Düren[59], A. Durglishvili[156b], D. Duvnjak[35], B. L. Dwyer[119], G. I. Dyckes[18a], M. Dyndal[87a], B. S. Dziedzic[37], Z. O. Earnshaw[153], G. H. Eberwein[130], B. Eckerova[29a], S. Eggebrecht[56], E. Egidio Purcino De Souza[84e], G. Eigen[17], K. Einsweiler[18a], T. Ekelof[168], P. A. Ekman[101], S. El Farkh[36b], Y. El Ghazali[63], H. El Jarrari[37], A. El Moussaouy[36a], V. Ellajosyula[168], M. Ellert[168], F. Ellinghaus[178], N. Ellis[37], J. Elmsheuser[30], M. Elsawy[120a], M. Elsing[37], D. Emeliyanov[138], Y. Enari[85], I. Ene[18a], S. Epari[13], D. Ernani Martins Neto[88], M. Errenst[178], M. Escalier[67], C. Escobar[170], E. Etzion[158], G. Evans[134a,134b], H. Evans[69], L. S. Evans[98], A. Ezhilov[38], S. Ezzarqtouni[36a], F. Fabbri[24a,24b], L. Fabbri[24a,24b], G. Facini[99], V. Fadeyev[140], R. M. Fakhrutdinov[38], D. Fakoudis[103], S. Falciano[76a], L. F. Falda Ulhoa Coelho[134a], F. Fallavollita[113], G. Falsetti[45a,45b], J. Faltova[137], C. Fan[169], K. Y. Fan[65b], Y. Fan[14], Y. Fang[14,115c], M. Fanti[72a,72b], M. Faraj[70a,70b], Z. Farazpay[100], A. Farbin[8], A. Farilla[78a], T. Farooque[110], J. N. Farr[179], S. M. Farrington[53,138], F. Fassi[36e], D. Fassouliotis[9], L. Fayard[67], P. Federic[137], P. Federicova[135], O. L. Fedin[38,a], M. Feickert[177], L. Feligioni[105], D. E. Fellers[18a], C. Feng[144a], Z. Feng[118], M. J. Fenton[166], L. Ferencz[49], P. Fernandez Martinez[68], M. J. V. Fernoux[105], J. Ferrando[94], A. Ferrari[168], P. Ferrari[117,118], R. Ferrari[74a], D. Ferrere[57], C. Ferretti[109], M. P. Fewell[1], D. Fiacco[76a,76b], F. Fiedler[103], P. Fiedler[136], S. Filimonov[38], A. Filipčič[96], E. K. Filmer[163a], F. Filthaut[117], M. C. N. Fiolhais[134a,134c,c], L. Fiorini[170], W. C. Fisher[110], T. Fitschen[104], P. M. Fitzhugh[139], I. Fleck[148], P. Fleischmann[109], T. Flick[178], M. Flores[34d,ad], L. R. Flores Castillo[65a], L. Flores Sanz De Acedo[37], F. M. Follega[79a,79b], N. Fomin[33], J. H. Foo[162], A. Formica[139], A. C. Forti[104], E. Fortin[37], A. W. Fortman[18a], L. Fountas[9,j], D. Fournier[67], H. Fox[94], P. Francavilla[75a,75b], S. Francescato[62], S. Franchellucci[57], M. Franchini[24a,24b], S. Franchino[64a], D. Francis[37], L. Franco[117], V. Franco Lima[37], L. Franconi[49], M. Franklin[62], G. Frattari[27], Y. Y. Frid[158], J. Friend[60], N. Fritzsche[37], A. Froch[57], D. Froidevaux[37], J. A. Frost[130], Y. Fu[110], S. Fuenzalida Garrido[141f], M. Fujimoto[105], K. Y. Fung[65a], E. Furtado De Simas Filho[84e], M. Furukawa[160], J. Fuster[170], A. Gaa[56], A. Gabrielli[24a,24b], A. Gabrielli[162], P. Gadow[37], G. Gagliardi[58a,58b], L. G. Gagnon[18a], S. Gaid[89b], S. Galantzan[158], J. Gallagher[1], E. J. Gallas[130], A. L. Gallen[168], B. J. Gallop[138], K. K. Gan[123], S. Ganguly[160], Y. Gao[53], A. Garabaglu[143], F. M. Garay Walls[141a,141b], B. Garcia[30], C. García[170], A. Garcia Alonso[118], A. G. Garcia Caffaro[179], J. E. García Navarro[170], M. Garcia-Sciveres[18a], G. L. Gardner[132], R. W. Gardner[41], N. Garelli[165], R. B. Garg[150], J. M. Gargan[53], C. A. Garner[162], C. M. Garvey[34a], V. K. Gassmann[165], G. Gaudio[74a], V. Gautam[13], P. Gauzzi[76a,76b], J. Gavranovic[96], I. L. Gavrilenko[38], A. Gavrilyuk[38], C. Gay[171], G. Gaycken[127], E. N. Gazis[10], A. Gekow[123], C. Gemme[58b], M. H. Genest[61], A. D. Gentry[116], S. George[98], W. F. George[21], T. Geralis[47], A. A. Gerwin[124], P. Gessinger-Befurt[37], M. E. Geyik[178], M. Ghani[174], K. Ghorbanian[97], A. Ghosal[148], A. Ghosh[166], A. Ghosh[7], B. Giacobbe[24b], S. Giagu[76a,76b], T. Giani[118], A. Giannini[63], S. M. Gibson[98], M. Gignac[140], D. T. Gil[87b], A. K. Gilbert[87a], B. J. Gilbert[43], D. Gillberg[35], G. Gilles[118], L. Ginabat[131], D. M. Gingrich[2,ag], M. P. Giordani[70a,70c], P. F. Giraud[139], G. Giugliarelli[70a,70c], D. Giugni[72a], F. Giuli[77a,77b], I. Gkialas[9,j], L. K. Gladilin[38], C. Glasman[102], G. Glemža[49], M. Glisic[127], I. Gnesi[45b], Y. Go[30], M. Goblirsch-Kolb[37], B. Gocke[50], D. Godin[111], B. Gokturk[22a], S. Goldfarb[108], T. Golling[57], M. G. D. Gololo[34c], D. Golubkov[38], J. P. Gombas[110], A. Gomes[134a,134b], G. Gomes Da Silva[148], A. J. Gomez Delegido[170], R. Gonçalo[134a], L. Gonella[21], A. Gongadze[156c], F. Gonnella[21], J. L. Gonski[150], R. Y. González Andana[53], S. González de la Hoz[170], R. Gonzalez Lopez[95], C. Gonzalez Renteria[18a], M. V. Gonzalez Rodrigues[49], R. Gonzalez Suarez[168], S. Gonzalez-Sevilla[57], L. Goossens[37], B. Gorini[37], E. Gorini[71a,71b], A. Gorišek[96], T. C. Gosart[132], A. T. Goshaw[52], M. I. Gostkin[40], S. Goswami[125], C. A. Gottardo[37], S. A. Gotz[112], M. Gouighri[36b], A. G. Goussiou[143], N. Govender[34c], R. P. Grabarczyk[130], I. Grabowska-Bold[87a], K. Graham[35], E. Gramstad[129], S. Grancagnolo[71a,71b], C. M. Grant[1,139], P. M. Gravila[28f], F. G. Gravili[71a,71b], H. M. Gray[18a], M. Greco[113], M. J. Green[1], C. Grefe[25], A. S. Grefsrud[17], I. M. Gregor[49], K. T. Greif[166], P. Grenier[150], S. G. Grewe[113], A. A. Grillo[140], K. Grimm[32], S. Grinstein[13,x], J.-F. Grivaz[67], E. Gross[176], J. Grosse-Knetter[56], L. Guan[109], G. Guerrieri[37], R. Gugel[103], J. A. M. Guhit[109], A. Guida[19], E. Guilloton[174], S. Guindon[37], F. Guo[14,115c], J. Guo[145a], L. Guo[49], L. Guo[115b,v], Y. Guo[109], A. Gupta[50], R. Gupta[133], S. Gurbuz[25], S. S. Gurdasani[49], G. Gustavino[76a,76b], P. Gutierrez[124], L. F. Gutierrez Zagazeta[132], M. Gutsche[51], C. Gutschow[99], C. Gwenlan[130], C. B. Gwilliam[95], E. S. Haaland[129], A. Haas[121],

M. Habedank[60], C. Haber[18a], H. K. Hadavand[8], A. Haddad[42], A. Hadef[51], A. I. Hagan[94], J. J. Hahn[148], E. H. Haines[99], M. Haleem[173], J. Haley[125], G. D. Hallewell[105], L. Halser[20], K. Hamano[172], M. Hamer[25], S. E. D. Hammoud[67], E. J. Hampshire[98], J. Han[144a], L. Han[115a], L. Han[63], S. Han[18a], K. Hanagaki[85], M. Hance[140], D. A. Hangal[43], H. Hanif[149], M. D. Hank[132], J. B. Hansen[44], P. H. Hansen[44], D. Harada[57], T. Harenberg[178], S. Harkusha[180], M. L. Harris[106], Y. T. Harris[25], J. Harrison[13], N. M. Harrison[123], P. F. Harrison[174], N. M. Hartman[113], N. M. Hartmann[112], R. Z. Hasan[98,138], Y. Hasegawa[147], F. Haslbeck[130], S. Hassan[17], R. Hauser[110], C. M. Hawkes[21], R. J. Hawkings[37], Y. Hayashi[160], D. Hayden[110], C. Hayes[109], R. L. Hayes[118], C. P. Hays[130], J. M. Hays[97], H. S. Hayward[95], F. He[63], M. He[14,115c], Y. He[49], Y. He[99], N. B. Heatley[97], V. Hedberg[101], A. L. Heggelund[129], C. Heidegger[55], K. K. Heidegger[55], J. Heilman[35], S. Heim[49], T. Heim[18a], J. G. Heinlein[132], J. J. Heinrich[127], L. Heinrich[113,ae], J. Hejbal[135], A. Held[177], S. Hellesund[17], C. M. Helling[171], S. Hellman[48a,48b], L. Henkelmann[33], A. M. Henriques Correia[37], H. Herde[101], Y. Hernández Jiménez[152], L. M. Herrmann[25], T. Herrmann[51], G. Herten[55], R. Hertenberger[112], L. Hervas[37], M. E. Hesping[103], N. P. Hessey[163a], J. Hessler[113], M. Hidaoui[36b], N. Hidic[137], E. Hill[162], S. J. Hillier[21], J. R. Hinds[110], F. Hinterkeuser[25], M. Hirose[128], S. Hirose[164], D. Hirschbuehl[178], T. G. Hitchings[104], B. Hiti[96], J. Hobbs[152], R. Hobincu[28e], N. Hod[176], M. C. Hodgkinson[146], B. H. Hodkinson[130], A. Hoecker[37], D. D. Hofer[109], J. Hofer[170], M. Holzbock[37], L. B. A. H. Hommels[33], B. P. Honan[104], J. J. Hong[69], J. Hong[145a], T. M. Hong[133], B. H. Hooberman[169], W. H. Hopkins[6], M. C. Hoppesch[169], Y. Horii[114], M. E. Horstmann[113], S. Hou[155], M. R. Housenga[169], A. S. Howard[96], J. Howarth[60], J. Hoya[6], M. Hrabovsky[126], T. Hryn'ova[4], P. J. Hsu[66], S.-C. Hsu[143], T. Hsu[67], M. Hu[18a], Q. Hu[63], S. Huang[33], X. Huang[14,115c], Y. Huang[137], Y. Huang[115b], Y. Huang[103], Y. Huang[14], Z. Huang[104], Z. Hubacek[136], M. Huebner[25], F. Huegging[25], T. B. Huffman[130], M. Hufnagel Maranha De Faria[84a], C. A. Hugli[49], M. Huhtinen[37], S. K. Huiberts[17], R. Hulsken[107], C. E. Hultquist[18a], N. Huseynov[12,g], J. Huston[110], J. Huth[62], R. Hyneman[7], G. Iacobucci[57], G. Iakovidis[30], L. Iconomidou-Fayard[67], J. P. Iddon[37], P. Iengo[73a,73b], R. Iguchi[160], Y. Iiyama[160], T. Iizawa[130], Y. Ikegami[85], D. Iliadis[159], N. Ilic[162], H. Imam[84c], G. Inacio Goncalves[84d], S. A. Infante Cabanas[141c], T. Ingebretsen Carlson[48a,48b], J. M. Inglis[97], G. Introzzi[74a,74b], M. Iodice[78a], V. Ippolito[76a,76b], R. K. Irwin[95], M. Ishino[160], W. Islam[177], C. Issever[19], S. Istin[22a,al], H. Ito[175], R. Iuppa[79a,79b], A. Ivina[176], V. Izzo[73a], P. Jacka[135], P. Jackson[1], P. Jain[49], K. Jakobs[55], T. Jakoubek[176], J. Jamieson[60], W. Jang[160], M. Javurkova[106], P. Jawahar[104], L. Jeanty[127], J. Jejelava[156a], P. Jenni[55,f], C. E. Jessiman[35], C. Jia[144a], H. Jia[171], J. Jia[152], X. Jia[14,115c], Z. Jia[115a], C. Jiang[53], Q. Jiang[65b], S. Jiggins[49], J. Jimenez Pena[13], S. Jin[115a], A. Jinaru[28b], O. Jinnouchi[142], P. Johansson[146], K. A. Johns[7], J. W. Johnson[140], F. A. Jolly[49], D. M. Jones[153], E. Jones[49], K. S. Jones[8], P. Jones[33], R. W. L. Jones[94], T. J. Jones[95], H. L. Joos[37,56], R. Joshi[123], J. Jovicevic[16], X. Ju[18a], J. J. Junggeburth[37], T. Junkermann[64a], A. Juste Rozas[13,x], M. K. Juzek[88], S. Kabana[141e], A. Kaczmarska[88], M. Kado[113], H. Kagan[123], M. Kagan[150], A. Kahn[132], C. Kahra[103], T. Kaji[160], E. Kajomovitz[157], N. Kakati[176], I. Kalaitzidou[55], N. J. Kang[140], D. Kar[34g], K. Karava[130], E. Karentzos[25], O. Karkout[118], S. N. Karpov[40], Z. M. Karpova[40], V. Kartvelishvili[94], A. N. Karyukhin[38], E. Kasimi[159], J. Katzy[49], S. Kaur[35], K. Kawade[147], M. P. Kawale[124], C. Kawamoto[90], T. Kawamoto[63], E. F. Kay[37], F. I. Kaya[165], S. Kazakos[110], V. F. Kazanin[38], Y. Ke[152], J. M. Keaveney[34a], R. Keeler[172], G. V. Kehris[62], J. S. Keller[35], J. J. Kempster[153], O. Kepka[135], J. Kerr[163b], B. P. Kerridge[138], B. P. Kerševan[96], L. Keszeghova[29a], R. A. Khan[133], A. Khanov[125], A. G. Kharlamov[38], T. Kharlamova[38], E. E. Khoda[143], M. Kholodenko[134a], T. J. Khoo[19], G. Khoriauli[173], J. Khubua[156b,*], Y. A. R. Khwaira[131], B. Kibirige[34g], D. Kim[6], D. W. Kim[48a,48b], Y. K. Kim[41], N. Kimura[99], M. K. Kingston[56], A. Kirchhoff[56], C. Kirfel[25], F. Kirfel[25], J. Kirk[138], A. E. Kiryunin[113], S. Kita[164], C. Kitsaki[10], O. Kivernyk[25], M. Klassen[165], C. Klein[35], L. Klein[173], M. H. Klein[46], S. B. Klein[57], U. Klein[95], A. Klimentov[30], T. Klioutchnikova[37], P. Kluit[118], S. Kluth[113], E. Kneringer[80], T. M. Knight[162], A. Knue[50], D. Kobylianskii[176], S. F. Koch[130], M. Kocian[150], P. Kodyš[137], D. M. Koeck[127], P. T. Koenig[25], T. Koffas[35], O. Kolay[51], I. Koletsou[4], T. Komarek[88], K. Köneke[56], A. X. Y. Kong[1], T. Kono[122], N. Konstantinidis[99], P. Kontaxakis[57], B. Konya[101], R. Kopeliansky[43], S. Koperny[87a], K. Korcyl[88], K. Kordas[159,e], A. Korn[99], S. Korn[56], I. Korolkov[13], N. Korotkova[38], B. Kortman[118], O. Kortner[113], S. Kortner[113], W. H. Kostecka[119], V. V. Kostyukhin[148], A. Kotsokechagia[37], A. Kotwal[52], A. Koulouris[37], A. Kourkoumeli-Charalampidi[74a,74b], C. Kourkoumelis[9], E. Kourlitis[113,ae], O. Kovanda[127], R. Kowalewski[172], W. Kozanecki[127], A. S. Kozhin[38], V. A. Kramarenko[38], G. Kramberger[96], P. Kramer[25], M. W. Krasny[131], A. Krasznahorkay[106], A. C. Kraus[119], J. W. Kraus[178], J. A. Kremer[49], N. B. Krengel[148], T. Kresse[51], L. Kretschmann[178], J. Kretzschmar[95], K. Kreul[19],

P. Krieger[162], K. Krizka[21], K. Kroeninger[50], H. Kroha[113], J. Kroll[135], J. Kroll[132], K. S. Krowpman[110], U. Kruchonak[40], H. Krüger[25], N. Krumnack[82], M. C. Kruse[52], O. Kuchinskaia[38], S. Kuday[3a], S. Kuehn[37], R. Kuesters[55], T. Kuhl[49], V. Kukhtin[40], Y. Kulchitsky[40], S. Kuleshov[141b,141d], M. Kumar[34g], N. Kumari[49], P. Kumari[163b], A. Kupco[135], T. Kupfer[50], A. Kupich[38], O. Kuprash[55], H. Kurashige[86], L. L. Kurchaninov[163a], O. Kurdysh[4], Y. A. Kurochkin[39], A. Kurova[38], M. Kuze[142], A. K. Kvam[106], J. Kvita[126], N. G. Kyriacou[109], L. A. O. Laatu[105], C. Lacasta[170], F. Lacava[76a,76b], H. Lacker[19], D. Lacour[131], N. N. Lad[99], E. Ladygin[40], A. Lafarge[42], B. Laforge[131], T. Lagouri[179], F. Z. Lahbabi[36a], S. Lai[56], J. E. Lambert[172], S. Lammers[69], W. Lampl[7], C. Lampoudis[159,e], G. Lamprinoudis[103], A. N. Lancaster[119], E. Lançon[30], U. Landgraf[55], M. P. J. Landon[97], V. S. Lang[55], O. K. B. Langrekken[129], A. J. Lankford[166], F. Lanni[37], K. Lantzsch[25], A. Lanza[74a], M. Lanzac Berrocal[170], J. F. Laporte[139], T. Lari[72a], D. Larsen[17], F. Lasagni Manghi[24b], M. Lassnig[37], V. Latonova[135], S. D. Lawlor[146], Z. Lawrence[104], R. Lazaridou[174], M. Lazzaroni[72a,72b], H. D. M. Le[110], E. M. Le Boulicaut[179], L. T. Le Pottier[18a], B. Leban[24a,24b], M. LeBlanc[104], F. Ledroit-Guillon[61], S. C. Lee[155], T. F. Lee[95], L. L. Leeuw[34c,aj], M. Lefebvre[172], C. Leggett[18a], G. Lehmann Miotto[37], M. Leigh[57], W. A. Leight[106], W. Leinonen[117], A. Leisos[159,u], M. A. L. Leite[84c], C. E. Leitgeb[19], R. Leitner[137], K. J. C. Leney[46], T. Lenz[25], S. Leone[75a], C. Leonidopoulos[53], A. Leopold[151], J. H. Lepage Bourbonnais[35], R. Les[110], C. G. Lester[33], M. Levchenko[38], J. Levêque[4], L. J. Levinson[176], G. Levrini[24a,24b], M. P. Lewicki[88], C. Lewis[143], D. J. Lewis[4], L. Lewitt[146], A. Li[30], B. Li[144a], C. Li[109], C.-Q. Li[113], H. Li[63], H. Li[144a], H. Li[104], H. Li[15], H. Li[144a], J. Li[145a], K. Li[14], L. Li[145a], R. Li[179], S. Li[14,115c], S. Li[145a,145b,d], T. Li[5], X. Li[107], Z. Li[160], Z. Li[14,115c], Z. Li[63], S. Liang[14,115c], Z. Liang[14], M. Liberatore[139], B. Liberti[77a], K. Lie[65c], J. Lieber Marin[84e], H. Lien[69], H. Lin[109], L. Linden[112], R. E. Lindley[7], J. H. Lindon[2], J. Ling[62], E. Lipeles[132], A. Lipniacka[17], A. Lister[171], J. D. Little[69], B. Liu[14], B. X. Liu[115b], D. Liu[145a,145b], E. H. L. Liu[21], J. K. K. Liu[33], K. Liu[145b], K. Liu[145a,145b], M. Liu[63], M. Y. Liu[63], P. Liu[14], Q. Liu[143,145a,145b], X. Liu[63], X. Liu[144a], Y. Liu[115b,115c], Y. L. Liu[144a], Y. W. Liu[63], S. L. Lloyd[97], E. M. Lobodzinska[49], P. Loch[7], E. Lodhi[162], T. Lohse[19], K. Lohwasser[146], E. Loiacono[49], J. D. Lomas[21], J. D. Long[43], I. Longarini[166], R. Longo[169], A. Lopez Solis[49], N. A. Lopez-canelas[7], N. Lorenzo Martinez[4], A. M. Lory[112], M. Losada[120a], G. Löschcke Centeno[153], O. Loseva[38], X. Lou[48a,48b], X. Lou[14,115c], A. Lounis[67], P. A. Love[94], G. Lu[14,115c], M. Lu[67], S. Lu[132], Y. J. Lu[155], H. J. Lubatti[143], C. Luci[76a,76b], F. L. Lucio Alves[115a], F. Luehring[69], B. S. Lunday[132], O. Lundberg[151], B. Lund-Jensen[151,*], N. A. Luongo[6], M. S. Lutz[37], A. B. Lux[26], D. Lynn[30], R. Lysak[135], E. Lytken[101], V. Lyubushkin[40], T. Lyubushkina[40], M. M. Lyukova[152], M. Firdaus M. Soberi[53], H. Ma[30], K. Ma[63], L. L. Ma[144a], W. Ma[63], Y. Ma[125], J. C. MacDonald[103], P. C. Machado De Abreu Farias[84e], R. Madar[42], T. Madula[99], J. Maeda[86], T. Maeno[30], P. T. Mafa[34c,k], H. Maguire[146], V. Maiboroda[139], A. Maio[134a,134b,134d], K. Maj[87a], O. Majersky[49], S. Majewski[127], R. Makhmanazarov[38], N. Makovec[67], V. Maksimovic[16], B. Malaescu[131], Pa. Malecki[88], V. P. Maleev[38], F. Malek[61,p], M. Mali[96], D. Malito[98], U. Mallik[81,*], S. Maltezos[10], S. Malyukov[40], J. Mamuzic[13], G. Mancini[54], M. N. Mancini[27], G. Manco[74a,74b], J. P. Mandalia[97], S. S. Mandarry[153], I. Mandić[96], L. Manhaes de Andrade Filho[84a], I. M. Maniatis[176], J. Manjarres Ramos[92], D. C. Mankad[176], A. Mann[112], S. Manzoni[37], L. Mao[145a], X. Mapekula[34c], A. Marantis[159,u], G. Marchiori[5], M. Marcisovsky[135], C. Marcon[72a], M. Marinescu[21], S. Marium[49], M. Marjanovic[124], A. Markhoos[55], M. Markovitch[67], M. K. Maroun[106], E. J. Marshall[94], Z. Marshall[18a], S. Marti-Garcia[170], J. Martin[99], T. A. Martin[138], V. J. Martin[53], B. Martin dit Latour[17], L. Martinelli[76a,76b], M. Martinez[13,x], P. Martinez Agullo[170], V. I. Martinez Outschoorn[106], P. Martinez Suarez[13], S. Martin-Haugh[138], G. Martinovicova[137], V. S. Martoiu[28b], A. C. Martyniuk[99], A. Marzin[37], D. Mascione[79a,79b], L. Masetti[103], J. Masik[104], A. L. Maslennikov[40], S. L. Mason[43], P. Massarotti[73a,73b], P. Mastrandrea[75a,75b], A. Mastroberardino[45a,45b], T. Masubuchi[128], T. T. Mathew[127], J. Matousek[137], D. M. Mattern[50], J. Maurer[28b], T. Maurin[60], A. J. Maury[67], B. Maček[96], D. A. Maximov[38], A. E. May[104], E. Mayer[42], R. Mazini[34g], I. Maznas[119], M. Mazza[110], S. M. Mazza[140], E. Mazzeo[72a,72b], J. P. Mc Gowan[172], S. P. Mc Kee[109], C. A. Mc Lean[6], C. C. McCracken[171], E. F. McDonald[108], A. E. McDougall[118], L. F. Mcelhinney[94], J. A. Mcfayden[153], R. P. McGovern[132], R. P. Mckenzie[34g], T. C. Mclachlan[49], D. J. Mclaughlin[99], S. J. McMahon[138], C. M. Mcpartland[95], R. A. McPherson[172,ab], S. Mehlhase[112], A. Mehta[95], D. Melini[170], B. R. Mellado Garcia[34g], A. H. Melo[56], F. Meloni[49], A. M. Mendes Jacques Da Costa[104], H. Y. Meng[162], L. Meng[94], S. Menke[113], M. Mentink[37], E. Meoni[45a,45b], G. Mercado[119], S. Merianos[159], C. Merlassino[70a,70c], C. Meroni[72a,72b], J. Metcalfe[6], A. S. Mete[6], E. Meuser[103], C. Meyer[69], J.-P. Meyer[139], R. P. Middleton[138], L. Mijović[53], G. Mikenberg[176],

M. Mikestikova[135], M. Mikuž[96], H. Mildner[103], A. Milic[37], D. W. Miller[41], E. H. Miller[150], L. S. Miller[35], A. Milov[176], D. A. Milstead[48a,48b], T. Min[115a], A. A. Minaenko[38], I. A. Minashvili[156b], A. I. Mincer[121], B. Mindur[87a], M. Mineev[40], Y. Mino[90], L. M. Mir[13], M. Miralles Lopez[60], M. Mironova[18a], M. C. Missio[117], A. Mitra[174], V. A. Mitsou[170], Y. Mitsumori[114], O. Miu[162], P. S. Miyagawa[97], T. Mkrtchyan[64a], M. Mlinarevic[99], T. Mlinarevic[99], M. Mlynarikova[37], S. Mobius[20], P. Mogg[112], M. H. Mohamed Farook[116], A. F. Mohammed[14,115c], S. Mohapatra[43], S. Mohiuddin[125], G. Mokgatitswane[34g], L. Moleri[176], B. Mondal[148], S. Mondal[136], K. Mönig[49], E. Monnier[105], L. Monsonis Romero[170], J. Montejo Berlingen[13], A. Montella[48a,48b], M. Montella[123], F. Montereali[78a,78b], F. Monticelli[93], S. Monzani[70a,70c], A. Morancho Tarda[44], N. Morange[67], A. L. Moreira De Carvalho[49], M. Moreno Llácer[170], C. Moreno Martinez[57], J. M. Moreno Perez[23b], P. Morettini[58b], S. Morgenstern[37], M. Morii[62], M. Morinaga[160], M. Moritsu[91], F. Morodei[76a,76b], P. Moschovakos[37], B. Moser[130], M. Mosidze[156b], T. Moskalets[46], P. Moskvitina[117], J. Moss[32,m], P. Moszkowicz[87a], A. Moussa[36d], Y. Moyal[176], E. J. W. Moyse[106], O. Mtintsilana[34g], S. Muanza[105], J. Mueller[133], R. Müller[37], G. A. Mullier[168], A. J. Mullin[33], J. J. Mullin[52], A. E. Mulski[62], D. P. Mungo[162], D. Munoz Perez[170], F. J. Munoz Sanchez[104], M. Murin[104], W. J. Murray[138,174], M. Muškinja[96], C. Mwewa[30], A. G. Myagkov[38,a], A. J. Myers[8], G. Myers[109], M. Myska[136], B. P. Nachman[18a], K. Nagai[130], K. Nagano[85], R. Nagasaka[160], J. L. Nagle[30,ai], E. Nagy[105], A. M. Nairz[37], Y. Nakahama[85], K. Nakamura[85], K. Nakkalil[5], H. Nanjo[128], E. A. Narayanan[46], Y. Narukawa[160], I. Naryshkin[38], L. Nasella[72a,72b], S. Nasri[120b], C. Nass[25], G. Navarro[23a], J. Navarro-Gonzalez[170], A. Nayaz[19], P. Y. Nechaeva[38], S. Nechaeva[24a,24b], F. Nechansky[135], L. Nedic[130], T. J. Neep[21], A. Negri[74a,74b], M. Negrini[24b], C. Nellist[118], C. Nelson[107], K. Nelson[109], S. Nemecek[135], M. Nessi[37,h], M. S. Neubauer[169], F. Neuhaus[103], J. Newell[95], P. R. Newman[21], Y. W. Y. Ng[169], B. Ngair[120a], H. D. N. Nguyen[111], R. B. Nickerson[130], R. Nicolaidou[139], J. Nielsen[140], M. Niemeyer[56], J. Niermann[37], N. Nikiforou[37], V. Nikolaenko[38,a], I. Nikolic-Audit[131], P. Nilsson[30], I. Ninca[49], G. Ninio[158], A. Nisati[76a], N. Nishu[2], R. Nisius[113], N. Nitika[70a,70c], J.-E. Nitschke[51], E. K. Nkadimeng[34g], T. Nobe[160], T. Nommensen[154], M. B. Norfolk[146], B. J. Norman[35], M. Noury[36a], J. Novak[96], T. Novak[96], R. Novotny[116], L. Nozka[126], K. Ntekas[166], N. M. J. Nunes De Moura Junior[84b], J. Ocariz[131], A. Ochi[86], I. Ochoa[134a], S. Oerdek[49,y], J. T. Offermann[41], A. Ogrodnik[137], A. Oh[104], C. C. Ohm[151], H. Oide[85], R. Oishi[160], M. L. Ojeda[37], Y. Okumura[160], L. F. Oleiro Seabra[134a], I. Oleksiyuk[57], S. A. Olivares Pino[141d], G. Oliveira Correa[13], D. Oliveira Damazio[30], J. L. Oliver[166], Ö. O. Öncel[55], A. P. O'Neill[20], A. Onofre[134a,134e], P. U. E. Onyisi[11], M. J. Oreglia[41], D. Orestano[78a,78b], R. S. Orr[162], L. M. Osojnak[132], Y. Osumi[114], G. Otero y Garzon[31], H. Otono[91], G. J. Ottino[18a], M. Ouchrif[36d], F. Ould-Saada[129], T. Ovsiannikova[143], M. Owen[60], R. E. Owen[138], V. E. Ozcan[22a], F. Ozturk[88], N. Ozturk[8], S. Ozturk[83], H. A. Pacey[130], K. Pachal[163a], A. Pacheco Pages[13], C. Padilla Aranda[13], G. Padovano[76a,76b], S. Pagan Griso[18a], G. Palacino[69], A. Palazzo[71a,71b], J. Pampel[25], J. Pan[179], T. Pan[65a], D. K. Panchal[11], C. E. Pandini[118], J. G. Panduro Vazquez[138], H. D. Pandya[1], H. Pang[139], P. Pani[49], G. Panizzo[70a,70c], L. Panwar[131], L. Paolozzi[57], S. Parajuli[169], A. Paramonov[6], C. Paraskevopoulos[54], D. Paredes Hernandez[65b], A. Pareti[74a,74b], K. R. Park[43], T. H. Park[113], F. Parodi[58a,58b], J. A. Parsons[43], U. Parzefall[55], B. Pascual Dias[42], L. Pascual Dominguez[102], E. Pasqualucci[76a], S. Passaggio[58b], F. Pastore[98], P. Patel[88], U. M. Patel[52], J. R. Pater[104], T. Pauly[37], F. Pauwels[137], C. I. Pazos[165], M. Pedersen[129], R. Pedro[134a], S. V. Peleganchuk[38], O. Penc[37], E. A. Pender[53], S. Peng[15], G. D. Penn[179], K. E. Penski[112], M. Penzin[38], B. S. Peralva[84d], A. P. Pereira Peixoto[143], L. Pereira Sanchez[150], D. V. Perepelitsa[30,ai], G. Perera[106], E. Perez Codina[163a], M. Perganti[10], H. Pernegger[37], S. Perrella[76a,76b], O. Perrin[42], K. Peters[49], R. F. Y. Peters[104], B. A. Petersen[37], T. C. Petersen[44], E. Petit[105], V. Petousis[136], C. Petridou[159,e], T. Petru[137], A. Petrukhin[148], M. Pettee[18a], A. Petukhov[83], K. Petukhova[37], R. Pezoa[141f], L. Pezzotti[24a,24b], G. Pezzullo[179], L. Pfaffenbichler[37], A. J. Pfleger[37], T. M. Pham[177], T. Pham[108], P. W. Phillips[138], G. Piacquadio[152], E. Pianori[18a], F. Piazza[127], R. Piegaia[31], D. Pietreanu[28b], A. D. Pilkington[104], M. Pinamonti[70a,70c], J. L. Pinfold[2], B. C. Pinheiro Pereira[134a], J. Pinol Bel[13], A. E. Pinto Pinoargote[139], L. Pintucci[70a,70c], K. M. Piper[153], A. Pirttikoski[57], D. A. Pizzi[35], L. Pizzimento[65b], M.-A. Pleier[30], V. Pleskot[137], E. Plotnikova[40], G. Poddar[97], R. Poettgen[101], L. Poggioli[131], S. Polacek[137], G. Polesello[74a], A. Poley[149,163a], A. Polini[24b], C. S. Pollard[174], Z. B. Pollock[123], E. Pompa Pacchi[124], N. I. Pond[99], D. Ponomarenko[69], L. Pontecorvo[37], S. Popa[28a], G. A. Popeneciu[28d], A. Poreba[37], D. M. Portillo Quintero[163a], S. Pospisil[136], M. A. Postill[146], P. Postolache[28c], K. Potamianos[174], P. A. Potepa[87a], I. N. Potrap[40], C. J. Potter[33], H. Potti[154], J. Poveda[170], M. E. Pozo Astigarraga[37], A. Prades Ibanez[77a,77b], J. Pretel[172],

D. Price[104], M. Primavera[71a], L. Primomo[70a,70c], M. A. Principe Martin[102], R. Privara[126], T. Procter[60], M. L. Proffitt[143], N. Proklova[132], K. Prokofiev[65c], G. Proto[113], J. Proudfoot[6], M. Przybycien[87a], W. W. Przygoda[87b], A. Psallidas[47], J. E. Puddefoot[146], D. Pudzha[55], D. Pyatiizbyantseva[117], J. Qian[109], R. Qian[110], D. Qichen[104], Y. Qin[13], T. Qiu[53], A. Quadt[56], M. Queitsch-Maitland[104], G. Quetant[57], R. P. Quinn[171], G. Rabanal Bolanos[62], D. Rafanoharana[55], F. Raffaeli[77a,77b], F. Ragusa[72a,72b], J. L. Rainbolt[41], J. A. Raine[57], S. Rajagopalan[30], E. Ramakoti[38], L. Rambelli[58a,58b], I. A. Ramirez-Berend[35], K. Ran[49,115c], D. S. Rankin[132], N. P. Rapheeha[34g], H. Rasheed[28b], V. Raskina[131], D. F. Rassloff[64a], A. Rastogi[18a], S. Rave[103], S. Ravera[58a,58b], B. Ravina[37], I. Ravinovich[176], M. Raymond[37], A. L. Read[129], N. P. Readioff[146], D. M. Rebuzzi[74a,74b], A. S. Reed[113], K. Reeves[27], J. A. Reidelsturz[178], D. Reikher[127], A. Rej[50], C. Rembser[37], H. Ren[63], M. Renda[28b], F. Renner[49], A. G. Rennie[166], A. L. Rescia[49], S. Resconi[72a], M. Ressegotti[58a,58b], S. Rettie[37], W. F. Rettie[35], J. G. Reyes Rivera[110], E. Reynolds[18a], O. L. Rezanova[40], P. Reznicek[137], H. Riani[36d], N. Ribaric[52], E. Ricci[79a,79b], R. Richter[113], S. Richter[48a,48b], E. Richter-Was[87b], M. Ridel[131], S. Ridouani[36d], P. Rieck[121], P. Riedler[37], E. M. Riefel[48a,48b], J. O. Rieger[118], M. Rijssenbeek[152], M. Rimoldi[37], L. Rinaldi[24a,24b], P. Rincke[56,168], G. Ripellino[168], I. Riu[13], J. C. Rivera Vergara[172], F. Rizatdinova[125], E. Rizvi[97], B. R. Roberts[18a], S. S. Roberts[140], D. Robinson[33], M. Robles Manzano[103], A. Robson[60], A. Rocchi[77a,77b], C. Roda[75a,75b], S. Rodriguez Bosca[37], Y. Rodriguez Garcia[23a], A. M. Rodríguez Vera[119], S. Roe[37], J. T. Roemer[37], O. Røhne[129], C. P. A. Roland[131], J. Roloff[30], A. Romaniouk[80], E. Romano[74a,74b], M. Romano[24b], A. C. Romero Hernandez[169], N. Rompotis[95], L. Roos[131], S. Rosati[76a], B. J. Rosser[41], E. Rossi[130], E. Rossi[73a,73b], L. P. Rossi[62], L. Rossini[55], R. Rosten[123], M. Rotaru[28b], B. Rottler[55], D. Rousseau[67], D. Rousso[49], S. Roy-Garand[162], A. Rozanov[105], Z. M. A. Rozario[60], Y. Rozen[157], A. Rubio Jimenez[170], V. H. Ruelas Rivera[19], T. A. Ruggeri[1], A. Ruggiero[130], A. Ruiz-Martinez[170], A. Rummler[37], Z. Rurikova[55], N. A. Rusakovich[40], H. L. Russell[172], G. Russo[76a,76b], J. P. Rutherfoord[7], S. Rutherford Colmenares[33], M. Rybar[137], E. B. Rye[129], A. Ryzhov[46], J. A. Sabater Iglesias[57], H. F.-W. Sadrozinski[140], F. Safai Tehrani[76a], S. Saha[1], M. Sahinsoy[83], A. Saibel[170], B. T. Saifuddin[124], M. Saimpert[139], M. Saito[160], T. Saito[160], A. Sala[72a,72b], D. Salamani[37], A. Salnikov[150], J. Salt[170], A. Salvador Salas[158], D. Salvatore[45a,45b], F. Salvatore[153], A. Salzburger[37], D. Sammel[55], E. Sampson[94], D. Sampsonidis[159,e], D. Sampsonidou[127], J. Sánchez[170], V. Sanchez Sebastian[170], H. Sandaker[129], C. O. Sander[49], J. A. Sandesara[106], M. Sandhoff[178], C. Sandoval[23b], L. Sanfilippo[64a], D. P. C. Sankey[138], T. Sano[90], A. Sansoni[54], L. Santi[37], C. Santoni[42], H. Santos[134a,134b], A. Santra[176], E. Sanzani[24a,24b], K. A. Saoucha[89b], J. G. Saraiva[134a,134d], J. Sardain[7], O. Sasaki[85], K. Sato[164], C. Sauer[37], E. Sauvan[4], P. Savard[162,ag], R. Sawada[160], C. Sawyer[138], L. Sawyer[100], C. Sbarra[24b], A. Sbrizzi[24a,24b], T. Scanlon[99], J. Schaarschmidt[143], U. Schäfer[103], A. C. Schaffer[46,67], D. Schaile[112], R. D. Schamberger[152], C. Scharf[19], M. M. Schefer[20], V. A. Schegelsky[38], D. Scheirich[137], M. Schernau[141e], C. Scheulen[57], C. Schiavi[58a,58b], M. Schioppa[45a,45b], B. Schlag[150], S. Schlenker[37], J. Schmeing[178], M. A. Schmidt[178], K. Schmieden[103], C. Schmitt[103], N. Schmitt[103], S. Schmitt[49], L. Schoeffel[139], A. Schoening[64b], P. G. Scholer[35], E. Schopf[148], M. Schott[25], S. Schramm[57], T. Schroer[57], H.-C. Schultz-Coulon[64a], M. Schumacher[55], B. A. Schumm[140], Ph. Schune[139], H. R. Schwartz[140], A. Schwartzman[150], T. A. Schwarz[109], Ph. Schwemling[139], R. Schwienhorst[110], F. G. Sciacca[20], A. Sciandra[30], G. Sciolla[27], F. Scuri[75a], C. D. Sebastiani[37], K. Sedlaczek[119], S. C. Seidel[116], A. Seiden[140], B. D. Seidlitz[43], C. Seitz[49], J. M. Seixas[84b], G. Sekhniaidze[73a], L. Selem[61], N. Semprini-Cesari[24a,24b], A. Semushin[38,180], D. Sengupta[57], V. Senthilkumar[170], L. Serin[67], M. Sessa[77a,77b], H. Severini[124], F. Sforza[58a,58b], A. Sfyrla[57], Q. Sha[14], E. Shabalina[56], H. Shaddix[119], A. H. Shah[33], R. Shaheen[151], J. D. Shahinian[132], D. Shaked Renous[176], M. Shamim[37], L. Y. Shan[14], M. Shapiro[18a], A. Sharma[37], A. S. Sharma[171], P. Sharma[30], P. B. Shatalov[38], K. Shaw[153], S. M. Shaw[104], Q. Shen[145a], D. J. Sheppard[149], P. Sherwood[99], L. Shi[99], X. Shi[14], S. Shimizu[85], C. O. Shimmin[179], I. P. J. Shipsey[130,*], S. Shirabe[91], M. Shiyakova[40,z], M. J. Shochet[41], D. R. Shope[129], B. Shrestha[124], S. Shrestha[123,ak], I. Shreyber[38], M. J. Shroff[172], P. Sicho[135], A. M. Sickles[169], E. Sideras Haddad[34g,167], A. C. Sidley[118], A. Sidoti[24b], F. Siegert[51], Dj. Sijacki[16], F. Sili[93], J. M. Silva[53], I. Silva Ferreira[84b], M. V. Silva Oliveira[30], S. B. Silverstein[48a], S. Simion[67], R. Simoniello[37], E. L. Simpson[104], H. Simpson[153], L. R. Simpson[109], S. Simsek[83], S. Sindhu[56], P. Sinervo[162], S. N. Singh[27], S. Singh[30], S. Sinha[49], S. Sinha[104], M. Sioli[24a,24b], K. Sioulas[9], I. Siral[37], E. Sitnikova[49], J. Sjölin[48a,48b], A. Skaf[56], E. Skorda[21], P. Skubic[124], M. Slawinska[88], I. Slazyk[17], V. Smakhtin[176], B. H. Smart[138], S. Yu. Smirnov[141b], Y. Smirnov[38], L. N. Smirnova[38,a], O. Smirnova[101], A. C. Smith[43], D. R. Smith[166], E. A. Smith[41], J. L. Smith[104], M. B. Smith[35], R. Smith[150], H. Smitmanns[103], M. Smizanska[94], K. Smolek[136],

A. A. Snesarev[40], H. L. Snoek[118], S. Snyder[30], R. Sobie[172,ab], A. Soffer[158], C. A. Solans Sanchez[37], E. Yu. Soldatov[40], U. Soldevila[170], A. A. Solodkov[34g], S. Solomon[27], A. Soloshenko[40], K. Solovieva[55], O. V. Solovyanov[42], P. Sommer[51], A. Sonay[13], W. Y. Song[163b], A. Sopczak[136], A. L. Sopio[53], F. Sopkova[29b], J. D. Sorenson[116], I. R. Sotarriva Alvarez[142], V. Sothilingam[64a], O. J. Soto Sandoval[141b,141c], S. Sottocornola[69], R. Soualah[89b], Z. Soumaimi[36e], D. South[49], N. Soybelman[176], S. Spagnolo[71a,71b], M. Spalla[113], D. Sperlich[55], B. Spisso[73a,73b], D. P. Spiteri[60], M. Spousta[137], E. J. Staats[35], R. Stamen[64a], E. Stanecka[88], W. Stanek-Maslouska[49], M. V. Stange[51], B. Stanislaus[18a], M. M. Stanitzki[49], B. Stapf[49], E. A. Starchenko[38], G. H. Stark[140], J. Stark[92], P. Staroba[135], P. Starovoitov[89b], R. Staszewski[88], G. Stavropoulos[47], A. Stefl[37], P. Steinberg[30], B. Stelzer[149,163a], H. J. Stelzer[133], O. Stelzer-Chilton[163a], H. Stenzel[59], T. J. Stevenson[153], G. A. Stewart[37], J. R. Stewart[125], M. C. Stockton[37], G. Stoicea[28b], M. Stolarski[134a], S. Stonjek[113], A. Straessner[51], J. Strandberg[151], S. Strandberg[48a,48b], M. Stratmann[178], M. Strauss[124], T. Strebler[105], P. Strizenec[29b], R. Ströhmer[173], D. M. Strom[127], R. Stroynowski[46], A. Strubig[48a,48b], S. A. Stucci[30], B. Stugu[17], J. Stupak[124], N. A. Styles[49], D. Su[150], S. Su[63], W. Su[145b], X. Su[63], D. Suchy[29a], K. Sugizaki[132], V. V. Sulin[38], M. J. Sullivan[95], D. M. S. Sultan[130], L. Sultanaliyeva[38], S. Sultansoy[3b], S. Sun[177], W. Sun[14], O. Sunneborn Gudnadottir[168], N. Sur[105], M. R. Sutton[153], H. Suzuki[164], M. Svatos[135], P. N. Swallow[33], M. Swiatlowski[163a], T. Swirski[173], I. Sykora[29a], M. Sykora[137], T. Sykora[137], D. Ta[103], K. Tackmann[49,y], A. Taffard[166], R. Tafirout[163a], J. S. Tafoya Vargas[67], Y. Takubo[85], M. Talby[105], A. A. Talyshev[38], K. C. Tam[65b], N. M. Tamir[158], A. Tanaka[160], J. Tanaka[160], R. Tanaka[67], M. Tanasini[152], Z. Tao[171], S. Tapia Araya[141f], S. Tapprogge[103], A. Tarek Abouelfadl Mohamed[110], S. Tarem[157], K. Tariq[14], G. Tarna[28b], G. F. Tartarelli[72a], M. J. Tartarin[92], P. Tas[137], M. Tasevsky[135], E. Tassi[45a,45b], A. C. Tate[169], G. Tateno[160], Y. Tayalati[36e,aa], G. N. Taylor[108], W. Taylor[163b], A. S. Tegetmeier[92], P. Teixeira-Dias[98], J. J. Teoh[162], K. Terashi[160], J. Terron[102], S. Terzo[13], M. Testa[54], R. J. Teuscher[162,ab], A. Thaler[80], O. Theiner[57], T. Theveneaux-Pelzer[105], O. Thielmann[178], D. W. Thomas[98], J. P. Thomas[21], E. A. Thompson[18a], P. D. Thompson[21], E. Thomson[132], R. E. Thornberry[46], C. Tian[63], Y. Tian[57], V. Tikhomirov[38,a], Yu. A. Tikhonov[38], S. Timoshenko[38], D. Timoshyn[137], E. X. L. Ting[1], P. Tipton[179], A. Tishelman-Charny[30], S. H. Tlou[34g], K. Todome[142], S. Todorova-Nova[137], S. Todt[51], L. Toffolin[70a,70c], M. Togawa[85], J. Tojo[91], S. Tokár[29a], O. Toldaiev[69], G. Tolkachev[105], M. Tomoto[85,114], L. Tompkins[150,o], E. Torrence[127], H. Torres[92], E. Torró Pastor[170], M. Toscani[31], C. Tosciri[41], M. Tost[11], D. R. Tovey[146], T. Trefzger[173], A. Tricoli[30], I. M. Trigger[163a], S. Trincaz-Duvoid[131], D. A. Trischuk[27], A. Tropina[40], L. Truong[34c], M. Trzebinski[88], A. Trzupek[88], F. Tsai[152], M. Tsai[109], A. Tsiamis[159], P. V. Tsiareshka[40], S. Tsigaridas[163a], A. Tsirigotis[159,u], V. Tsiskaridze[162], E. G. Tskhadadze[156a], M. Tsopoulou[159], Y. Tsujikawa[90], I. I. Tsukerman[38], V. Tsulaia[18a], S. Tsuno[85], K. Tsuri[122], D. Tsybychev[152], Y. Tu[65b], A. Tudorache[28b], V. Tudorache[28b], S. Turchikhin[58a,58b], I. Turk Cakir[3a], R. Turra[72a], T. Turtuvshin[40], P. M. Tuts[43], S. Tzamarias[159,e], E. Tzovara[103], F. Ukegawa[164], P. A. Ulloa Poblete[141b,141c], E. N. Umaka[30], G. Unal[37], A. Undrus[30], G. Unel[166], J. Urban[29b], P. Urrejola[141a], G. Usai[8], R. Ushioda[161], M. Usman[111], F. Ustuner[53], Z. Uysal[83], V. Vacek[136], B. Vachon[107], T. Vafeiadis[37], A. Vaitkus[99], C. Valderanis[112], E. Valdes Santurio[48a,48b], M. Valente[163a], S. Valentinetti[24a,24b], A. Valero[170], E. Valiente Moreno[170], A. Vallier[92], J. A. Valls Ferrer[170], D. R. Van Arneman[118], T. R. Van Daalen[143], A. Van Der Graaf[50], H. Z. Van Der Schyf[34g], P. Van Gemmeren[6], M. Van Rijnbach[37], S. Van Stroud[99], I. Van Vulpen[118], P. Vana[137], M. Vanadia[77a,77b], U. M. Vande Voorde[151], W. Vandelli[37], E. R. Vandewall[125], D. Vannicola[158], L. Vannoli[54], R. Vari[76a], E. W. Varnes[7], C. Varni[18b], D. Varouchas[67], L. Varriale[170], K. E. Varvell[154], M. E. Vasile[28b], L. Vaslin[85], A. Vasyukov[40], L. M. Vaughan[125], R. Vavricka[137], T. Vazquez Schroeder[13], J. Veatch[32], V. Vecchio[104], M. J. Veen[106], I. Veliscek[30], L. M. Veloce[162], F. Veloso[134a,134c], S. Veneziano[76a], A. Ventura[71a,71b], S. Ventura Gonzalez[139], A. Verbytskyi[113], M. Verducci[75a,75b], C. Vergis[97], M. Verissimo De Araujo[84b], W. Verkerke[118], J. C. Vermeulen[118], C. Vernieri[150], M. Vessella[166], M. C. Vetterli[149,ag], A. Vgenopoulos[103], N. Viaux Maira[141f], T. Vickey[146], O. E. Vickey Boeriu[146], G. H. A. Viehhauser[130], L. Vigani[64b], M. Vigl[113], M. Villa[24a,24b], M. Villaplana Perez[170], E. M. Villhauer[53], E. Vilucchi[54], M. G. Vincter[35], A. Visibile[118], C. Vittori[37], I. Vivarelli[24a,24b], E. Voevodina[113], F. Vogel[112], J. C. Voigt[51], P. Vokac[136], Yu. Volkotrub[87b], E. Von Toerne[25], B. Vormwald[37], K. Vorobev[38], M. Vos[170], K. Voss[148], M. Vozak[37], L. Vozdecky[124], N. Vranjes[16], M. Vranjes Milosavljevic[16], M. Vreeswijk[118], N. K. Vu[145a,145b], R. Vuillermet[37], O. Vujinovic[103], I. Vukotic[41], I. K. Vyas[35], S. Wada[164], C. Wagner[150], J. M. Wagner[18a], W. Wagner[178], S. Wahdan[178], H. Wahlberg[93], C. H. Waits[124], J. Walder[138], R. Walker[112], W. Walkowiak[148], A. Wall[132], E. J. Wallin[101], T. Wamorkar[18a], A. Z. Wang[140], C. Wang[103], C. Wang[11],

H. Wang[18a], J. Wang[65c], P. Wang[104], P. Wang[99], R. Wang[62], R. Wang[6], S. M. Wang[155], S. Wang[14], T. Wang[63], T. Wang[63], W. T. Wang[81], W. Wang[14], X. Wang[169], X. Wang[145a], X. Wang[49], Y. Wang[115a], Y. Wang[63], Z. Wang[109], Z. Wang[52,145a,145b], Z. Wang[109], C. Wanotayaroj[85], A. Warburton[107], R. J. Ward[21], A. L. Warnerbring[148], N. Warrack[60], S. Waterhouse[98], A. T. Watson[21], H. Watson[53], M. F. Watson[21], E. Watton[60], G. Watts[143], B. M. Waugh[99], J. M. Webb[55], C. Weber[30], H. A. Weber[19], M. S. Weber[20], S. M. Weber[64a], C. Wei[63], Y. Wei[55], A. R. Weidberg[130], E. J. Weik[121], J. Weingarten[50], C. Weiser[55], C. J. Wells[49], T. Wenaus[30], B. Wendland[50], T. Wengler[37], N. S. Wenke[113], N. Wermes[25], M. Wessels[64a], A. M. Wharton[94], A. S. White[62], A. White[8], M. J. White[1], D. Whiteson[166], L. Wickremasinghe[128], W. Wiedenmann[177], M. Wielers[138], C. Wiglesworth[44], D. J. Wilbern[124], H. G. Wilkens[37], J. J. H. Wilkinson[33], D. M. Williams[43], H. H. Williams[132], S. Williams[33], S. Willocq[106], B. J. Wilson[104], D. J. Wilson[104], P. J. Windischhofer[41], F. I. Winkel[31], F. Winklmeier[127], B. T. Winter[55], M. Wittgen[150], M. Wobisch[100], T. Wojtkowski[61], Z. Wolffs[118], J. Wollrath[37], M. W. Wolter[88], H. Wolters[134a,134c], M. C. Wong[140], E. L. Woodward[43], S. D. Worm[49], B. K. Wosiek[88], K. W. Woźniak[88], S. Wozniewski[56], K. Wraight[60], C. Wu[21], M. Wu[115b], M. Wu[117], S. L. Wu[177], X. Wu[57], X. Wu[63], Y. Wu[63], Z. Wu[4], J. Wuerzinger[113,ae], T. R. Wyatt[104], B. M. Wynne[53], S. Xella[44], L. Xia[115a], M. Xia[15], M. Xie[63], A. Xiong[127], J. Xiong[18a], D. Xu[14], H. Xu[63], L. Xu[63], R. Xu[132], T. Xu[109], Y. Xu[143], Z. Xu[53], Z. Xu[115a], B. Yabsley[154], S. Yacoob[34a], Y. Yamaguchi[85], E. Yamashita[160], H. Yamauchi[164], T. Yamazaki[18a], Y. Yamazaki[86], S. Yan[60], Z. Yan[106], H. J. Yang[145a,145b], H. T. Yang[63], S. Yang[63], T. Yang[65c], X. Yang[37], X. Yang[14], Y. Yang[46], Y. Yang[63], W.-M. Yao[18a], C. L. Yardley[153], H. Ye[56], J. Ye[14], S. Ye[30], X. Ye[63], Y. Yeh[99], I. Yeletskikh[40], B. Yeo[18b], M. R. Yexley[99], T. P. Yildirim[130], P. Yin[43], K. Yorita[175], S. Younas[28b], C. J. S. Young[37], C. Young[150], N. D. Young[127], Y. Yu[63], J. Yuan[14,115c], M. Yuan[109], R. Yuan[145a,145b], L. Yue[99], M. Zaazoua[63], B. Zabinski[88], I. Zahir[36a], Z. K. Zak[88], T. Zakareishvili[170], S. Zambito[57], J. A. Zamora Saa[141b,141d], J. Zang[160], D. Zanzi[55], R. Zanzottera[72a,72b], O. Zaplatilek[136], C. Zeitnitz[178], H. Zeng[14], J. C. Zeng[169], D. T. Zenger Jr[27], O. Zenin[38], T. Ženiš[29a], S. Zenz[97], S. Zerradi[36a], D. Zerwas[67], M. Zhai[14,115c], D. F. Zhang[146], J. Zhang[144a], J. Zhang[6], K. Zhang[14,115c], L. Zhang[63], L. Zhang[115a], P. Zhang[14,115c], R. Zhang[177], S. Zhang[92], T. Zhang[160], X. Zhang[145a], Y. Zhang[143], Y. Zhang[99], Y. Zhang[63], Y. Zhang[115a], Z. Zhang[18a], Z. Zhang[144a], Z. Zhang[67], H. Zhao[143], T. Zhao[144a], Y. Zhao[35], Z. Zhao[63], Z. Zhao[63], A. Zhemchugov[40], J. Zheng[115a], K. Zheng[169], X. Zheng[63], Z. Zheng[150], D. Zhong[169], B. Zhou[109], H. Zhou[7], N. Zhou[145a], Y. Zhou[15], Y. Zhou[115a], Y. Zhou[7], C. G. Zhu[144a], J. Zhu[109], X. Zhu[145b], Y. Zhu[145a], Y. Zhu[63], X. Zhuang[14], K. Zhukov[69], N. I. Zimine[40], J. Zinsser[64b], M. Ziolkowski[148], L. Živković[16], A. Zoccoli[24a,24b], K. Zoch[62], T. G. Zorbas[146], O. Zormpa[47], W. Zou[43], L. Zwalinski[37]

[1] Department of Physics, University of Adelaide, Adelaide, Australia
[2] Department of Physics, University of Alberta, Edmonton, AB, Canada
[3] [(a)]Department of Physics, Ankara University, Ankara, Turkey; [(b)]Division of Physics, TOBB University of Economics and Technology, Ankara, Turkey
[4] LAPP, Université Savoie Mont Blanc, CNRS/IN2P3, Annecy, France
[5] APC, Université Paris Cité, CNRS/IN2P3, Paris, France
[6] High Energy Physics Division, Argonne National Laboratory, Argonne, IL, USA
[7] Department of Physics, University of Arizona, Tucson, AZ, USA
[8] Department of Physics, University of Texas at Arlington, Arlington, TX, USA
[9] Physics Department, National and Kapodistrian University of Athens, Athens, Greece
[10] Physics Department, National Technical University of Athens, Zografou, Greece
[11] Department of Physics, University of Texas at Austin, Austin, TX, USA
[12] Institute of Physics, Azerbaijan Academy of Sciences, Baku, Azerbaijan
[13] Institut de Física d'Altes Energies (IFAE), Barcelona Institute of Science and Technology, Barcelona, Spain
[14] Institute of High Energy Physics, Chinese Academy of Sciences, Beijing, China
[15] Physics Department, Tsinghua University, Beijing, China
[16] Institute of Physics, University of Belgrade, Belgrade, Serbia
[17] Department for Physics and Technology, University of Bergen, Bergen, Norway
[18] [(a)]Physics Division, Lawrence Berkeley National Laboratory, Berkeley, CA, USA; [(b)]University of California, Berkeley, CA, USA
[19] Institut für Physik, Humboldt Universität zu Berlin, Berlin, Germany

[20] Albert Einstein Center for Fundamental Physics and Laboratory for High Energy Physics, University of Bern, Bern, Switzerland
[21] School of Physics and Astronomy, University of Birmingham, Birmingham, UK
[22] [(a)]Department of Physics, Bogazici University, Istanbul, Turkey; [(b)]Department of Physics Engineering, Gaziantep University, Gaziantep, Turkey; [(c)]Department of Physics, Istanbul University, Istanbul, Turkey
[23] [(a)]Facultad de Ciencias y Centro de Investigaciónes, Universidad Antonio Nariño, Bogotá, Colombia; [(b)]Departamento de Física, Universidad Nacional de Colombia, Bogotá, Colombia
[24] [(a)]Dipartimento di Fisica e Astronomia A. Righi, Università di Bologna, Bologna, Italy; [(b)]INFN Sezione di Bologna, Bologna, Italy
[25] Physikalisches Institut, Universität Bonn, Bonn, Germany
[26] Department of Physics, Boston University, Boston, MA, USA
[27] Department of Physics, Brandeis University, Waltham, MA, USA
[28] [(a)]Transilvania University of Brasov, Brasov, Romania; [(b)]Horia Hulubei National Institute of Physics and Nuclear Engineering, Bucharest, Romania; [(c)]Department of Physics, Alexandru Ioan Cuza University of Iasi, Iasi, Romania; [(d)]Physics Department, National Institute for Research and Development of Isotopic and Molecular Technologies, Cluj-Napoca, Romania; [(e)]National University of Science and Technology Politechnica, Bucharest, Romania; [(f)]West University in Timisoara, Timisoara, Romania; [(g)]Faculty of Physics, University of Bucharest, Bucharest, Romania
[29] [(a)]Faculty of Mathematics, Physics and Informatics, Comenius University, Bratislava, Slovak Republic; [(b)]Department of Subnuclear Physics, Institute of Experimental Physics of the Slovak Academy of Sciences, Kosice, Slovak Republic
[30] Physics Department, Brookhaven National Laboratory, Upton, NY, USA
[31] Universidad de Buenos Aires, Facultad de Ciencias Exactas y Naturales, Departamento de Física, y CONICET, Instituto de Física de Buenos Aires (IFIBA), Buenos Aires, Argentina
[32] California State University, Long Beach, CA, USA
[33] Cavendish Laboratory, University of Cambridge, Cambridge, UK
[34] [(a)]Department of Physics, University of Cape Town, Cape Town, South Africa; [(b)]iThemba Labs, Western Cape, South Africa; [(c)]Department of Mechanical Engineering Science, University of Johannesburg, Johannesburg, South Africa; [(d)]National Institute of Physics, University of the Philippines Diliman (Philippines), Quezon City, Philippines; [(e)]Department of Physics, University of South Africa, Pretoria, South Africa; [(f)]University of Zululand, KwaDlangezwa, Empangeni, South Africa; [(g)]School of Physics, University of the Witwatersrand, Johannesburg, South Africa
[35] Department of Physics, Carleton University, Ottawa, ON, Canada
[36] [(a)]Faculté des Sciences Ain Chock, Université Hassan II de Casablanca, Casablanca, Morocco; [(b)]Faculté des Sciences, Université Ibn-Tofail, Kenitra, Morocco; [(c)]Faculté des Sciences Semlalia, Université Cadi Ayyad, LPHEA-Marrakech, Marrakech, Morocco; [(d)]LPMR, Faculté des Sciences, Université Mohamed Premier, Oujda, Morocco; [(e)]Faculté des sciences, Université Mohammed V, Rabat, Morocco; [(f)]Institute of Applied Physics, Mohammed VI Polytechnic University, Ben Guerir, Morocco
[37] CERN, Geneva, Switzerland
[38] Affiliated with an Institute Covered by a Cooperation Agreement with CERN, Geneva, Switzerland
[39] Affiliated with an Institute Formerly Covered by a Cooperation Agreement with CERN, Geneva, Switzerland
[40] Affiliated with an International Laboratory Covered by a Cooperation Agreement with CERN, Geneva, Switzerland
[41] Enrico Fermi Institute, University of Chicago, Chicago, IL, USA
[42] LPC, Université Clermont Auvergne, CNRS/IN2P3, Clermont-Ferrand, France
[43] Nevis Laboratory, Columbia University, Irvington, NY, USA
[44] Niels Bohr Institute, University of Copenhagen, Copenhagen, Denmark
[45] [(a)]Dipartimento di Fisica, Università della Calabria, Rende, Italy; [(b)]INFN Gruppo Collegato di Cosenza, Laboratori Nazionali di Frascati, Frascati, Italy
[46] Physics Department, Southern Methodist University, Dallas, TX, USA
[47] National Centre for Scientific Research "Demokritos", Agia Paraskevi, Greece
[48] [(a)]Department of Physics, Stockholm University, Stockholm, Sweden; [(b)]Oskar Klein Centre, Stockholm, Sweden
[49] Deutsches Elektronen-Synchrotron DESY, Hamburg and Zeuthen, Germany
[50] Fakultät Physik , Technische Universität Dortmund, Dortmund, Germany
[51] Institut für Kern- und Teilchenphysik, Technische Universität Dresden, Dresden, Germany

[52] Department of Physics, Duke University, Durham, NC, USA
[53] SUPA-School of Physics and Astronomy, University of Edinburgh, Edinburgh, UK
[54] INFN e Laboratori Nazionali di Frascati, Frascati, Italy
[55] Physikalisches Institut, Albert-Ludwigs-Universität Freiburg, Freiburg, Germany
[56] II. Physikalisches Institut, Georg-August-Universität Göttingen, Göttingen, Germany
[57] Département de Physique Nucléaire et Corpusculaire, Université de Genève, Geneva, Switzerland
[58] [(a)]Dipartimento di Fisica, Università di Genova, Genoa, Italy; [(b)]INFN Sezione di Genova, Genoa, Italy
[59] II. Physikalisches Institut, Justus-Liebig-Universität Giessen, Giessen, Germany
[60] SUPA-School of Physics and Astronomy, University of Glasgow, Glasgow, UK
[61] LPSC, Université Grenoble Alpes, CNRS/IN2P3, Grenoble INP, Grenoble, France
[62] Laboratory for Particle Physics and Cosmology, Harvard University, Cambridge, MA, USA
[63] Department of Modern Physics and State Key Laboratory of Particle Detection and Electronics, University of Science and Technology of China, Hefei, China
[64] [(a)]Kirchhoff-Institut für Physik, Ruprecht-Karls-Universität Heidelberg, Heidelberg, Germany; [(b)]Physikalisches Institut, Ruprecht-Karls-Universität Heidelberg, Heidelberg, Germany
[65] [(a)]Department of Physics, Chinese University of Hong Kong, Shatin, N.T., Hong Kong, China; [(b)]Department of Physics, University of Hong Kong, Hong Kong, China; [(c)]Department of Physics and Institute for Advanced Study, Hong Kong University of Science and Technology, Clear Water Bay, Kowloon, Hong Kong, China
[66] Department of Physics, National Tsing Hua University, Hsinchu, Taiwan
[67] IJCLab, Université Paris-Saclay, CNRS/IN2P3, 91405 Orsay, France
[68] Centro Nacional de Microelectrónica (IMB-CNM-CSIC), Barcelona, Spain
[69] Department of Physics, Indiana University, Bloomington, IN, USA
[70] [(a)]INFN Gruppo Collegato di Udine, Sezione di Trieste, Udine, Italy; [(b)]ICTP, Trieste, Italy; [(c)]Dipartimento Politecnico di Ingegneria e Architettura, Università di Udine, Udine, Italy
[71] [(a)]INFN Sezione di Lecce, Lecce, Italy; [(b)]Dipartimento di Matematica e Fisica, Università del Salento, Lecce, Italy
[72] [(a)]INFN Sezione di Milano, Milan, Italy; [(b)]Dipartimento di Fisica, Università di Milano, Milan, Italy
[73] [(a)]INFN Sezione di Napoli, Naples, Italy; [(b)]Dipartimento di Fisica, Università di Napoli, Naples, Italy
[74] [(a)]INFN Sezione di Pavia, Pavia, Italy; [(b)]Dipartimento di Fisica, Università di Pavia, Pavia, Italy
[75] [(a)]INFN Sezione di Pisa, Pisa, Italy; [(b)]Dipartimento di Fisica E. Fermi, Università di Pisa, Pisa, Italy
[76] [(a)]INFN Sezione di Roma, Rome, Italy; [(b)]Dipartimento di Fisica, Sapienza Università di Roma, Rome, Italy
[77] [(a)]INFN Sezione di Roma Tor Vergata, Rome, Italy; [(b)]Dipartimento di Fisica, Università di Roma Tor Vergata, Rome, Italy
[78] [(a)]INFN Sezione di Roma Tre, Rome, Italy; [(b)]Dipartimento di Matematica e Fisica, Università Roma Tre, Rome, Italy
[79] [(a)]INFN-TIFPA, Trento, Italy; [(b)]Università degli Studi di Trento, Trento, Italy
[80] Department of Astro and Particle Physics, Universität Innsbruck, Innsbruck, Austria
[81] University of Iowa, Iowa City, IA, USA
[82] Department of Physics and Astronomy, Iowa State University, Ames, IA, USA
[83] Istinye University, Sariyer, Istanbul, Turkey
[84] [(a)]Departamento de Engenharia Elétrica, Universidade Federal de Juiz de Fora (UFJF), Juiz de Fora, Brazil; [(b)]Universidade Federal do Rio De Janeiro COPPE/EE/IF, Rio de Janeiro, Brazil; [(c)]Instituto de Física, Universidade de São Paulo, São Paulo, Brazil; [(d)]Rio de Janeiro State University, Rio de Janeiro, Brazil; [(e)]Federal University of Bahia, Bahia, Brazil
[85] KEK, High Energy Accelerator Research Organization, Tsukuba, Japan
[86] Graduate School of Science, Kobe University, Kobe, Japan
[87] [(a)]Faculty of Physics and Applied Computer Science, AGH University of Krakow, Kraków, Poland; [(b)]Marian Smoluchowski Institute of Physics, Jagiellonian University, Kraków, Poland
[88] Institute of Nuclear Physics Polish Academy of Sciences, Kraków, Poland
[89] [(a)]Khalifa University of Science and Technology, Abu Dhabi, United Arab Emirates; [(b)]University of Sharjah, Sharjah, United Arab Emirates
[90] Faculty of Science, Kyoto University, Kyoto, Japan
[91] Research Center for Advanced Particle Physics and Department of Physics, Kyushu University, Fukuoka, Japan
[92] L2IT, Université de Toulouse, CNRS/IN2P3, UPS, Toulouse, France
[93] Instituto de Física La Plata, Universidad Nacional de La Plata and CONICET, La Plata, Argentina

[94] Physics Department, Lancaster University, Lancaster, UK
[95] Oliver Lodge Laboratory, University of Liverpool, Liverpool, UK
[96] Department of Experimental Particle Physics, Jožef Stefan Institute and Department of Physics, University of Ljubljana, Ljubljana, Slovenia
[97] School of Physics and Astronomy, Queen Mary University of London, London, UK
[98] Department of Physics, Royal Holloway University of London, Egham, UK
[99] Department of Physics and Astronomy, University College London, London, UK
[100] Louisiana Tech University, Ruston, LA, USA
[101] Fysiska institutionen, Lunds universitet, Lund, Sweden
[102] Departamento de Física Teorica C-15 and CIAFF, Universidad Autónoma de Madrid, Madrid, Spain
[103] Institut für Physik, Universität Mainz, Mainz, Germany
[104] School of Physics and Astronomy, University of Manchester, Manchester, UK
[105] CPPM, Aix-Marseille Université, CNRS/IN2P3, Marseille, France
[106] Department of Physics, University of Massachusetts, Amherst, MA, USA
[107] Department of Physics, McGill University, Montreal, QC, Canada
[108] School of Physics, University of Melbourne, Melbourne, VIC, Australia
[109] Department of Physics, University of Michigan, Ann Arbor, MI, USA
[110] Department of Physics and Astronomy, Michigan State University, East Lansing, MI, USA
[111] Group of Particle Physics, University of Montreal, Montreal, QC, Canada
[112] Fakultät für Physik, Ludwig-Maximilians-Universität München, Munich, Germany
[113] Max-Planck-Institut für Physik (Werner-Heisenberg-Institut), Munich, Germany
[114] Graduate School of Science and Kobayashi-Maskawa Institute, Nagoya University, Nagoya, Japan
[115] [(a)]Department of Physics, Nanjing University, Nanjing, China; [(b)]School of Science, Shenzhen Campus of Sun Yat-sen University, Shenzhen, China; [(c)]University of Chinese Academy of Science (UCAS), Beijing, China
[116] Department of Physics and Astronomy, University of New Mexico, Albuquerque, NM, USA
[117] Institute for Mathematics, Astrophysics and Particle Physics, Radboud University/Nikhef, Nijmegen, The Netherlands
[118] Nikhef National Institute for Subatomic Physics and University of Amsterdam, Amsterdam, The Netherlands
[119] Department of Physics, Northern Illinois University, De Kalb, IL, USA
[120] [(a)]New York University Abu Dhabi, Abu Dhabi, United Arab Emirates; [(b)]United Arab Emirates University, Al Ain, United Arab Emirates
[121] Department of Physics, New York University, New York, NY, USA
[122] Ochanomizu University, Otsuka, Bunkyo-ku, Tokyo, Japan
[123] Ohio State University, Columbus, OH, USA
[124] Homer L. Dodge Department of Physics and Astronomy, University of Oklahoma, Norman, OK, USA
[125] Department of Physics, Oklahoma State University, Stillwater, OK, USA
[126] Joint Laboratory of Optics, Palacký University, Olomouc, Czech Republic
[127] Institute for Fundamental Science, University of Oregon, Eugene, OR, USA
[128] Graduate School of Science, Osaka University, Osaka, Japan
[129] Department of Physics, University of Oslo, Oslo, Norway
[130] Department of Physics, Oxford University, Oxford, UK
[131] LPNHE, Sorbonne Université, Université Paris Cité, CNRS/IN2P3, Paris, France
[132] Department of Physics, University of Pennsylvania, Philadelphia, PA, USA
[133] Department of Physics and Astronomy, University of Pittsburgh, Pittsburgh, PA, USA
[134] [(a)]Laboratório de Instrumentação e Física Experimental de Partículas-LIP, Lisbon, Portugal; [(b)]Departamento de Física, Faculdade de Ciências, Universidade de Lisboa, Lisbon, Portugal; [(c)]Departamento de Física, Universidade de Coimbra, Coimbra, Portugal; [(d)]Centro de Física Nuclear da Universidade de Lisboa, Lisbon, Portugal; [(e)]Departamento de Física, Universidade do Minho, Braga, Portugal; [(f)]Departamento de Física Teórica y del Cosmos, Universidad de Granada, Granada, Spain; [(g)]Departamento de Física, Instituto Superior Técnico, Universidade de Lisboa, Lisbon, Portugal
[135] Institute of Physics of the Czech Academy of Sciences, Prague, Czech Republic
[136] Czech Technical University in Prague, Prague, Czech Republic
[137] Faculty of Mathematics and Physics, Charles University, Prague, Czech Republic
[138] Particle Physics Department, Rutherford Appleton Laboratory, Didcot, UK
[139] IRFU, CEA, Université Paris-Saclay, Gif-sur-Yvette, France

[140] Santa Cruz Institute for Particle Physics, University of California Santa Cruz, Santa Cruz, CA, USA
[141] [(a)]Departamento de Física, Pontificia Universidad Católica de Chile, Santiago, Chile; [(b)]Millennium Institute for Subatomic Physics at High Energy Frontier (SAPHIR), Santiago, Chile; [(c)]Instituto de Investigación Multidisciplinario en Ciencia y Tecnología, y Departamento de Física, Universidad de La Serena, La Serena, Chile; [(d)]Department of Physics, Universidad Andres Bello, Santiago, Chile; [(e)]Instituto de Alta Investigación, Universidad de Tarapacá, Arica, Chile; [(f)]Departamento de Física, Universidad Técnica Federico Santa María, Valparaíso, Chile
[142] Department of Physics, Institute of Science, Tokyo, Japan
[143] Department of Physics, University of Washington, Seattle, WA, USA
[144] [(a)]Institute of Frontier and Interdisciplinary Science and Key Laboratory of Particle Physics and Particle Irradiation (MOE), Shandong University, Qingdao, China; [(b)]School of Physics, Zhengzhou University, Zhengzhou, China
[145] [(a)]School of Physics and Astronomy, Key Laboratory for Particle Astrophysics and Cosmology (MOE), SKLPPC, Shanghai Jiao Tong University, Shanghai, China; [(b)]Tsung-Dao Lee Institute, Shanghai, China
[146] Department of Physics and Astronomy, University of Sheffield, Sheffield, UK
[147] Department of Physics, Shinshu University, Nagano, Japan
[148] Department Physik, Universität Siegen, Siegen, Germany
[149] Department of Physics, Simon Fraser University, Burnaby, BC, Canada
[150] SLAC National Accelerator Laboratory, Stanford, CA, USA
[151] Department of Physics, Royal Institute of Technology, Stockholm, Sweden
[152] Departments of Physics and Astronomy, Stony Brook University, Stony Brook, NY, USA
[153] Department of Physics and Astronomy, University of Sussex, Brighton, UK
[154] School of Physics, University of Sydney, Sydney, Australia
[155] Institute of Physics, Academia Sinica, Taipei, Taiwan
[156] [(a)]E. Andronikashvili Institute of Physics, Iv. Javakhishvili Tbilisi State University, Tbilisi, Georgia; [(b)]High Energy Physics Institute, Tbilisi State University, Tbilisi, Georgia; [(c)]University of Georgia, Tbilisi, Georgia
[157] Department of Physics, Technion, Israel Institute of Technology, Haifa, Israel
[158] Raymond and Beverly Sackler School of Physics and Astronomy, Tel Aviv University, Tel Aviv, Israel
[159] Department of Physics, Aristotle University of Thessaloniki, Thessaloníki, Greece
[160] International Center for Elementary Particle Physics and Department of Physics, University of Tokyo, Tokyo, Japan
[161] Graduate School of Science and Technology, Tokyo Metropolitan University, Tokyo, Japan
[162] Department of Physics, University of Toronto, Toronto, ON, Canada
[163] [(a)]TRIUMF, Vancouver, BC, Canada; [(b)]Department of Physics and Astronomy, York University, Toronto, ON, Canada
[164] Division of Physics and Tomonaga Center for the History of the Universe, Faculty of Pure and Applied Sciences, University of Tsukuba, Tsukuba, Japan
[165] Department of Physics and Astronomy, Tufts University, Medford, MA, USA
[166] Department of Physics and Astronomy, University of California Irvine, Irvine, CA, USA
[167] University of West Attica, Athens, Greece
[168] Department of Physics and Astronomy, University of Uppsala, Uppsala, Sweden
[169] Department of Physics, University of Illinois, Urbana, IL, USA
[170] Instituto de Física Corpuscular (IFIC), Centro Mixto Universidad de Valencia-CSIC, Valencia, Spain
[171] Department of Physics, University of British Columbia, Vancouver, BC, Canada
[172] Department of Physics and Astronomy, University of Victoria, Victoria, BC, Canada
[173] Fakultät für Physik und Astronomie, Julius-Maximilians-Universität Würzburg, Würzburg, Germany
[174] Department of Physics, University of Warwick, Coventry, UK
[175] Waseda University, Tokyo, Japan
[176] Department of Particle Physics and Astrophysics, Weizmann Institute of Science, Rehovot, Israel
[177] Department of Physics, University of Wisconsin, Madison, WI, USA
[178] Fakultät für Mathematik und Naturwissenschaften, Fachgruppe Physik, Bergische Universität Wuppertal, Wuppertal, Germany
[179] Department of Physics, Yale University, New Haven, CT, USA
[180] Yerevan Physics Institute, Yerevan, Armenia

[a] Also Affiliated with an Institute Covered by a Cooperation Agreement with CERN, Geneva, Switzerland
[b] Also at An-Najah National University, Nablus, Palestine

[c] Also at Borough of Manhattan Community College, City University of New York, New York, NY, USA
[d] Also at Center for High Energy Physics, Peking University, Beijing, China
[e] Also at Center for Interdisciplinary Research and Innovation (CIRI-AUTH), Thessaloníki, Greece
[f] Also at CERN, Geneva, Switzerland
[g] Also at CMD-AC UNEC Research Center, Azerbaijan State University of Economics (UNEC), Baku, Azerbaijan
[h] Also at Département de Physique Nucléaire et Corpusculaire, Université de Genève, Geneva, Switzerland
[i] Also at Departament de Fisica de la Universitat Autonoma de Barcelona, Barcelona, Spain
[j] Also at Department of Financial and Management Engineering, University of the Aegean, Chios, Greece
[k] Also at Department of Mathematical Sciences, University of South Africa, Johannesburg, South Africa
[l] Also at Department of Physics, Bolu Abant Izzet Baysal University, Bolu, Turkey
[m] Also at Department of Physics, California State University, Sacramento, USA
[n] Also at Department of Physics, King's College London, London, UK
[o] Also at Department of Physics, Stanford University, Stanford, CA, USA
[p] Also at Department of Physics, Stellenbosch University, Stellenbosch, South Africa
[q] Also at Department of Physics, University of Fribourg, Fribourg, Switzerland
[r] Also at Department of Physics, University of Thessaly, Vólos, Greece
[s] Also at Department of Physics, Westmont College, Santa Barbara, USA
[t] Also at Faculty of Physics, Sofia University, 'St. Kliment Ohridski', Sofia, Bulgaria
[u] Also at Hellenic Open University, Patras, Greece
[v] Also at Henan University, Kaifeng, China
[w] Also at Imam Mohammad Ibn Saud Islamic University, Riyadh, Saudi Arabia
[x] Also at Institucio Catalana de Recerca i Estudis Avancats, ICREA, Barcelona, Spain
[y] Also at Institut für Experimentalphysik, Universität Hamburg, Hamburg, Germany
[z] Also at Institute for Nuclear Research and Nuclear Energy (INRNE) of the Bulgarian Academy of Sciences, Sofia, Bulgaria
[aa] Also at Institute of Applied Physics, Mohammed VI Polytechnic University, Ben Guerir, Morocco
[ab] Also at Institute of Particle Physics (IPP), Victoria, Canada
[ac] Also at Institute of Physics, Azerbaijan Academy of Sciences, Baku, Azerbaijan
[ad] Also at National Institute of Physics, University of the Philippines Diliman (Philippines), Quezon City, Philippines
[ae] Also at Technical University of Munich, Munich, Germany
[af] Also at The Collaborative Innovation Center of Quantum Matter (CICQM), Beijing, China
[ag] Also at TRIUMF, Vancouver, BC, Canada
[ah] Also at Università di Napoli Parthenope, Naples, Italy
[ai] Also at Department of Physics, University of Colorado Boulder, Colorado, USA
[aj] Also at University of the Western Cape, Cape Town, South Africa
[ak] Also at Washington College, Chestertown, MD, USA
[al] Also at Physics Department, Yeditepe University, Istanbul, Turkey
[*] Deceased